

Nano-confined multi-component metal hydride system for hydrogen sensing application

submitted in partial fulfillment of the requirements of

The degree of
Doctor of Philosophy
of the
Indian Institute of Technology Bombay, India
and
Monash University, Australia

by

Arif Ibrahim

Supervisors:

Sidhartha P Duttagupta (IIT Bombay)

Arindam Sarkar (IIT Bombay)

Sankara Sarma V Tatiparti (IIT Bombay)

Raman Singh (Monash University)

Gita Pendharkar (Monash University)

List all supervisors involved



*The course of study for this award was developed jointly by
Monash University, Australia and the Indian Institute of Technology Bombay, India
and was given academic recognition by each of them.*

*The programme was administrated by The IITB-Monash Research Academy
(Year 2020)*

This thesis is dedicated to my family

Declaration

I declare that this written submission represents my ideas in my own words and where others' opinions or concepts have been included; I have adequately cited and referenced the sources. I also declare that I have adhered to all principles of academic honesty and integrity and have not misrepresented or fabricated or falsified any idea/data/fact/sources in my submission. I understand that any violation of the above will be cause for disciplinary action by the institute and can also evoke a penal response from the sources which have thus not been appropriately cited or from whom proper permission has not been taken when needed.

(Signature)

Arif Ibrahim

(Name of the student)

Roll No. 154074001

Date 30/10/20

Abstract

Hydrogen has been portrayed as a new alternative energy source to replace non-renewable energy sources such as fossil fuel [1]. Hydrogen is going to be a prime part of the fuel cells, particularly for automobiles. Hydrogen energy is also useful for space applications, since combustion of hydrogen can provide very high energy densities as compared to other energy sources such as petroleum and diesel. Safety is a crucial aspect while handling hydrogen [2, 3]. Hydrogen gas is colorless, odorless, highly flammable at a concentration above 4%, and highly explosive at the level above 15% [4-7]. Therefore, the rapid detection of hydrogen gas is essential for public safety and welfare. Proper hydrogen leakage sensing is required to avoid any fatal accidents along with the safety and controlled use of the equipment. Also, high sensitivity with specific selectivity, durability, and minimum operating temperature is required in the detection. For better hydrogen sensing and to enhance sensing parameters such as sensitivity and selectivity, various metal oxide semiconductors or metals have been chosen [11-12].

In this study, we report for the first time the hydrogen sensing properties of the novel metal Pd, Pt impregnated graphitic carbon nitride ($\text{g-C}_3\text{N}_4$) nanocomposite, and metal oxide ZnO impregnated graphitic carbon nitride nanocomposite at room temperature. The sensing material was synthesized by a hydrothermal and direct thermal decomposition, where melamine was used as a precursor for base material $\text{g-C}_3\text{N}_4$ and source materials for the incorporation of metal-semiconductor.

The deposition of nanocomposite based thin films on an Astro-glass substrate occurs in a temperature range of 350-400⁰C; employing a simplistic and elementary approach of the nebulizer-based ultrasonic spray pyrolysis technique. A mist of the precursor solution is produced by means of a nebulizer. Dry airflow is used to transfer the formed mist on the thermally activated substrate, which allows deposition. The crystallinity and morphology of the deposited film were confirmed by various characterizations.

The sensor was fabricated by depositing sensing materials on a screen-printed carbon electrode using a nebulizer-based spray pyrolysis setup. The crystallinity, nano morphology, elemental analysis, and chemical composition of the samples were examined by XRD, SEM, HRTEM,

EDS, and XPS. The metal nanoparticle size in g-C₃N₄ composite was calculated based on XRD data and validated by TEM data, which shows the average particle size of 3-5 nm. A dynamic response or change in electrical resistance was recorded during the presence and the absence of the analyte gas. The sensitivity obtained for the sensor at different concentrations of hydrogen gas was recorded. A comparison of the performance of both the sensors was recorded, the sensing results depict that the nebulized thin-film based Pt/g-C₃N₄ sensor shows good response and sensitivity towards the hydrogen gas and could be used for reliable hydrogen gas sensing.

Keywords: Graphitic carbon nitride; Platinum nanoparticles; Palladium nanoparticles; ZnO; Screen printed hydrogen gas sensor; Nebulizer spray pyrolysis; Room temperature hydrogen gas sensor.

Table of Contents

| | |
|--|----|
| List of Figures: | 9 |
| List of Tables: | 11 |
| Chapter 1 | 14 |
| Introduction | 14 |
| 1.1 Overview of hydrogen gas sensor: | 14 |
| 1.2 Problem Statement: | 16 |
| 1.3 Methodology: | 17 |
| 1.4 Contribution of the thesis work: | 17 |
| 1.5 Organization of the report: | 18 |
| Chapter 2 | 21 |
| Material synthesis, characterization, and deposition | 21 |
| 2.1 Instrument Overview | 21 |
| 2.1.1 Introduction | 21 |
| 2.2 Characterization tools: | 21 |
| 2.2.1 X-Ray Diffraction (XRD) | 21 |
| 2.2.2 Energy Dispersive X-ray (EDX) Spectroscopy | 22 |
| 2.2.3 X-ray Photoelectron Spectroscopy (XPS) | 22 |
| 2.2.4 Field Emission Scanning Electron Microscopy (FESEM) | 23 |
| 2.2.5 High-Resolution Transmission Electron Microscopy (HRTEM) | 23 |
| 2.2.6 Raman Spectroscopy | 23 |
| 2.2.7 Fourier Transform-Infra Red spectroscopy (FT-IR) | 24 |
| 2.2.8 UV-VIS-NIR and Photoluminescence Spectroscopy | 24 |
| 2.2.9 Nanoindentation | 25 |
| 2.3 Nebulizer Spray pyrolysis: | 32 |
| 2.3.1 Dual Beam Nebulizer-based spray pyrolysis system: | 35 |
| 2.4 Gas sensing setup: | 38 |
| 2.5 Screen printing technique | 39 |
| (i) Substrate cleaning | 39 |
| (ii) Paste optimization | 39 |
| (iii) Screen printing | 40 |

| | |
|--|----|
| Advantages of the screen printing method: | 42 |
| Preparation characterizations and testing of Nano-structured palladium impregnate graphitic carbon nitride composite for efficient hydrogen gas sensing..... | 43 |
| 3.1 Introduction: | 43 |
| 3.2 Preparation of g-C ₃ N ₄ : | 44 |
| 3.3 Preparation of Pd/g-C ₃ N ₄ Composite: | 44 |
| 3.4 Material Characterizations: | 45 |
| 3.4.1 X-ray diffraction analysis: | 46 |
| 3.4.3 Thermogravimetric analysis (TGA) | 50 |
| 3.4.4 Morphological Analysis | 51 |
| 3.4.5 Fourier-transform infrared (FTIR) spectroscopy..... | 53 |
| 3.4.6 Laser Raman Spectroscopy (LRS) | 54 |
| 3.4.7 X-ray photoelectron spectrum (XPS) analysis | 55 |
| 3.4.8 UV-VIS-NIR Spectroscopy | 57 |
| 3.4.9 Photoluminescence spectroscopy: | 58 |
| 3.4.10 Cyclic Voltammetry: | 59 |
| 3.5 Sensing Mechanism: | 60 |
| 3.6 Fabrication of Screen-printed Sensor: | 61 |
| 3.7 Gas sensing measurement and analysis:..... | 63 |
| Preparation Characterizations and testing of Pt/g-C ₃ N ₄ composite for efficient hydrogen gas sensing..... | 66 |
| 4.1 Introduction: | 66 |
| 4.2 The synthesis process of Pt/g-C ₃ N ₄ :..... | 66 |
| 4.3 Material Characterizations: | 67 |
| 4.3.1 X-ray Diffraction (XRD) | 67 |
| 4.3.2 X-Ray Photoelectron Spectroscopy (XPS):..... | 69 |
| 4.3.3 Field Emission Scanning Electron Microscopy (FESEM) and Transmission Electron Microscopy (TEM): | 71 |
| 4.3.4 Energy Dispersive X-Ray Spectroscopy (EDX): | 73 |
| 4.3.5 Fourier Transform Infrared Spectroscopy (FT-IR): | 74 |
| 4.3.6 Photoluminescence Spectroscopy (PL): | 75 |
| 4.4 Sensor fabrication..... | 76 |

| | |
|--|-----|
| 4.5 Hydrogen gas sensing: | 76 |
| Preparation, Characterizations, and testing of ZnO/g-C ₃ N ₄ composite for efficient hydrogen gas sensing..... | 81 |
| 5.1 Introduction: | 81 |
| 5.2 Preparation of ZnO/g-C ₃ N ₄ nanorods: | 81 |
| 5.3 Material Characterizations | 82 |
| 5.3.1 X-Ray Diffraction:..... | 82 |
| 5.3.2 X-ray Photoelectron Spectroscopy: | 84 |
| 5.3.3 FTIR: | 86 |
| 5.3.4 FESEM and TEM: | 87 |
| 5.3.5 Energy Dispersive X-Ray (EDX) Spectroscopy: | 90 |
| 5.3.6 Photoluminescence (PL) study: | 91 |
| 5.4 Gas sensing measurement: | 93 |
| Chapter 7 | 101 |
| Conclusion and Future Work:..... | 101 |
| Summary of the work:..... | 101 |
| Future work: | 103 |
| References:..... | 104 |

List of Figures:

| | |
|--|----|
| Figure 1 : Graphitic carbon nitride (a) thin film (b-c) Pellet. | 26 |
| Figure 2: (a) 2D FEM mesh geometry of indenter and material. (b) 3D cross-section view of the FEM under applied load condition. | 27 |
| Figure 3: (A) Experiment load-displacement curve of a pellet (Bulk S1) (B) Simulated load-displacement curve of a pellet (Bulk S1) (C) Experiment load-displacement curve of pellet (Bulk S2) and thin film (D) (a) Stress analysis (b) Plastic Strain (c) Displacement analysis..... | 30 |
| Figure 4: (a) Hardness Vs. The penetration depth of the g-CN pellet and thin film. (b) Stress Vs. Strain curve of g-CN pellet and thin film. | 31 |
| Figure 5: Schematic of dual-beam nebulizer based ultrasonic spray pyrolysis setup..... | 36 |
| Figure 6 : (a) Gas sensing setup (b) Block diagram of gas sensing setup | 38 |
| Figure 7: Flowchart of the synthesis process of Pd/g-C ₃ N ₄ nanocomposite. | 45 |
| Figure 8: Powder high-resolution X-ray diffraction of Pd/g-C ₃ N ₄ and g-C ₃ N ₄ | 47 |
| Figure 9: Powder high-resolution X-ray diffraction of and g-C ₃ N ₄ at different temperatures, concentrations, and ramp rate. | 48 |
| Figure 10: (a) EDX image of Pd/g-C ₃ N ₄ (b-e) elemental mapping of C,N,and Pd.. | 49 |
| Figure 11: Thermogravimetric (TGA) analysis of Pd/g-C ₃ N ₄ and g-C ₃ N ₄ | 50 |
| Figure 12: FESEM image of (a) g-C ₃ N ₄ (b) Pd/ g-C ₃ N ₄ . TEM image of (c) g-C ₃ N ₄ (d) Pd/g-C ₃ N ₄ (e) HR-TEM of Pd/g-C ₃ N ₄ (f) average particle size of Pd nanoparticles for image (e). | 52 |
| Figure 13: FTIR spectra of g-C ₃ N ₄ and Pd/g-C ₃ N ₄ | 53 |
| Figure 14: Raman spectra of g-C ₃ N ₄ and Pd/g-C ₃ N ₄ | 54 |
| Figure 15: (a) X-ray photoelectron spectroscopy survey spectrum of Pd/g-C ₃ N ₄ and g-C ₃ N ₄ , the deconvoluted high-resolution spectrum of (b) C 1s, (c) N 1s and (d) Pd 3d of Pd/g-C ₃ N ₄ and g-C ₃ N ₄ | 56 |
| Figure 16: UV-VIS spectra of g-C ₃ N ₄ and Pd/g-C ₃ N ₄ | 57 |
| Figure 17: PL spectra of g-C ₃ N ₄ at 500 °C, 550 °C, 600 °C | 58 |
| Figure 18: Cyclic voltammetry of Pd/g-C ₃ N ₄ and g-C ₃ N ₄ | 59 |
| Figure 19: Sensing mechanism of Pd/g-C ₃ N ₄ based resistive hydrogen gas sensor..... | 61 |
| Figure 20: (a) Carbon inter-digited electrode (b) Screen printed Pd/ g-C ₃ N ₄ sensor (c) Screen printing process. | 62 |
| Figure 21: (a) Sensor sensitivity over different hydrogen gas concentration, (b) Response and recovery time of the sensor at different hydrogen gas concentration. (c) I-V curve of Pd with different loading..... | 65 |
| Figure 22: XRD spectrum of Pt/g-C ₃ N ₄ | 68 |
| Figure 23: XRD spectra of Pt/g-C ₃ N ₄ with Pt loadings of 5% and 20%. | 69 |
| Figure 24: XPS spectra of (a) full scan spectra of Pt/g-C ₃ N ₄ (b) Pt 4f (c) N 1s (d) C 1s | 70 |
| Figure 25: (a) FESEM analysis of Pt/g-C ₃ N ₄ (b) TEM of Pt/g-C ₃ N ₄ (c) Particle size of Pt from TEM data (d) Inter-planar spacing of Pt/g-C ₃ N ₄ | 72 |
| Figure 26: (a) EDX of Pt/g-C ₃ N ₄ (b) elemental area mapping of elements (c) Pt (d) C (e) N. | 73 |

| | |
|---|----|
| Figure 27: FTIR spectrum of Pt/g-C ₃ N ₄ | 74 |
| Figure 28: PL spectra for Pt/g-C ₃ N ₄ and g-C ₃ N ₄ | 75 |
| Figure 29: (a) deposition of sensing material on top of the IDE (b) Fabricated Pt/g-C ₃ N ₄ gas sensor. | 76 |
| Figure 30:(a-b) Real-time electrical resistance response of Pt/g-C ₃ N ₄ at 1%, 4% and 10% H ₂ concentration at room temperature for drop casted and nebulized film (c) I-V curve of the sensor (d) Sensitivity of Pt/g-CN at 1%, 4% and 10% H ₂ concentration at room temperature for drop casted and nebulized film (inset) | 79 |
| Figure 31: Stability of nebulized thin-film sensor over the periods of 60 days..... | 80 |
| Figure 32: Schematic of ZnO/g-C ₃ N ₄ synthesis. | 82 |
| Figure 33: XRD spectra of (a) 0.1 ZnO/g-C ₃ N ₄ (b) 0.2 ZnO/g-C ₃ N ₄ (c) 0.3 ZnO/g-C ₃ N ₄ | 83 |
| Figure 34: XPS spectra of ZnO/g-C ₃ N ₄ and its deconvoluted peak of Zn 2p, C 1S, O 1S, N 1S. | 85 |
| Figure 35: FTIR spectra of ZnO/GCN with different ZnO content. | 86 |
| Figure 36: FESEM of ZnO/ g-C ₃ N ₄ (a) 0.1 ZnO/ g-C ₃ N ₄ (b) 0.2 ZnO/ g-C ₃ N ₄ (c) 0.3 ZnO/ g-C ₃ N ₄ (e) 0.4 ZnO/ g-C ₃ N ₄ . TEM image of (d) 0.2 ZnO/GCN (f) 0.4 ZnO/GCN (f) Interplanar spacing of ZnO/GCN. | 89 |
| Figure 37: EDX analysis of ZnO/GCN. Elemental area mapping of Zn, O, N, C..... | 90 |
| Figure 38: PL spectra of ZnO/g-C ₃ N ₄ at different ZnO concentrations. | 92 |
| Figure 39: Real-time electrical resistance response of ZnO/g-C ₃ N ₄ at 4% and 10% H ₂ concentration at room temperature. | 94 |
| Figure 40: (a) RC (b) RLC circuit arrangement for the impedance measurements..... | 96 |
| Figure 41: Impedance response of the first order and the second-order filter for Pd loading of 20% and 40% at a gas concentration of 4% and 10%, respectively. | 98 |

List of Tables:

| | |
|---|-----|
| Table 1: List of different materials prepared by using a nebulized spray pyrolysis technique. ... | 32 |
| Table 2: Spray parameters used for the deposition of film using a nebulized spray pyrolysis technique. | 37 |
| Table 3: comparison between drop casted and nebulized thin-film based Pt/g-C ₃ N ₄ sensor with their sensitivity, response and recovery time..... | 82 |
| Table 4: Response and recovery time of the ZnO/g-C ₃ N ₄ sensor at 4% and 10% concentration.... | 92 |
| Table 5: R,L,C values of a sensor at 1%, 4%, 10% concentration of analyte gas..... | 100 |

List of Abbreviations:

| | |
|------------|--|
| FEG-SEM | Field emission gun- scanning electron microscopy |
| HR-TEM | High-resolution Transmission electron microscopy |
| FTIR | Fourier transform infrared spectroscopy |
| XPS | X-ray photoelectron spectroscopy |
| UV | Ultraviolet spectroscopy |
| PL | Photoluminescence Spectroscopy |
| XRD | X-ray Diffraction |
| EDX or EDS | Energy-dispersive X-ray spectroscopy |
| AFM | Atomic force microscopy |
| GCN | Graphitic carbon nitride |
| IDE | Inter-digitated electrode |
| BE | Binding energy |
| RLC | Resister Inductor Insulator |
| MEMS | Micro Electro Mechanical System |

List of Symbols:

| Symbol | Unit | Name |
|---------------|-------------|------------------------------------|
| S | Percentage | Sensitivity |
| R_0 | Ohm | Resistivity at the presence of air |
| R_g | Ohm | Resistivity at the presence of gas |
| D | Nm | Crystallite size |
| K | -- | Scherrer's Constant |
| B | Radians | Full-Width Half Maxima |
| Θ | Radians | Peak position |
| Λ | Nm | Wavelength |

Chapter 1

Introduction

1.1 Overview of hydrogen gas sensor:

Hydrogen is increasingly essential as a clean energy source, due to its relatively easy availability and eco-friendliness. Moreover, hydrogen is efficient and renewable, and its common by-product is water [1]. For these features, hydrogen is the most promising green energy source for automotive and other industries and technologies, such as fuel cells, defence, petroleum, etc. The generation of hydrogen can also be achieved using nuclear radiation through the chemo-nuclear process [2]. This approach will help in reducing carbon emissions. Hence, hydrogen is beneficial for sustainable and clean energy future [3-4]. The use of hydrogen would resolve the high global energy demand, thus reducing global warming and air pollution [5]. However, hydrogen gas sensing is indispensable in the nuclear radiation-assisted generation of hydrogen gases as well as in space-related applications where the radioactive environment is present. Such sensing is essential because in the absence of early detection, hydrogen leakage can cause fatal accidents [6].

Various typologies have been used for sensing hydrogen [7-9], such as

1. Catalytic
2. Thermal conductivity-based
3. Electrochemical, conductometric (resistive)
4. Mechanical
5. Optical and
6. Acoustic

High concentration sensors are useful at the higher level of hydrogen gas sensing because low level/leak hydrogen sensors sometimes fail to detect the gas due to saturation and oxygen necessary for the operation.

While dealing with gas sensing, interference and poisons are the two main challenges. The intervention comes with poor selectivity towards targeted gas and toxins refer to undesirable species that cause an irreversible effect on a gas sensing. Apart from this, cross-sensitivity also plays an essential role during sensing. Cross-sensitivity refers to the sensitivity of the hydrogen sensor towards other gases [10-11].

However, given its small atomic/molecular size, hydrogen is quite susceptible to leakage. Therefore, in commercial handling of hydrogen it becomes indispensable to detect hydrogen leakage, which necessitates a reliable hydrogen sensing. Hydrogen is also susceptible to explosion in the air even at concentrations as low as 0.1 - 4 %. Detection of such low hydrogen concentrations will require high sensitivity sensors [12]. Hence, it is highly attractive to develop hydrogen sensors with high sensitivity, reliability, durability, eco-friendliness, and cost-effectiveness.

To improve the sensitivity and selectivity towards the hydrogen gas, semiconductor metal oxide or noble metals such as Au, Pt and Pd have been chosen as dopants [13-14]. Among the various hydrogen sensor types that have been explored (such as metal oxide semiconductors, thermoelectric, Schottky diodes, fiber optics, and electrochemical sensors), many researchers have employed palladium (Pd) as the active sensing material due to its uniquely strong interaction with H₂ gas [15-18]. Pd is considered as the most suitable dopant material for the detection of H₂ due to its high diffusion coefficient, high selectivity towards hydrogen, and high H₂ solubility at room temperature [19]. Pd has been extensively explored for hydrogen gas sensing through wires, films, alloys, and composites [20-25]. While depositing material for the sensor fabrication, the proper temperature of operation may be required since it was found that during the calcination process, Pd can oxidize when the temperature was excessively high and convert into PdO, which could alter the sensor performance [26].

Hydrothermal method of preparing gas sensing material gives the possibility to alter the morphology of the material, thus modulating the performance for better sensing. Hence, activity and selectivity increase due to specific morphology and atomic arrangement [27]. It is well known that change in morphology to the nano regime can improve performance [28]. Sensing properties of the nanomaterials can be enhanced by controlling their particle size, improving their surface to volume ratio, and by incorporation of dopant materials to achieve higher charge carrier mobility [29].

Metal oxide semiconductor-based hydrogen sensors have a drawback: they often require high operation temperature. On the other hand, those that can operate at room temperature reduce the sensor's cost, and their fabrication steps are not complex as their power consumption is low [19, 30]. High-temperature sensors require inbuilt heaters, which make the overall device fabrication process complex. Such sensors also suffer from other drawbacks such as long recovery time, poor stability, and slow response [31-34].

Hydrogen molecules interact with Pd to form hydrogen atoms that are absorbed by Pd to form PdH_x, which causes a phase transition from α Pd to β Pd [12]. However, pure Pd may not be the most efficient material for hydrogen sensing, because α to β phase transition is reported to be irreversible in the case of pure Pd [35], whereas an efficient sensor will require the material to revert to original form for future performance. Therefore, a pure Pd based hydrogen sensor suffers from an inferior lifespan and reliability. As a result, researchers have explored alloys and

composites of Pd such as Pd-Ag, Pd-Pt, Pd-Au, Pd-Ni, Pd-Cr, Pd-Al, Pd-NiO_x, Pd-TiO₂, Pd-WO₃, Pd-SnO₂/MoS₂, Pd/(Mg-Ni and Mg-Ti and Pd-Cu for improving reliability and lifespan of Pd-based hydrogen gas sensor [36–40].

Slaman et al. reported the implementation of Pd-capped chemo-chromic metal hydrides as a sensing layer in fiber optic hydrogen detectors. They reported a change in the optical properties of Mg-based alloys on hydrogen absorption and a drop in reflectance by a factor of 10 [40]. Rakesh et al. reported a fast response and recovery of hydrogen sensing in nanoparticle graphene composite layers of isolated Pd alloy nanoparticles dispersed onto the graphene layer. They investigated the effect of gas adsorption on electronic conduction in layers of graphene [36]. Zhang et al. demonstrated a resistive hydrogen gas sensor based on palladium-tin oxide-molybdenum disulfide (Pd-SnO₂-MoS₂) ternary hybrid, utilizing the hydrothermal route. They also investigated the synergistic effect of ternary nanostructures and the modulation of the potential barrier with electron transfer on a palladium-tin oxide-molybdenum disulfide-based hydrogen sensor [35]. Sekimoto et al. reported platinum or palladium supported tungsten oxide as the sensing material. They found that the sensor's characteristics are easily controlled by the amount of catalysts [41]. Donato Luna-Moreno et al. reported optical fiber hydrogen sensors that are based on absorption changes of evanescent fields; these fields are caused by a Pd or Pd/Au alloy thin film below the explosion limit that is 4% [42].

Gautametal. reported hydrogen sensing a property of Pd and Mg material based tri-layer, multilayer, and an alloy thin film [43]. Yumiet al. reported PdCuSi MG based capacitive MEMS hydrogen gas sensor [44]. Raghu et al. reported graphene and carbon nanotube as hydrogen gas sensors and explored the influencing factors such as large surface area, good thermal and chemical stability and also high electrical conductivity for applications such as fuel cell, hydrogen sensor and storage [45-46]. Seil et al. reported a thermo-chemical hydrogen sensor using chalcogenide thin film, but they found that the monomorphic type TCH sensor had a longer response time and longer recovery time [47]. Hydrogen dual-sensor using semiconductor metal oxide has been reported with a sensing pad in one side and Pt-based heater on the other side of an alumina substrate for the application in the fuel cell field [48]. Effect of gamma radiation was evaluated and found that higher gamma radiation can demean the sensor performance, SnO₂ based sensor has been fabricated to sense hydrogen under the radioactive environment [6] effectively. Matteo et al. reported NiO for hydrogen gas sensing in the presence of LPG gas and studied the selectivity of the sensor which is used on mobile and isolated fuel cell systems [49].

1.2 Problem Statement:

Various chemical gas sensors have been introduced for sensing purposes. But they have some drawbacks such as higher operating temperature and poor selectivity. To improve the sensor

performance, a fairly new nanocomposite based sensor has been developed. As the material is new towards sensing applications, several different batches with various concentrations were synthesized. The main aim of the thesis was to come up with a low-cost sensor that is capable of detecting hydrogen at low concentrations at room temperature. Different properties such as structural, morphological, elemental, optical, and electrical are of main interest in the synthesis and fabrication of the sensor. Furthermore, the sensor's sensing parameters need to be explored to optimize the sensor for different conditions. Sensitivity, selectivity, response time, recovery time, and reproducibility are some of the key features of any sensor which need to be characterized properly.

1.3 Methodology:

The hydro-chemical route was used to synthesize the entire nanocomposite used for the fabrication of the sensors. Various source materials were used and reduced using a reducing agent to obtain nanoparticles. To fabricate the sensor, drop-casting, screen printing, and nebulizer based techniques were used. CorelDRAW was used to design an interdigitated electrode. A carbon paste was used to print the interdigitated electrode. Thereafter, sensing material was deposited on top of pre-printed IDE. The nebulizer was used to deposit the very thin film of sensing materials on the electrode. Gas sensing was performed on a self-built sensing setup. Inlet was used to introduce the analyte gas at different concentrations. This setup has the ability to perform the temperature-related study and also has an inbuilt temperature sensor in it. The sensing was recorded based on a change in the sensor's resistance with respect to the concentration of the analyte.

RLC meter was used to explore the RLC values of the sensor. Change in RLC was recorded in the presence and the absence of the analyte. On the basis of the obtained RLC value, Pspice modeling was done to match the experiment and simulation results.

1.4 Contribution of the thesis work:

There are the following contributions have been made in this thesis:

- 1. Synthesis of different nanocomposites for hydrogen gas sensing:*

Three different nanocomposites have been prepared, namely Pd/GCN, Pt/GCN, and ZnO/GCN, by using direct pyrolysis followed by a hydrothermal approach. All the synthesized composites were tested in the presence of hydrogen gas.

- 2. Characterization of prepared nanocomposites:*

All synthesized materials have been characterized by several techniques to evaluate various parameters of the materials, such as phase composition, crystallinity, morphology, optical, vibration, rotation, and bonding properties, I-V characteristic, etc.

All the characterization confirmed the formation of the desired material with the required parameters for efficient performance as prominent hydrogen gas sensing material.

3. *Sensor fabrication and testing:*

The sensors were fabricated on a glass substrate by drop-casting, screen printing, and nebulizer spray pyrolysis techniques. Carbon paste-based interdigitated electrodes were fabricated for all types of the gas sensor. To deposit the sensing film on top of the IDE drop casting, screen printing and nebulizer spray pyrolysis techniques were used. For the sensing hydrogen gas, a glass chamber was fabricated with inlet and outlet for the purging of gas.

4. *Deposition and optimization of thin film deposited by nebulized spray pyrolysis system:*

For the deposition of the sensing film, we built a dual-beam based ultrasonic and jet nebulizer spray pyrolysis setup. The system was optimized for several parameters. The film was deposited on top of IDE. To optimize the film and the quality of the deposited film, various characterization and measurements were performed.

5. *LCR measurements and modeling of sensor:*

Fabricated sensor was tested for L, C, and R data of the sensor in LCR meter. Pspice Modeling of the sensor was performed on obtained data. Also, changes in the parameters were monitored in the presence and absence of the analyte gas.

1.5 Organization of the report:

The subsequent chapters are organized as follows:

In chapter 2, material synthesis, characterization, and deposition of the material are described in detail. Various characterization methods have been used to classify the synthesized material. Crystallinity, morphology, optical, electrical properties have been discussed. Screen printing technique, nebulizer based deposition, and gas sensing setup are described in this chapter.

In chapter 3, "*Preparation Characterizations and testing of Nano-structured palladium impregnate graphitic carbon nitride composite for efficient hydrogen gas sensing*," palladium nanoparticles were incorporated into graphitic carbon nitride (g-C₃N₄) by a fairly new chemical process that uses ammonium tetrachloropalladate as a Pd metal nanoparticle source along with an appropriate reducing agent. Similarly, for the synthesis of g-C₃N₄, urea was used as a

precursor at 550 °C. g-C₃N₄ and Pd/g-C₃N₄ were characterized by X-ray diffraction (XRD), scanning electron microscope (SEM), transmission electron microscopy (TEM), UV-VIS-NIR spectroscopy, Raman spectroscopy, Fourier transform infrared spectroscopy (FTIR), and energy-dispersive X-ray spectroscopy (EDS). Pd-dispersed graphitic carbon nitride film was deposited on an interdigitated carbon electrode by using a screen printing technique. In this chapter, the sensor is tested at different concentrations and thicknesses. Sensor parameters such as response and recovery time have been explored. The overall results in this chapter show Pd/g-C₃N₄ nanocomposite as an efficient hydrogen sensing material.

In chapter 4, *“Preparation Characterizations and testing of Pt/g-C₃N₄ composite for efficient hydrogen gas sensing.”*

The sensing material was synthesized by using a hydrothermal approach, where melamine and chloroplatinic acid hexahydrate were used as precursors. The sensor was fabricated by depositing sensing materials on a screen-printed carbon electrode by jet nebulizer based spray pyrolysis setup. The crystallinity, nano morphology, elemental analysis, and chemical composition of the samples were examined by XRD, SEM, HRTEM, EDS, and XPS. A drastic change in electrical resistance was recorded during the presence and the absence of the analyte gas. The sensitivity obtained for the sensors at different concentrations is discussed. The sensing results are discussed in detail, it is concluded that the Pt/g-C₃N₄ shows a good response towards the hydrogen gas and could be used for reliable hydrogen gas sensing.

In chapter 5, *“Preparation Characterizations and testing of ZnO/g-C₃N₄ composite for efficient hydrogen gas sensing”*, the preparation of the ZnO/g-C₃N₄ material has been discussed. The ZnO has been prepared at different concentrations using fairly simple direct pyrolysis of the mixture of the precursors. The crystallinity, nano morphology, elemental analysis, and chemical composition of the material were examined by XRD, SEM, HRTEM, EDS, and XPS. This chapter also discusses the sensing study at different concentrations of ZnO/g-C₃N₄.

In chapter 6, “RLC modeling of the gas sensor”, RLC modeling of the gas sensor is discussed at the various operating frequency. The Pspice modeling of the sensor was explored at different concentrations of the gas.

Chapter 2

Material synthesis, characterization, and deposition

2.1 Instrument Overview

2.1.1 Introduction

This chapter describes a brief overview of the tools used for the characterizations. This chapter also describes the material synthesis and characterization performed on the prepared samples.

2.2 Characterization tools:

2.2.1 X-Ray Diffraction (XRD)

XRD is a characterization tool that is used to identify the phase of any crystalline material. It is a technique used to describe the crystal structure and spacing of atomic planes (d). In XRD, X-ray is being generated by a cathode ray tube, which is then filtered by sophisticated filters to produce monochromatic radiation. Proper optics is then used to concentrate the X-ray beam, and finally, the generated beam is subjected to samples for various studies.

In XRD, diffraction patterns are generated when incident rays strike to the sample. It is to be said that the interference would be constructive if it follows the Bragg's law which states,

$$n\lambda = 2d\sin\theta$$

Where n is the order of reflection, λ is the wavelength of the incident X-rays, d is the interplanar spacing, and θ is the angle of incident.

Conversion of diffraction peaks to its corresponding lattice spacing d allows the identification of different materials as every material has a different d spacing.

Powder X-ray diffraction (XRD) patterns were recorded by using the RigakuSmartLab X-ray diffractometer with Cu K α radiation ($\lambda = 1.5405 \text{ \AA}$). All measurements were taken in the 2θ range of $5\text{--}100^\circ$ with a step size of 0.01° .

2.2.2 Energy Dispersive X-ray (EDX) Spectroscopy

EDX is used to analyze the elemental composition. As an operating principle, high energy X-ray is incident on the sample as a result of core electron ejection from the atom. It follows Moseley's law, according to which frequency of light released after the incidence of the X-ray is related to the atomic number of the atom. To remove the core electron from the atom, high energy X-ray is incident on the sample. As a result, an electron from the core-shell is knocked out of the orbit and an electron from a higher energy level releases energy and fills that space. The amount of energy released during this process is different for different materials. Hence, by examining the released energy, one can identify the different elements along with the proportion by which they are present in the material.

The energy-dispersive X-ray spectra were generated using a JSM-7600F (FEG) scanning electron microscope.

2.2.3 X-ray Photoelectron Spectroscopy (XPS)

XPS, also known as ESCA, is used for chemical and elemental analysis of the material. This technique can also be used to determine the depth profile of the material. There is no restriction in how it comes to the material, unlike EDX, which can penetrate the sample at a specific depth, i.e., 5 nm. The basic principle of the XPS is the first sample is illuminated/incident by X-ray sources such as Al K α or Mg K α . Emitted photoelectron from the sample surface is then observed with respect to its states, chemical bonding, etc. Materials are then analyzed on the basis of kinetic energy (KE) of ejected photo-electrons from the sample surface. Binding energy can be evaluated by simply calculating the KE of ejected photo-electrons.

Two types of X-rays are used Mg K_α and Al K_α . The peak position and intensity of the peak in the spectrum provide information related to chemical states for a given element.

XPS spectra were recorded using AXIS Supra, Monochromatic (Al K_α) 600 W, X-ray source, 1486.6 eV.

2.2.4 Field Emission Scanning Electron Microscopy (FESEM)

It is an imaging technique in which an electron beam strikes the sample surface and generates output in the form of an image. SEM gives information about the surface and morphology of the sample. The conductive surface is required to get the required quality result/imaging. For an insulating sample, a thin layer of coating is necessary for imaging.

Scanning electron microscope (SEM) images were generated by a JSM-7600F (FEG) scanning electron microscope.

2.2.5 High-Resolution Transmission Electron Microscopy (HRTEM)

HRTEM is used for the imaging of the sample by a high energy electron beam, which is allowed to transmit through a thin specimen. This technique is used to determine the particle size in the sub-nanometer scale. This tool also provides inter-planar spacing of crystalline structure between the layers from the electron-diffraction pattern.

Philips CM 200 was used to record the transmission electron microscopy (TEM) images.

2.2.6 Raman Spectroscopy

Raman spectroscopy is used to analyze vibration and rotational modes of molecules. Raman spectroscopy is generally used for the unique fingerprinting of molecules. Raman scattering is based on inelastic scattering of photons.

As an operating principle, a monochromatic light source such as a laser is used to illuminate visible, near-infrared, UV, or X-ray. This laser light then strikes the molecules at vibration mode as a result of the interaction energy, laser photon is shifted either up or down, respectively.

The Raman spectra were recorded using a Horiba HR 800 Laser Raman Spectrometer in the range of 500–1800 cm^{-1} . An argon laser (535 nm) was used here.

2.2.7 Fourier Transform-Infra Red spectroscopy (FT-IR)

FT-IR is a spectrometric technique that operates in the range between NIR to FIR spectrum. FT-IR collects data by interferometer by getting the infrared spectra of the sample, followed by performing the Fourier transform on the data. Thereafter, the FT-IR spectrometer collects and digitizes the interferogram, performs FT function, and displays the spectrum.

Here, the Bruker, a 3000 Hyperion Microscope with a Vertex 80 FTIR System FTIR spectrometer in the range 500–4000 cm^{-1} was used. The samples were prepared by using KBr pelletizer.

2.2.8 UV-VIS-NIR and Photoluminescence Spectroscopy

This is an optical technique based on the amount of light absorbed by a chemical substance in the range between UV - VIS to NIR. Measurement is done by comparing the actual with a reference. The result is often recorded in terms of transmission, reflection, and absorption. This method is often used to determine the light absorption using the Beer-Lambert law. Photoluminescence (PL) works on a principle of light emission from the material after the absorption of the photon energy. PL works as a principle where it absorbs certain energy from incident photons; as a result, electron-hole pair breaks and electron from the valence band excites to the conduction band and stay there for some time. After the relaxation time, the electron re-emits the photon energy, which is equal to the bandgap energy of that material. Hence, this method is used to find out the bandgap of any material.

The optical properties were investigated using Thermo Scientific UV-VIS-NIR spectroscopy in the range of 200-800 nm.

2.2.9 Nanoindentation

Nanoindentation is a very prominent characterization technique to explore the mechanical properties of the material in thin film and bulk form. This process has been explored to obtain various mechanical properties such as hardness, elastic modulus, stress, strain, plasticity, endurance loads, optimal thickness, and optimal critical load [50]. Nanoindentation testing at a very low load is a successful technique for examining the mechanical attributes of ceramic, metallic, and inter-metallic thin films as well as bulk films. Hardness, yield strength, and elasticity modulus are the basic parameters for mechanical invention [55]. Nano hardness measurements are attractive because they can be done on a variety of materials, metals and ceramic, and supply data on its elastic and plastic deformation behavior. The simulation output relies on the size of the meshing, radius, and geometry of the used indenter tip. It also depends on the hardening law imposed to the model and a little bit on the friction coefficient [6/56]. Researchers have explored experimental techniques as well as a simulation method to extract the desired mechanical properties from the nanoindentation process [57-62].

The mechanical property of graphitic carbon nitride remains relatively unexplored. Mortazavi et al. (2014) used classical molecular dynamics simulations to explore the thermal conductivity and mechanical response of the graphitic carbon nitride and found that the film has a remarkable elastic modulus [63]. Abdullah et al. (2016) used density functional theory (DFT) to obtain the elastic constants and the strain responses of graphitic heptazine. They also studied the bandgap dependence on the tensile strain of the material within the elastic region [64]. Ajori et al. (2017) explored density functional theory to obtain the mechanical properties of graphene-like graphitic carbon-nitride (g-C₃N₄) such as Young's modulus and Poisson's ratio [65].

2.2.10 Finite Element Model (FEM)

FEM approach with experimental data validation was explored, which has so far not been reported. The finite element technique is used for considering the very complex stress-strain field of thin, tough coatings and bulk substrates subjected to a nanoindentation process. The

indentation process was simulated with the use of the ABAQUS finite element software package [53]. We compared experimental data with the simulated result. We have also investigated several mechanical properties to develop an improved understanding of the material in this regime. The investigated material was graphitic carbon nitride pellet and thin film. The numerical analysis allowed the plastic deformation history during indentation to be tolerated. The system was simulated by a 2D axisymmetric model. The element type used for the material block is CAX4R. The indenter was selected as a rigid surface. A comparison between the experimental data and numerical results exhibited that the FEM approach is capable of replicating the loading-unloading curve of an nanoindentation test. The nanoindentation process is a very prominent method to examine the mechanical properties of an unknown material with or without the substrate. The nanoindentation process works on a principle where a certain amount of force is exerted on the sample surface, and the corresponding displacement value is measured [54]. Because the indentations made are too small to be easily observed, the size of the indentation is determined from the measured depth of indentation and the calibrated shape of the indenter.

Experiment details

Sample preparation:

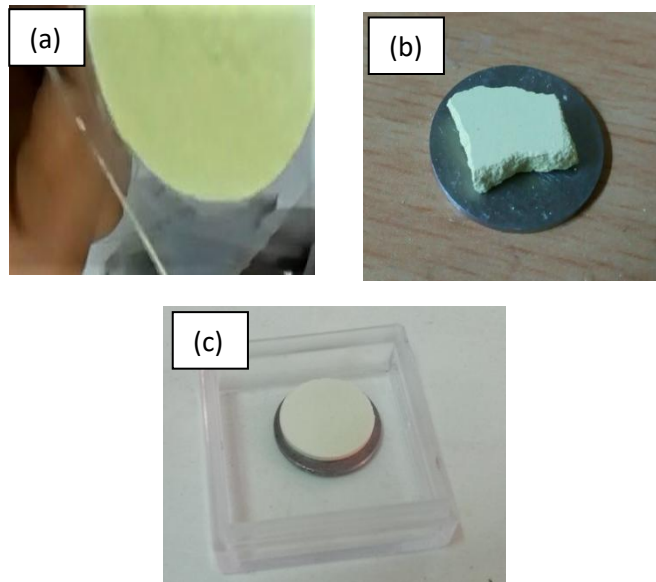


Figure 1 : Graphitic carbon nitride (a) thin film (b-c) Pellet.

The nanoindentation process was done on the graphitic carbon nitride pellet. Bulk graphitic carbon nitride powder was ground well into the fine powder with the use of mortar and pestle. Then, the fine powder was put into the one-inch cylindrical pelletizer system. A load of 7-ton was exerted on the powder sample to make a pellet of g-C₃N₄. Finally, approximately 2 mm and 1 mm thick graphitic carbon nitride pellets named bulk S1 and bulk S2 were obtained from the process for the nanoindentation process to evaluate its mechanical properties. The thin film of g-C₃N₄ was obtained by a thermal vapor condensation method using melamine as a precursor [66].

Nanoindentation study was done using Hysitron Inc Minneapolis, USA, Model: TI-900 that had a load range of minimum up to 10 μ N and maximum up to 500 mN, a displacement range of maximum Z-displacement up to 5 μ m and max X-displacement up to 15 μ m.

FEM analysis was done by using Abaqus 6.14 with the appropriate dimensions. A fine 2D axisymmetric mesh was created, as shown in Figure 2(a), to replicate the actual structure in the simulation. It is always advisable to use meshes as fine as possible. Fine mesh might take a longer time to run the simulation, but the result will be more accurate. A conical tip, which was having 70.2 half angles, is used to represent a Berkovich indenter, which has the geometry of a three-sided pyramid.

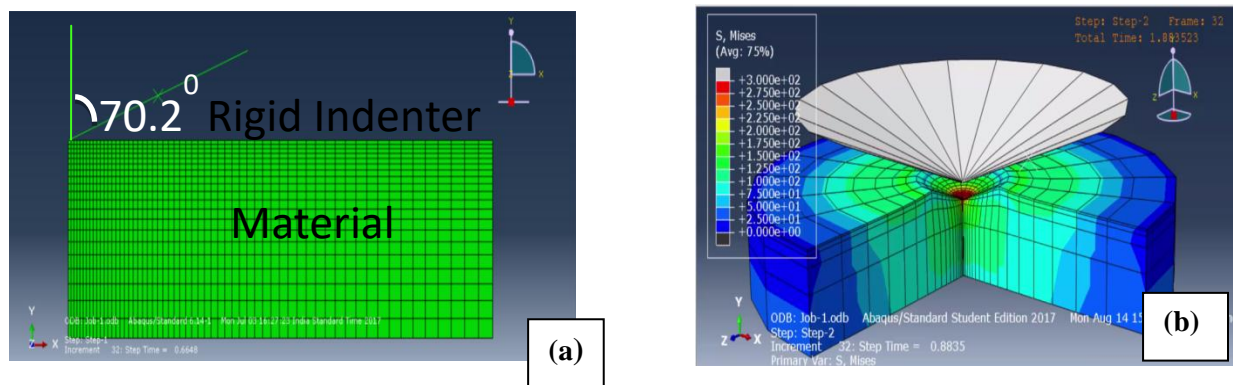


Figure 2: (a) 2D FEM mesh geometry of indenter and material. (b) 3D cross-section view of the FEM under applied load condition.

because it is a 2D model, taking lesser time to complete the simulation compared to a 3D model, so it generally takes lesser time to complete the simulation process, unlike a 3D model. 2D axisymmetric indentation modeling with easy-to-understand 270-degree cross-section view is shown in Figure 2(b), where it is fairly easy to understand how strain, plastic deformation, and displacement progress gradually as the structure is subjected to a certain amount of loading. Different boundary conditions were applied to get the best and close fit to the experimental results. The indenter tip was chosen as a rigid body and the material as a deformable body. The indenter was selected as a master and material as a slave. Proper material properties such as elasticity, plasticity were defined.

The boundary conditions:

Bottom edge of the material block created from the initial step: $U1 = U2 = UR3 = 0$

The left edge of the material block created from the initial step: $U1 = UR3 = 0$

A reference point on the indenture created from the initial step: $U1 = UR3 = 0$

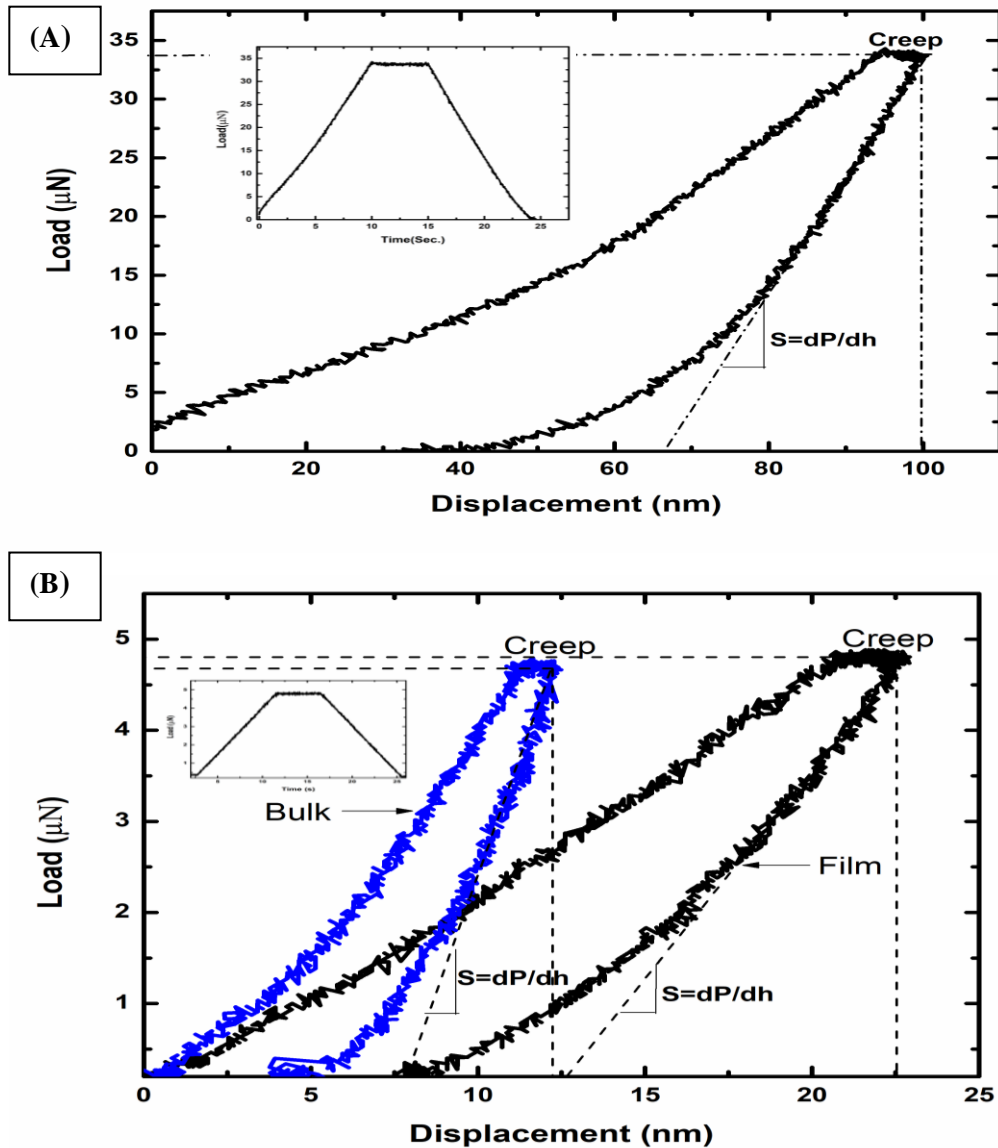
Reference point on the indenter from the contact step: $U2 = -0.01342$ unit/seconds. This boundary condition pushes the indenter into the material block.

The reference point on the indenter from the contact step: $U2 = \text{Zero}$. After applying this final boundary condition on the simulation model, it brings the indenter tip to its previous position.

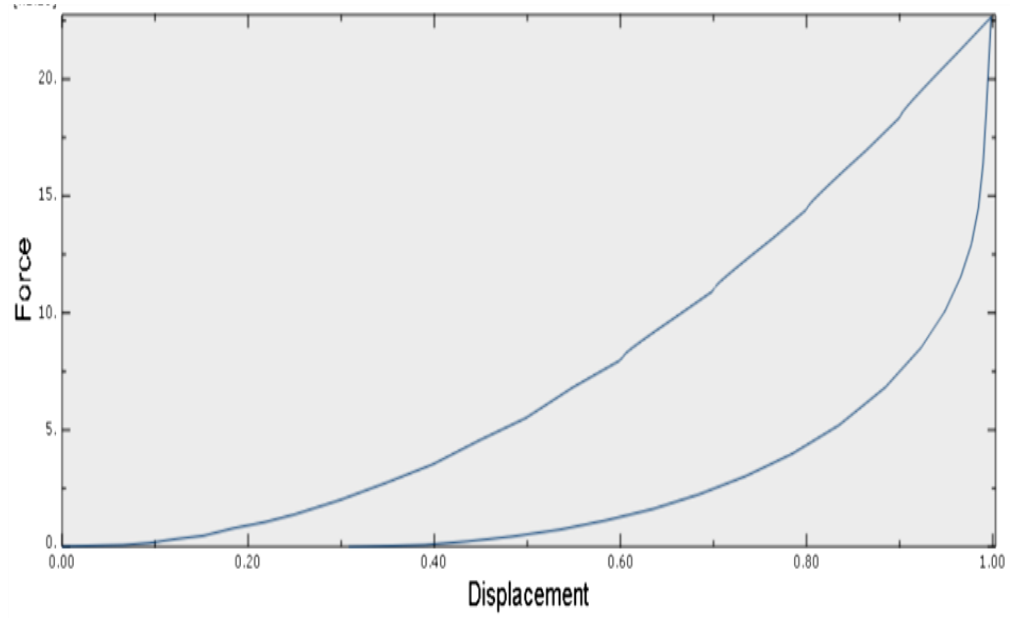
Below, simulation results illustrate the stress, displacement and plastic strain exerted on the $\text{g-C}_3\text{N}_4$ pellet

The numerical analysis of the given structure was performed in the finite element method with the applied load in the range of μN and displacement in the order of nm. The appropriate load-displacement curve was obtained after applying several boundary conditions and iterations. Figure 3 (A, C) shows the load-displacement curve as a result of the applied condition for both pellets and film. Loading was done till the penetration depth of 100 nm with the applied load of 30 μN for pellet S1. It is very difficult to analyze the extremely thin film of any material on a

substrate due to the impact of the substrate effect during the indentation process. To eliminate the substrate effect, a 10% rule was considered for a film with an applied load of 5 μN and a penetration depth of 25 nm. The experimental results, as shown in Figure 3 (A), depict the load-displacement curve of the g-C₃N₄ pellet S1, and it closely matches the simulated results, as shown in Figure 3 (B). Simulated results were used to get other important parameters of the materials such as stress, strain, plasticity, etc. as shown in Figure 3 (D) (a). The figures show how stress exerted into the sample is subjected to an increment of applied load, color gradient shows how stress spreads throughout the sample with red being higher and blue being the lower side of the applied stress to the sample. A similar study was done for plastic strain and displacement, which is shown in Figure 3 (D) (b) and (c).



(C)



(D)

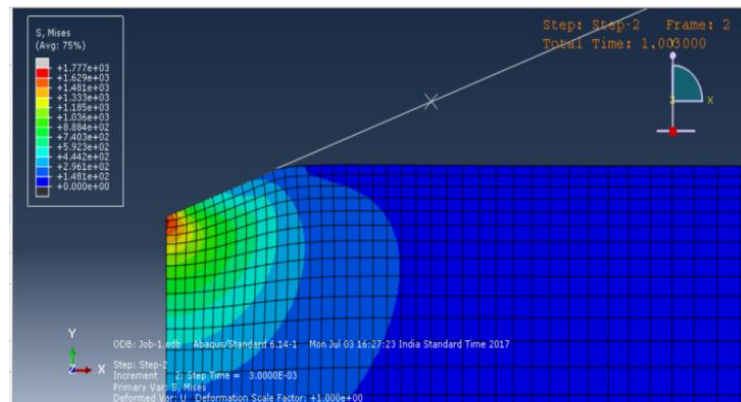
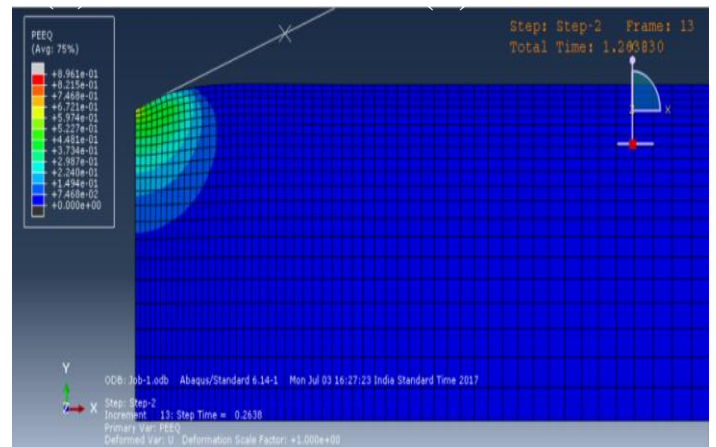
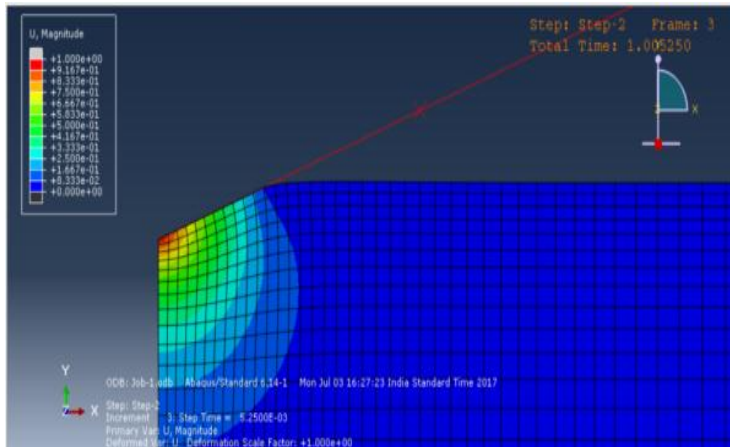


Figure 3: (A) Experiment load-displacement curve of a pellet (Bulk S1) (B) Simulated load-displacement curve of a pellet (Bulk S1) (C) Experiment load-displacement curve of pellet (Bulk S2) and thin film (D) (a) Stress analysis (b) Plastic Strain (c) Displacement analysis

Stress-strain curves for both pellets and thin films are shown in Figure 4(b). For g-C₃N₄ pellet, stress is the linear function to strain for a certain period of time that indicates that it obeys Hooke's law whereas the elastic region thin-film follows a straight curve but does not obey Hooke's law. From the curve, it was observed that g-C₃N₄ shows polymer-type behavior [67-69]. It was also observed that almost identical stress-strain curves were obtained for a film as well as pellets under a fixed applied load.

Figure 4(a) represents the hardness vs. penetration depth plot obtained from nanoindentation experimental data for g-CN pellet and thin film. It was observed that the higher the hardness, the lower would be the penetration depth and vice versa.

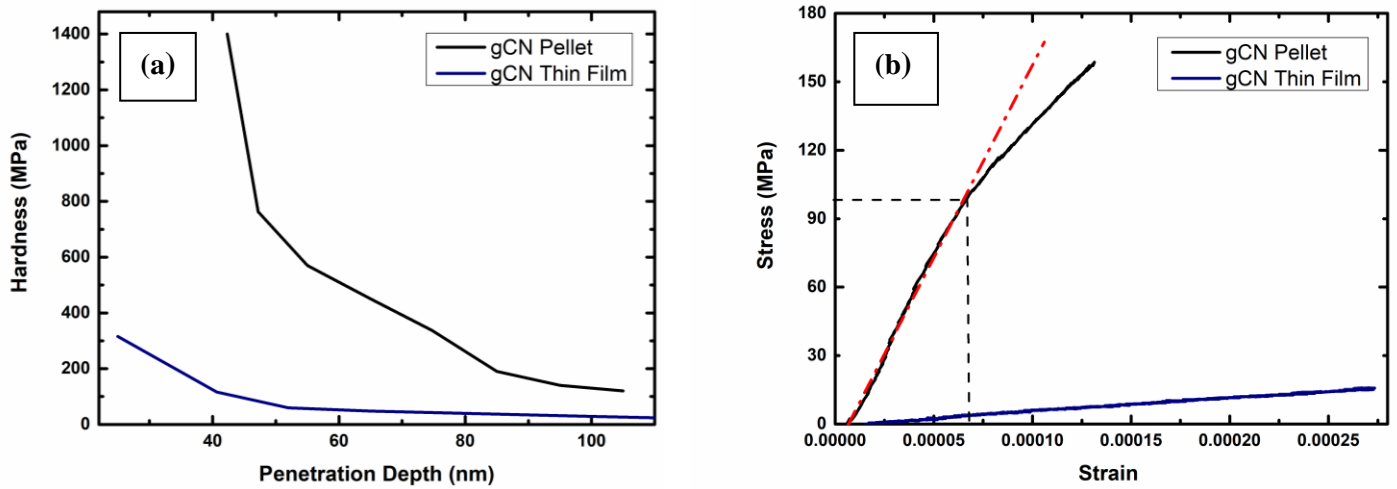


Figure 4: (a) Hardness Vs. The penetration depth of the g-CN pellet and thin film. (b) Stress Vs. Strain curve of g-CN pellet and thin film.

2.3 Nebulizer Spray pyrolysis:

Nebulizer spray pyrolysis is an adaptable, easy, cost-effective, time-saving, and efficient way of growing thin films at a low temperature and atmospheric pressure [70–71]. Scalability to deposition across a large area can be achieved through this technique. Deposition of binary and ternary oxide thin films such as $\text{Sn}_x\text{Zn}_{1-x}\text{O}_{1+x}$, MnS, graphene, In_2S_3 , CdIn_2S_4 , $\text{Cu}_2\text{ZnSnS}_4$, MgO, bismuth sulfide, gallium oxide, Y_2O_3 , $\text{Zn}_{(1-x)}\text{Mg}_x\text{O}$, Mn-doped ZnO, calcium phosphate, iron oxide, chromium oxide, tin-doped zinc oxide, Cd-doped SnO_2 , $\text{Gd}_x\text{Zn}_{(1-x)}\text{O}$, and Na-doped ZnO as listed in Table 1, have been achieved using the nebulized spray pyrolysis technique [70,72–86]. Mariappan et al. reported the advantage of using nebulized spray pyrolysis over other spraying techniques, such as less material requirements with controlled spraying of the solution, which lead to uniform and thin film deposition [72]. In addition, Fu et al. reported the simplicity of the technique and the requirement of low-cost raw materials [74]. Ebsenso et al. reported the deposition of a quaternary oxide film, $\text{Ln}_{(1-x)}\text{Sr}_x\text{CoO}_3$ ($\text{Ln} = \text{La}, \text{Nd}, \text{and Gd}$), and ternary oxide SrRuO_3 thin films through the nebulized spray pyrolysis technique. It was determined that the thin film that was prepared by this technique shows low film resistivity, which can be explored for use as an efficient electrode in various situations [74].

Table 1: List of different materials prepared by using nebulized spray pyrolysis technique

| Thin film | Spray (Precursors) | Solutions | Temperature (°C) | Substrate | References |
|----------------------|---|---|---------------------|-----------|--|
| Jet Nebulizer | | | | | |
| MnS | Manganese (MnCl_2) and thiourea EDTA. | chloride ($\text{CS}(\text{NH}_2)_2$), | 350 °C | Glass | M. Girish a, R. Sivakumar b,*, C. Sanjeeviraja c, Y. Kuroki d (2015) [72] |

| | | | | | | |
|--|---|-------------------|--|---------|--|--|
| Sn_x Zn_{1-x} | | | | | | R. Mariappan,1,2 V. Ponnuswamy,1 P. Jayamurugan, (2013) [74] |
| O_{1+x} | Zinc chloride, NaOH solution, tin (IV) chloride, EDTA, Deionized water | 400 °C | | Glass | | |
| Graphene | Graphene oxide, Deionized water, Dextrose | 200 °C | | Glass | | J. Tamil Illakkiya, P. UshaRajalakshmi, Rachel Oommen(2016) [75] |
| In₂ S₃ | Indium chloride, thiourea solutions with the volume ratio of 2:3 respectively. The precursors were dissolved in double Distilled water and isopropyl alcohol. | 200 °C to 350 °C | | Glass | | J. Raj Mohamed1,3 • C. Sanjeeviraja2 • L. Amalraj1 (2016) [76] |
| CdIn₂S₄ | Solution of CdCl ₂ , In ₂ Cl ₃ and CS(NH ₂) ₂ | 200 °C to 450 °C | | Glass | | J.Raj Mohamed a,c, C. Sanjeeviraja b, L. Amalraj a,* (2016) [77] |
| Ultrasonic Nebulizer | | | | | | |
| Cu₂ZnSnS₄ | cupric chloride (0.008M), zinc chloride (0.005M), stannic chloride (0.005M) and thiourea (0.04M) was used | 350 °C and 500 °C | | glass | | Sheng Huang1, Wenjun Luo1,3 and Zhigang Zou1,[78] |
| MgO | magnesium acetate was used with ethylene glycol | 380–600 °C | | Si(100) | | Xiaorong Fu a, GuangmingWu b, |

| | | | | |
|--|--|---------------------------------|--|--|
| | monomethyl ether | | | Shigeng Song [79] |
| bismuth sulphide | Bi(NO ₃) ₃ and thiourea | 150–450°C | Si(1 1 1) and glass | Sheng-Yue Wang*, You-Wei Du[80] |
| Gallium Oxide | Gallium acetylacetonate (GAAC) Dissolved in a mixture of 1 part deionized water and 1 part methyl alcohol. Glacial acetic acid was added ~5 mL/L! to obtain a complete dissolution of the source material | 300 °C to 500 °C in 25 °C steps | Si | A. Ortiz,a,z J. C. Alonso,aE.Andrade,b and C. Urbiola [81] |
| Y₂O₃ | Yttriumacetylacetonate, Y(CH ₃ COCHCOCH ₃) ₃ | 350–400 °C | Si(1 0 0) | Sheng-Yue Wang*, Zu-Hong Lu [82] |
| solid oxide fuel cell anode electrode | Nickel(II) nitrate hexahydrate (98%). The deposition mechanism of modified spray pyrolysis. N ₂ NiO ₆ ·6H ₂ O; Alfa Aesar), cerium(III) nitrate hexahydrate (99.5%, Ce(NO ₃) ₃ ·6H ₂ O; Alfa Aesar) and gadolinium(III) nitrate hydrate(99.9%, Gd(NO ₃) ₃ ·xH ₂ O, x ≈ 6; Alfa Aesar) | 250-350°C | yttria stabilized zirconia (YSZ) substrate | Lin Liu, Gap-Yong Kim *, Abhijit Chandra [83] |

| | | | | |
|--|--|------------|---|--|
| Zn_{1-x}Mg_xO | Zn(CH ₃ COO) ₂ ·2H ₂ O and Mg(CH ₃ COO) ₂ ·4H ₂ O | 400 °C | Single-crystal Si (100) wafers and quartz glass | Xia Zhang, Xiao Min Li *, Tong Lai Chen, [84] |
| Mn-doped ZnO | zinc nitrate (Zn(NO ₃) ₂ ·6H ₂ O) and manganese (Mn(NO ₃) ₂ ·6H ₂ O) | 400 °C | glass substrate | Preetam Singh, Ajay Kaushal, Davinder Kaur [85] |
| Calcium Phosphate | Ca(NO ₃) ₂ ·4H ₂ O (1 L, 0.5 M) | 500 °C | glass | Dominic Walsh,* Laura Arcelli, Vicky Swinerd, [86] |
| iron oxide | iron acetylacetonate, a mixture of DI water and anhydrous ethanol with a volume ratio of 1:1, | 200–540 °C | Si(111) | Shengyue Wang a, Wei Wang b,), Wenzhong Wang [73] |

2.3.1 Dual Beam Nebulizer-based spray pyrolysis system:

To fabricate films, a new deposition system/setup is proposed that comprises a dual beam ultrasonic nebulizer setup, as shown in Fig5. The proposed setup consists of two ultrasonic nebulizers, a compressor as a carrier gas, a rotating disk for controlled deposition, a sample holder to hold the substrates (such as glass, silicon), a heater (up to 1000 °C), control systems and readout devices. Operating the system is simple. The required amount of liquid sample is poured into the ultrasonic nebulizer's vessel. The system provides the freedom to make a composite or a layer of two different materials during the process of deposition, which is enabled by the two-beam functionality of the nebulizer. The sample holder is attached to the heater, which can heat up the sample to the required temperature to achieve an appropriate adhesiveness with uniform film thickness. Two identical rotating disks are placed, one on top of the other, in such a manner that one disk moves clockwise or counterclockwise by using a stepper motor that is connected to

the control system, as shown in Fig5(a). The compressor is used as a carrier gas for the ultrasonic nebulizer to dispose of the generated aerosol or mist of the poured material during the nebulization process. Finally, the exhaust that is connected to the top of the setup works as an outlet and removes the excess mist that may be generated within the chamber. The exhaust also provides directionality for better film deposition.

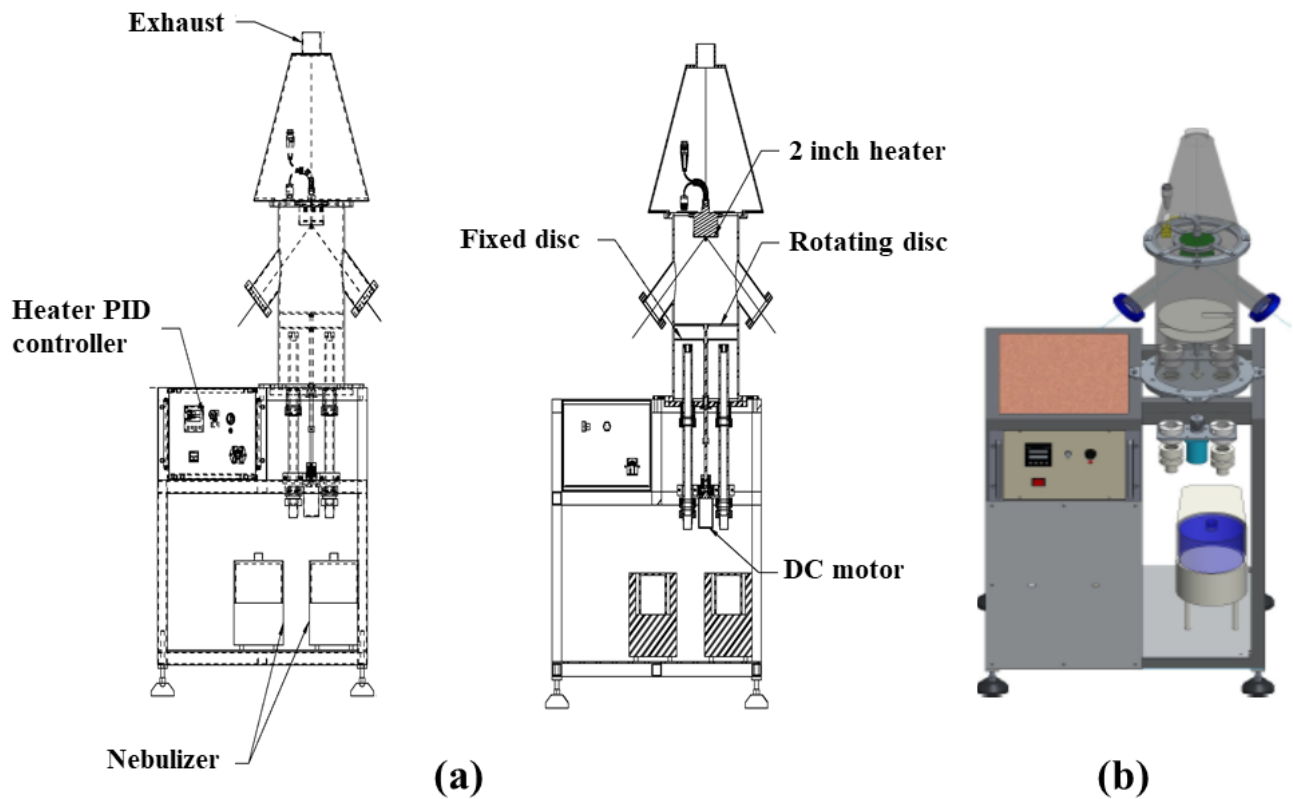


Figure 5: Schematic of dual-beam nebulizer based ultrasonic spray pyrolysis setup.

Table2:Spray parameters used for the deposition of the film using nebulized spray pyrolysis technique

Spray parameters used for the deposition of the film using a nebulized spray pyrolysis technique.

| <i>Spray Parameters for thin film deposition</i> | |
|---|--|
| Spray Technique | Ultrasonic |
| Air Blast | Atomizer |
| Ultrasonic operating frequency (MHz) | $1.7 \pm 10\%$ |
| Droplet size (μm) | 2.8 |
| Solution flow rate (ml/min) | 0.1–3 |
| Distance from the heater to the substrate (cm) | 4–5 |
| Solvent | DI water and Methanol |
| Precursor | g-C ₃ N ₄ , Pd/g-C ₃ N ₄ |
| Concentration (mol/l) | |
| Deposition Temperature (°C) | 350 |
| Annealing Temperature (°C) | 450 |
| Substrate | Glass |

2.4 Gas sensing setup:

The gas sensing setup was made with an inlet and an outlet for the sensing of analyte gas, as shown in Fig 6(a)&(b). The gas cylinder was connected to the inlet with a push-pull connector. Similarly, the outlet was connected to the vacuum pump to evacuate gases present inside the gas chamber before the measurement for an accurate reading. A removable 2-inch heater with temperature controller and monitor was introduced to the chamber for temperature-related studies. To record the data during sensing, the sensor was connected to the digital multimeter by maintaining the chamber leakage free. Sensing was performed and data were recorded from the DMM, further parameters were calculated from the obtained data.

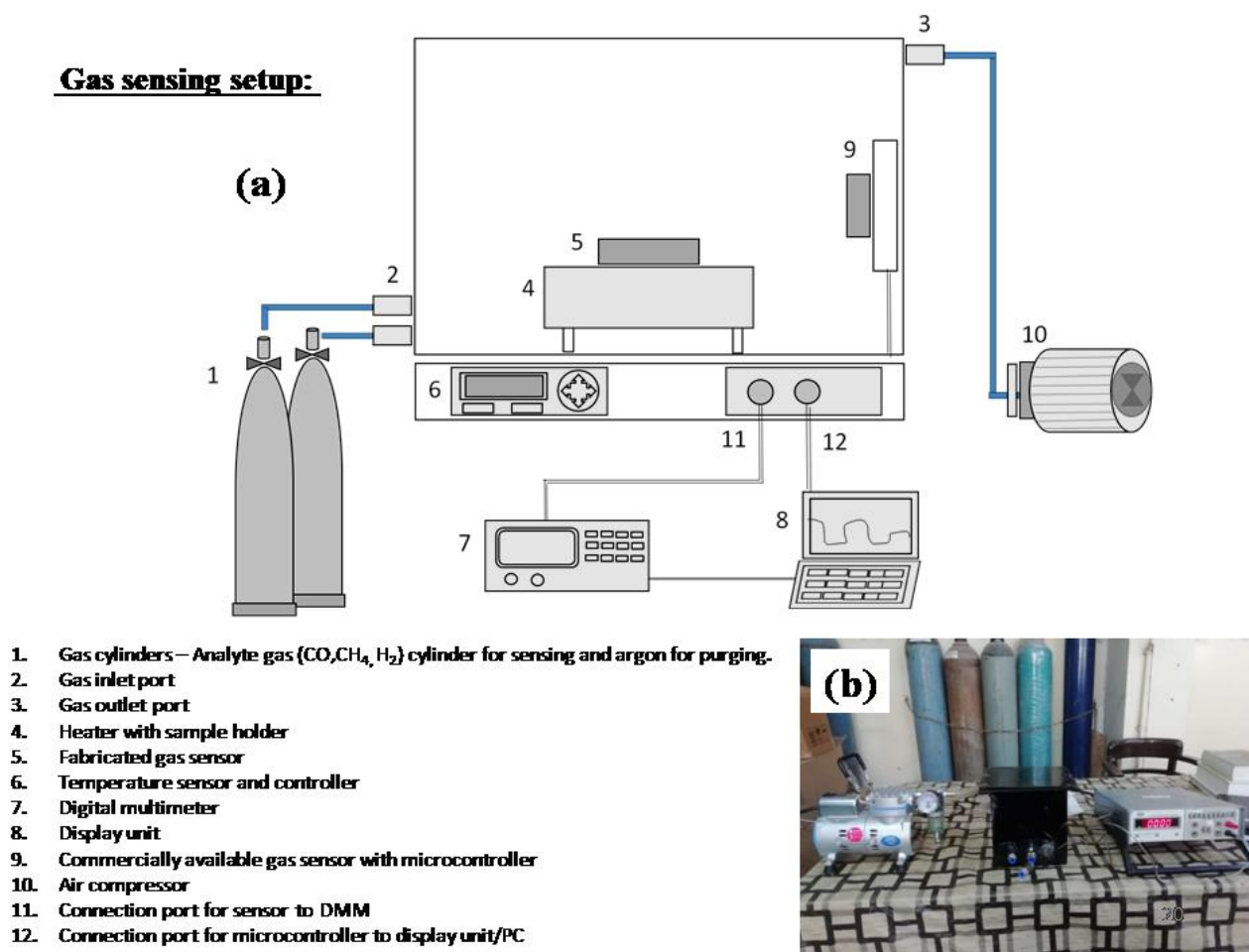


Figure 6 : (a) Gas sensing setup (b) Block diagram of gas sensing setup

2.5 Screen printing technique

a) Thick film fabrication

To improve the sensor's important parameters such as selectivity, sensitivity, response, and recovery time, the deposition technique plays a critical role in enhancing the entire characteristic.

A sensor could be fabricated in the following ways:

1. Thin film
2. Thick film
3. Pellets

Amongst the various approaches, screen printing is considered to be one of the easiest to use. This approach has the ability for large scale enhancement of the product because of its advantages such as small size, portability, versatility, low cost, and mass production.

Screen printing technique uses sensing material or any functional material in the form of a paste with optimized viscosity by adding some organic binding. Glass or alumina substrates are being used to deposit materials.

The following steps are required to deposit a thick film using screen-printing technology:

- (i) Substrate cleaning
- (ii) Paste optimization
- (iii) Screen printing

(i) Substrate cleaning

In the cleaning process, a substrate such as glass or alumina was properly cleaned. In our case, we used glass slides (3cm x 3cm) as a substrate for the screen printing process. Firstly, all the glass slides were properly cleaned by soap solution to remove the mechanical impurities such as oil and grease. To remove the organic impurities, piranha cleaning was performed in which H_2SO_4 and H_2O_2 were taken in a 3:1 ratio, and glass slides were dipped in the solution for 30 minutes. After this, substrates were cleaned and dried in the muffle furnace.

(ii) Paste optimization

For paste formulation, functional material, ethylcellulose (EC) as an organic temporary binder and terpineol as a solvent were used. Materials were used in different proportions and several batches were made, and finally desired batch was chosen for the printing.

(iii) Screen printing

Screen printing is a process of thick film deposition on top of a substrate (glass, alumina, etc.). There are several factors that play an important role during the deposition of the material, such as pressure applied, mesh, count of the screen, paste viscosity. There are the following steps used in the screen printing technique.

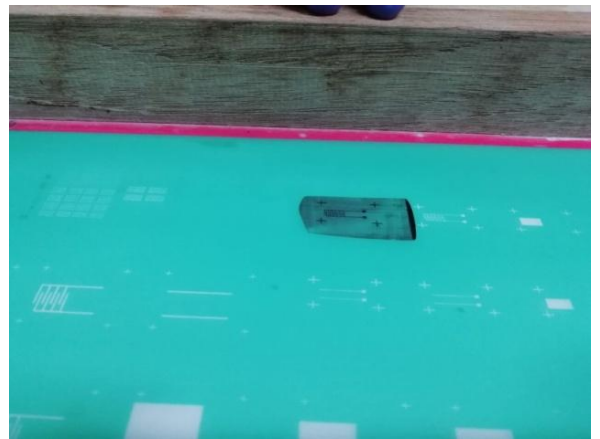
1. Adjustment/Alignment of the screen with the substrate



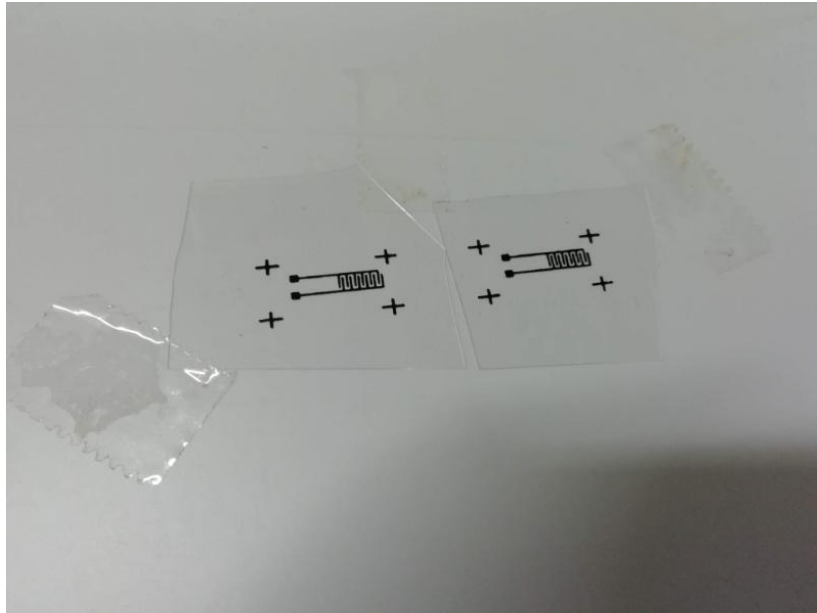
2. Controlling amount and viscosity of the material



3. Controlling pressure to spread out the material



4. Lifting the screen after deposition



There are different types of screens available, depending on the number of mesh openings, viz— 140, 240, 360, 400, per linear inch. The nylon cloth of 140 mesh count was used in the present experimentation work.

Advantages of the screen printing method:

- 1) It is easy to use and low cost.
- 3) Thick films are more robust, less susceptible to contamination.
- 3) Thick film technology offers important advantages, such as high productivity and automation.
- 4) The thick film technology has contributed to the sensor development itself as a primary sensing element. Apart from gas sensors, thick film resistors can be used as a strain gauge, temperature sensors, and magnetic sensors.
- 5) The portability of the screen gives freedom to use this technique almost everywhere without any extra requirements.

Chapter 3

Preparation characterizations and testing of Nano-structured palladium impregnate graphitic carbon nitride composite for efficient hydrogen gas sensing

3.1 Introduction:

This chapter describes the incorporation of nanoparticles of palladium (Pd) into graphitic carbon nitride ($g\text{-C}_3\text{N}_4$) matrix with a view to improve hydrogen sensing efficiency of $g\text{-C}_3\text{N}_4$ by a fairly new chemical process that uses ammonium tetrachloropalladate as a Pd metal nanoparticle source along with an appropriate reducing agent. Researchers have explored $g\text{-C}_3\text{N}_4$ for various applications such as a catalyst for water splitting, photoluminescence, storage because of its relatively low cost, easy synthesis, and ready availability. For the synthesis of $g\text{-C}_3\text{N}_4$, urea was used as a precursor at 550°C and at atmospheric pressure under a muffle furnace without add-on support. The final solution of the Pd/ $g\text{-C}_3\text{N}_4$ nanocomposite was then centrifuged and dried for use as a hydrogen-sensing material. $g\text{-C}_3\text{N}_4$ and Pd/ $g\text{-C}_3\text{N}_4$ were characterized by X-ray diffraction (XRD), scanning electron microscope (SEM), transmission electron microscopy (TEM), UV-VIS-NIR spectroscopy, Raman spectroscopy, Fourier transform infrared spectroscopy (FTIR), and energy-dispersive X-ray spectroscopy (EDS). Pd-dispersed graphitic carbon nitride film was deposited on an interdigitated carbon electrode by using a screen printing technique. From the qualitative analysis by I-V measurement, a significant change in the resistance was observed during the presence and absence of hydrogen gas. The response and recovery time of the sensor were calculated for the sensor at various different concentrations of analyte gases. The sensor response at different deposition techniques such as screen printed, drop a cast, and nebulizer based deposition have been explored and compared. The results show Pd/ $g\text{-C}_3\text{N}_4$ nanocomposite as an efficient hydrogen sensing material.

3.2 Preparation of g-C₃N₄:

g-C₃N₄ was prepared by calcination and urea was used as a precursor to the preparation. Ten grams of urea was placed in a quartz crucible (50 ml) that was covered by aluminum foil. The urea was then heated to 550 °C in a muffle furnace for 3h, with a ramp up and ramp down at a heating rate of 5 °C min⁻¹. The outgrowth of yellowish powder was collected as bulk graphitic carbon nitride (g-C₃N₄). This method meets the requirements of other supplements such as carrier gases (Argon, N, and O), vacuum. The obtained bulk g-C₃N₄ was further converted into fine g-C₃N₄ nanoparticles by ultrasonication-assisted liquid exfoliation, followed by grinding into a fine powder with a mortar and pestle. It was then dispersed in DI water, followed by repeated sonication for six hours. The unexfoliated g-C₃N₄ was removed by centrifugation.

3.3 Preparation of Pd/g-C₃N₄ Composite:

To impregnate the g-C₃N₄ matrix with the palladium nanoparticle, a fairly new synthesis process was explored, as shown in Fig.7, in which 80 mg of finely powdered g-C₃N₄ was added to 100 ml of pure DI water, followed by 30 min of sonication at room temperature. After sonication, 0.0530 grams of ammonium tetrachloropalladate (II) [(NH₄)₂PdCl₄] was added to the solution that was held a further 30 min of sonication. A solution that contained a reducing agent was separately prepared by mixing 0.9 M NaOH and 0.4 M NaBH₄. This solution helps to reduce Pd ions into Pd metal nanoparticle under constant magnetic stirring at 450 RPM for 24 hrs atmospheric temperature. As a result, a dark-colored solution of the Pd/g-C₃N₄ nanocomposite was obtained, which was then centrifuged and dried for use as a hydrogen-sensing material.

J

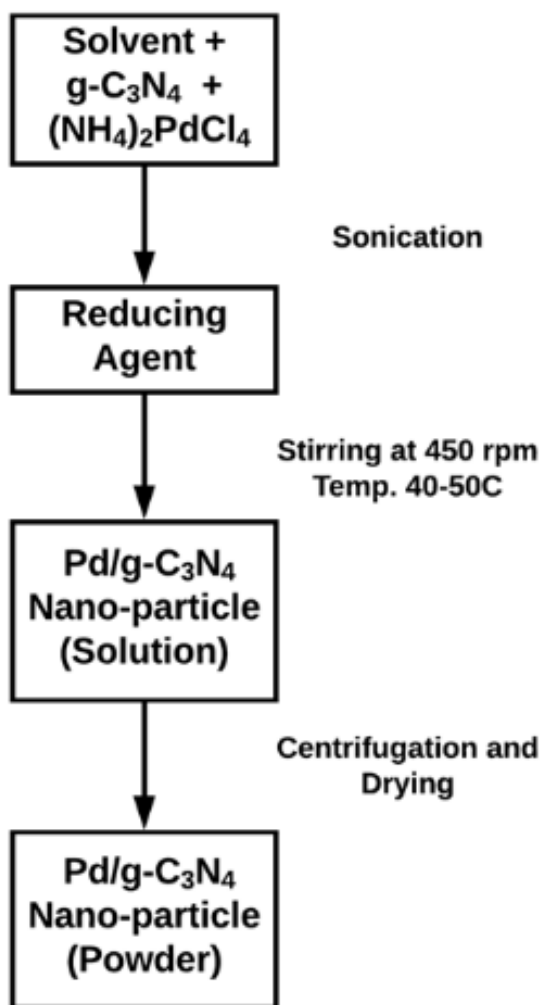


Figure 7: Flowchart of the synthesis process of Pd/g-C₃N₄ nanocomposite.

3.4 Material Characterizations:

Powder X-ray diffraction (XRD) patterns were recorded by using the RigakuSmartLab X-ray diffractometer with Cu K α radiation ($\lambda = 1.5405 \text{ \AA}$). All measurements were taken in the 2θ range of $5\text{--}100^\circ$ with a step size of 0.01° . Vibrational properties of samples were investigated with FT-Raman and FTIR spectrometers. Here, the Bruker, a 3000 Hyperion Microscope with a Vertex 80 FTIR System FTIR spectrometer in the range $500\text{--}4000 \text{ cm}^{-1}$ was used. The samples were prepared by using KBr pelletizer. The Raman spectra were recorded using a Horiba HR 800 Laser Raman Spectrometer in the range of $500\text{--}1800 \text{ cm}^{-1}$. An argon laser (535 nm) was used here. Scanning electron microscope (SEM) images and the energy-dispersive X-ray spectra were

generated by a JSM-7600F (FEG) scanning electron microscope. Philips CM 200 was used to record the transmission electron microscopy (TEM) images. The optical properties were investigated using Thermo Scientific UV-VIS-NIR spectroscopy in the range of 200-800 nm. The chemical compositions (XPS) were recorded using AXIS Supra, Monochromatic (AlK α) 600 W, X-ray source; 1486.6 eV was used.

3.4.1 X-ray diffraction analysis:

The high-resolution X-ray diffraction (HR-XRD) pattern of the graphitic carbon nitride (g-C₃N₄) bulk powder and the nanoparticles are shown in Fig.8. Bulk g-C₃N₄ shows a strong peak at 27.5°, which corresponds to the interlayer diffraction of the conjugated aromatic systems, and the weak peak at 13.01° corresponds to in-planar repeated tri-s-triazine units[87]. The peak intensity of the interlayer diffraction reduces as one moves from bulk to nanoparticles. The interlayer spacing (as calculated from Bragg's law) is 0.323 nm for (002) plane, and it is 0.679 nm for (100) plane.

Further, X-ray diffraction was done on the batch of prepared g-C₃N₄ sample, which is shown in fig.9 (a-c). XRD of three different batches of the g-C₃N₄ sample was carried out. Three different samples were made at different precursor weights, temperatures, and ramping rates. In the case of variation in material weight, no significant change was observed, as shown in fig 9 (a). Similarly, at the different temperatures, it is evident from the XRD that at a lower temperature, the material is more amorphous, and there are several other phases present, which shows that the formation of the material is not proper as shown in the fig.9 (b). In the sample with variation in the ramping rate, it shows that the formation of the material is good when the ramp rate is lower, as shown in fig. 9 (c).

The incorporation of Pd nanoparticles into the g-C₃N₄ matrix gives rise to sharp palladium peaks at 39.64°, 45.73°, 67.12°, 80.95°, and 85.58° as shown in Fig. 8(b), which correspond to (1 1 1), (2 0 0), (2 2 0), (3 1 1), and (2 2 2) FCC crystal planes[88]. The broadening of the peaks and the concurrent decrease in the peak intensity indicate the formation of nanoparticles of Pd. The small

shift in Pd peaks corresponds to the formation of palladium hydride, due to the hydrogen incorporation into the Pd lattice [78].

The crystallite size of the metal particles was calculated using Scherrer's formula:

$$d(\text{\AA}) = k\lambda/(\beta\cos\theta)$$

Where $k = 0.94$ (a coefficient); $\lambda = 1.5405 \text{ \AA}$ (the wavelength of X-ray Cu K α radiation); β = full width at half maximum of corresponding peaks; and θ = peak position. The calculated average crystallite size is around 3–5 nm.

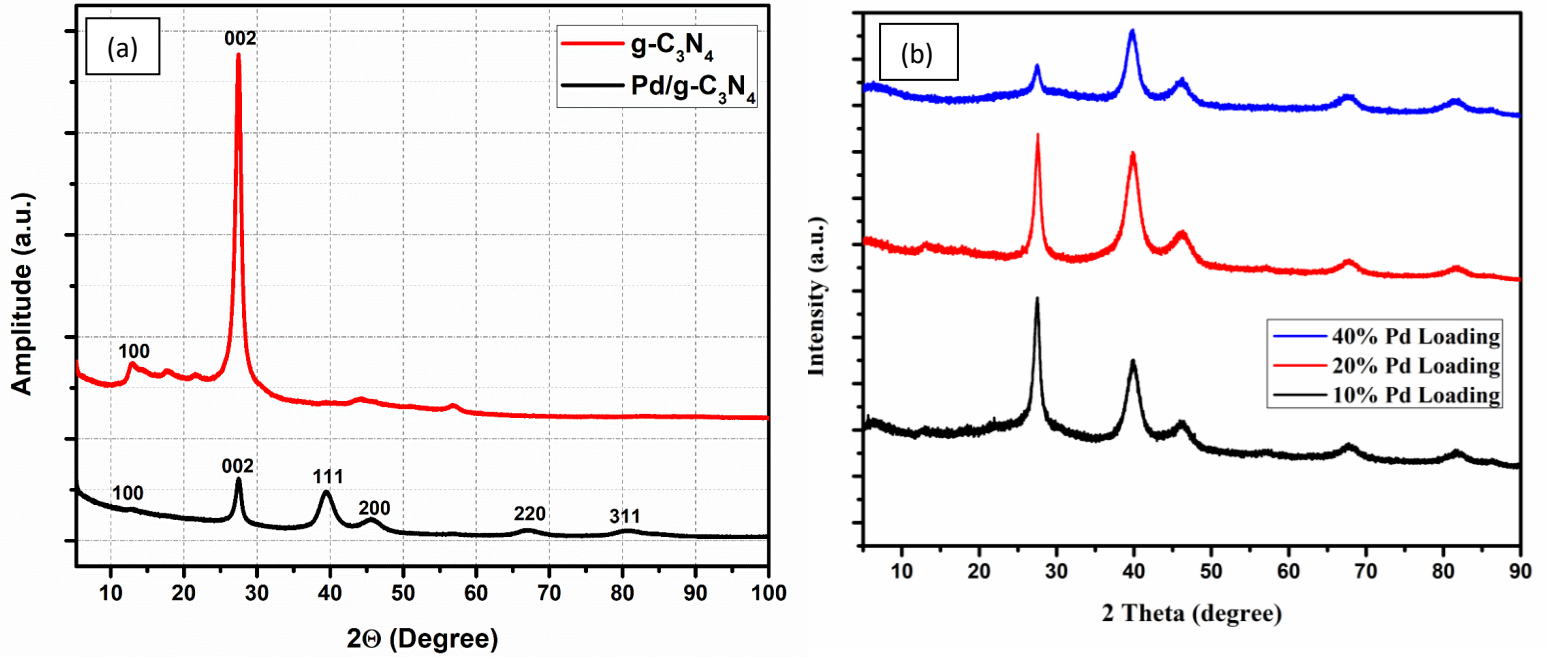


Figure 8: Powder high-resolution X-ray diffraction of Pd/g-C₃N₄ and g-C₃N₄

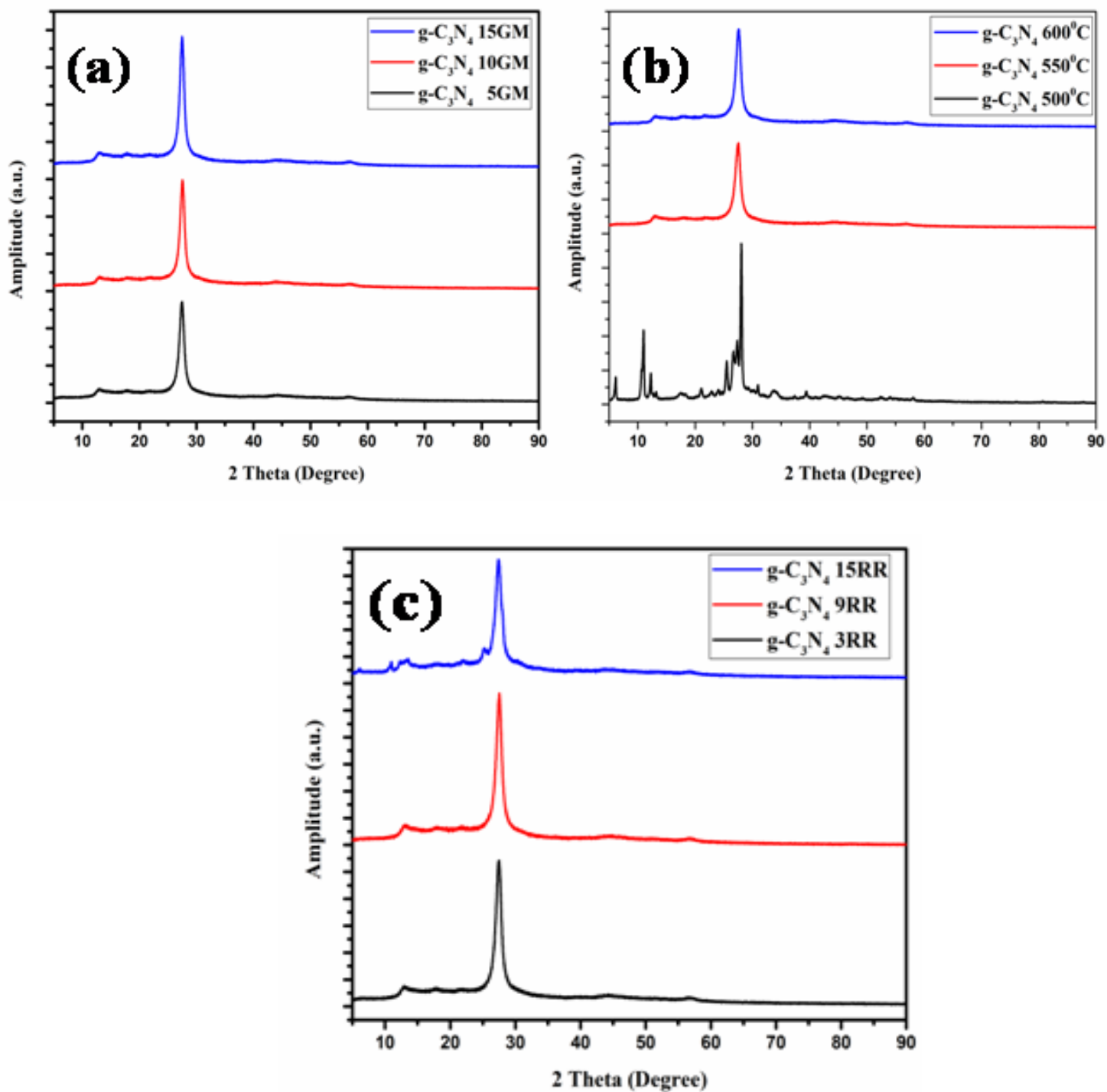


Figure 9: Powder high-resolution X-ray diffraction of and g-C₃N₄ at different temperatures, concentrations, and ramp rate.

3.4.2 Energy-dispersive X-ray spectroscopy:

The energy-dispersive X-ray spectroscopy (EDS) analysis Fig. 10 (a) shows the presence of carbon, nitrogen, and palladium, thereby confirming the incorporation of Pd nanoparticles into the matrix. Similarly, elemental mapping of Pd/g-C₃N₄ nanocomposite was performed, and the presence of elements such as C, N, and Pd on the material is shown in fig 10(b,c,d, e) with different color coding for each element.

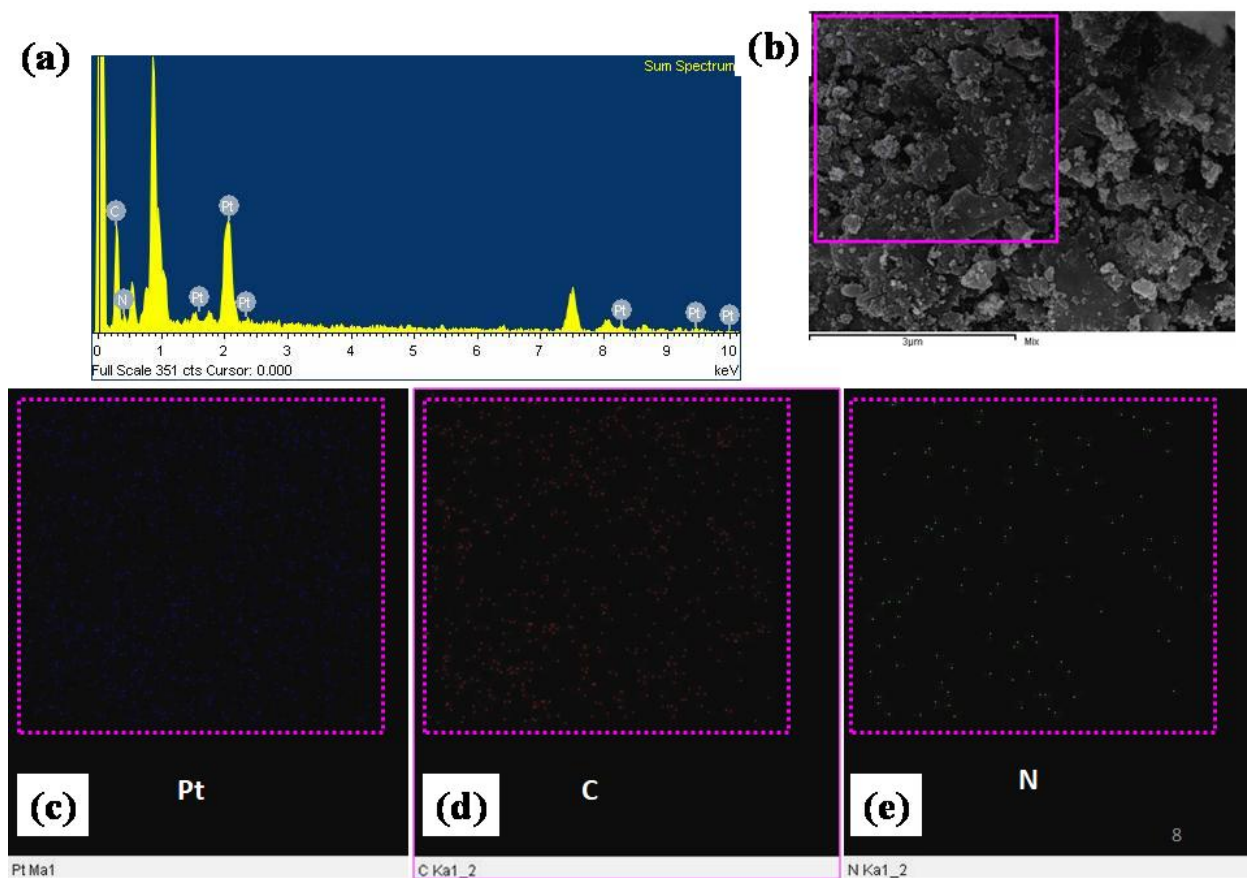


Figure 10: (a) EDX image of Pd/g-C₃N₄ (b-e) elemental mapping of C,N,and Pd..

3.4.3 Thermogravimetric analysis (TGA)

The result of the TGA analysis of the $\text{g-C}_3\text{N}_4$ and the $\text{Pd/g-C}_3\text{N}_4$ nano-composites shown in Fig. 11. From the analysis, it is evident that the $\text{g-C}_3\text{N}_4$ is thermally stable until 600°C , after which it starts decomposing and the decomposition finishes at 700°C . Decomposition is not because of oxidation; instead, it is due to direct thermal decomposition of $\text{g-C}_3\text{N}_4$ to CNH , NH_3 , and C_2N_2 species [89]. Similarly, the $\text{Pd/g-C}_3\text{N}_4$ composite shows good stability until $500\text{--}550^\circ\text{C}$, after which it starts decomposing. The $\text{Pd/g-C}_3\text{N}_4$ nanocomposite starts to decompose at a lower temperature (than $\text{g-C}_3\text{N}_4$), the Pd nanoparticles act as a catalyst [88-89]. The TGA plot for $\text{Pd/g-C}_3\text{N}_4$ nanocomposites suggests that 19.3% (wt%) of material remains beyond 600°C , which corresponds to the loading of Pd metal-nanoparticle in $\text{g-C}_3\text{N}_4$.

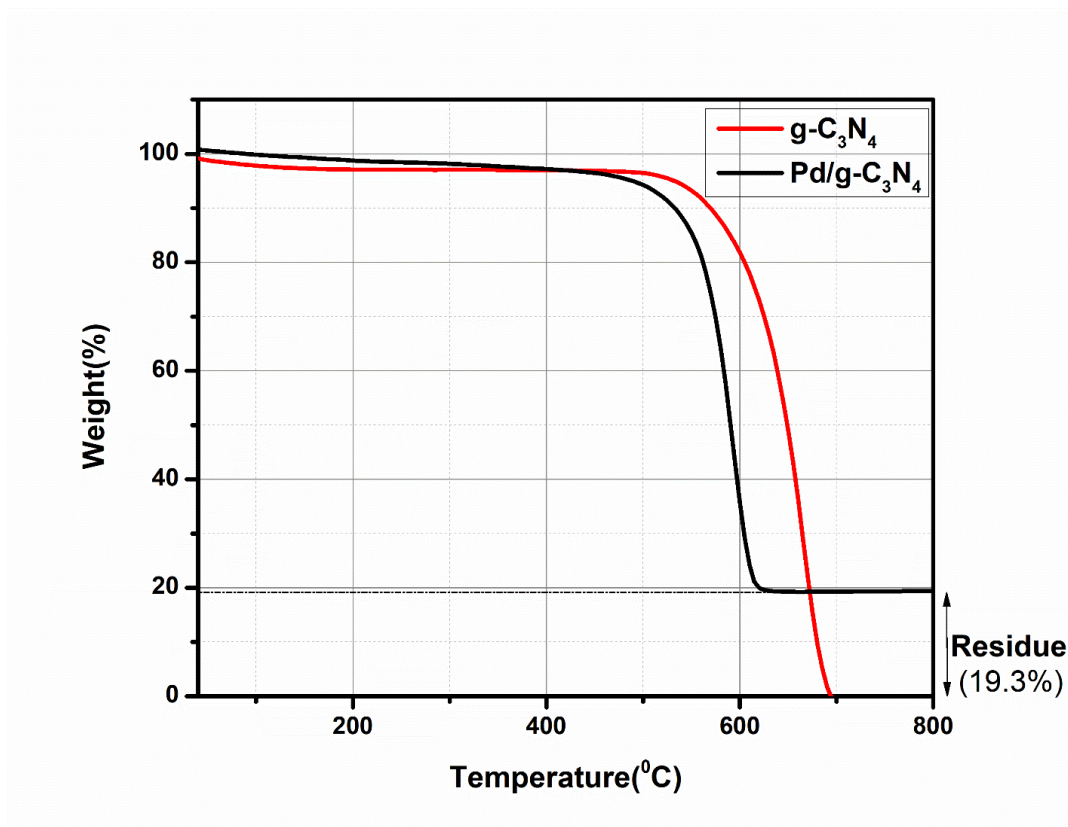


Figure 11: Thermogravimetric (TGA) analysis of $\text{Pd/g-C}_3\text{N}_4$ and $\text{g-C}_3\text{N}_4$.

3.4.4 Morphological Analysis

Morphology of g-C₃N₄ and Pd/ g-C₃N₄ powders were characterized by FESEM and TEM. SEM images (Fig. 12 (a)(b)) reveal irregularity in the layers of g-C₃N₄, which may be attributed to the amorphous nature of the precursor material. Because g-C₃N₄ tended to charge during SEM, a thin (4-5 nm) coating of Pt was deposited (for 60 s at ten mA) that reduced charging and hence, resulted in much-improved imaging. In the case of Pd/ g-C₃N₄, Pd nanoparticles (3–5 nm) formed in the g-C₃N₄ matrix, although, in some places, a Pd cloud was noticed due to uneven loading.

A TEM image of g-C₃N₄ in Fig.12 (c)(d) shows overlapping g-C₃N₄ sheets. The Pd/ g-C₃N₄ TEM image suggests the Pd nanoparticle size to be 3–5 nm that closely matches the particle size that was calculated using Scherrer's formula from the obtained XRD data. The average particle size of the Pd/g-C₃N₄ (Fig. 12(f)) was calculated from the HRTEM image shown in Fig 12(e).

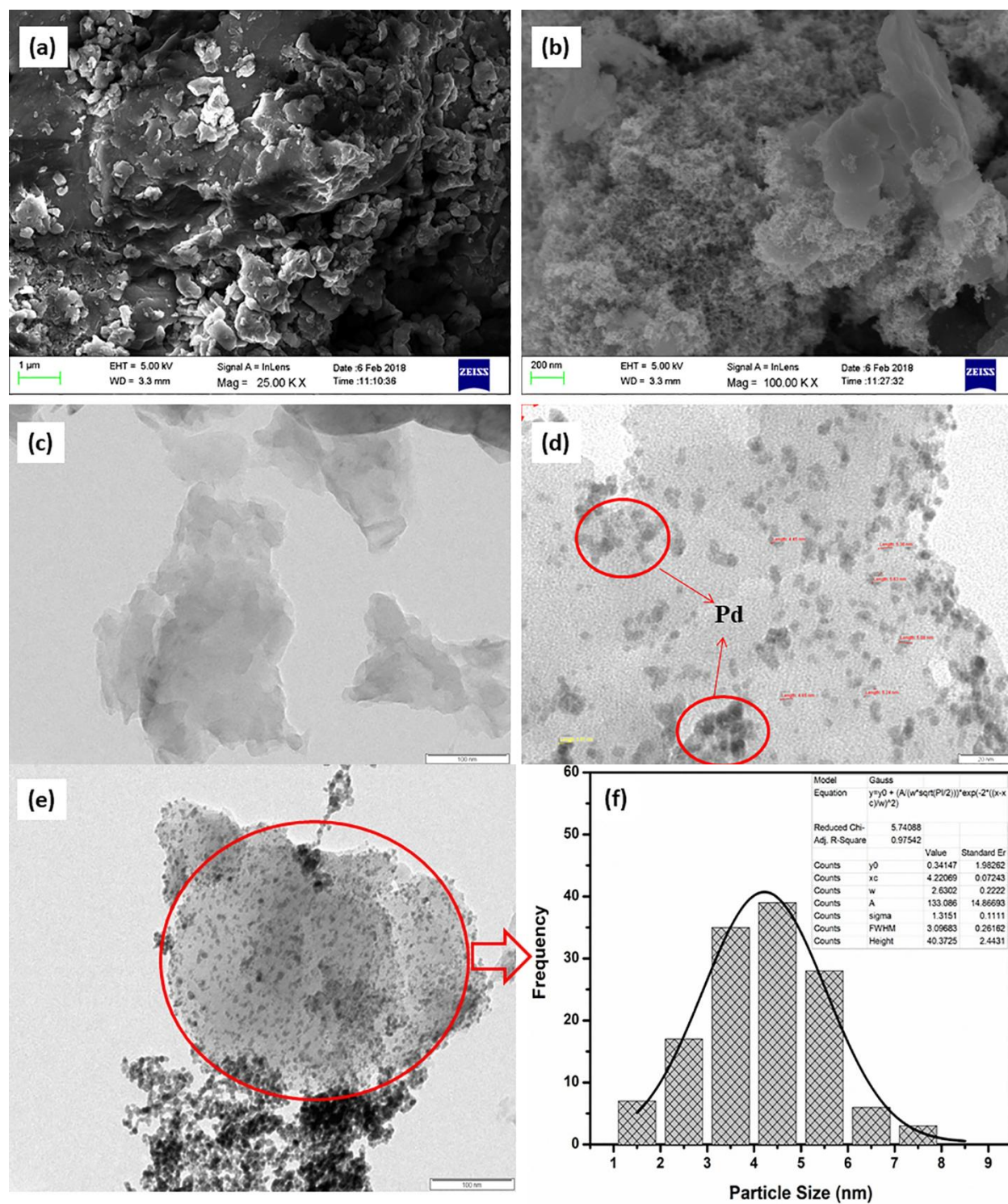


Figure 12: FESEM image of (a) g-C₃N₄ (b) Pd/ g-C₃N₄. TEM image of (c) g-C₃N₄(d) Pd/g-C₃N₄(e) HR-TEM of Pd/g-C₃N₄(f) average particle size of Pd nanoparticles for image (e).

3.4.5 Fourier-transform infrared (FTIR)spectroscopy

FTIR was used to analyze the bonding as well as different vibrational modes, as shown in Fig. 13. For g-C₃N₄, the peaks at 806.55 and 1460 cm⁻¹ correspond to the tri-s-triazine mode [88]. The peaks in the range of 1200 to 1650 cm⁻¹ are due to C-N and C=N stretching vibrations in tri-s-triazine rings. The absorption peak at 1641 cm⁻¹ is due to C=N, and the one at 1318.69 corresponds to C-N [90-92]. The small peak at 2136.97 cm⁻¹ corresponds to cyanogroups [93]. The peaks in the range of 3000–3350 cm⁻¹ are attributed to amino groups, that is –NH₂ or –NH [84]. The stretching modes of NH₂ groups are at 3166 cm⁻¹ [94-95]. For Pd/g-C₃N₄, the FTIR spectrum resembles the spectrum of g-C₃N₄, because the Pd nanoparticle does not form any vibrational bond with the g-C₃N₄ lattice. It was found that the absorption reduces with the incorporation of Pd nanoparticles; the slight absorption was found near 810–880 cm⁻¹, which could be due to aromatic C-H bending. A small blueshift was observed in Pd/g-C₃N₄ FTIR spectra.

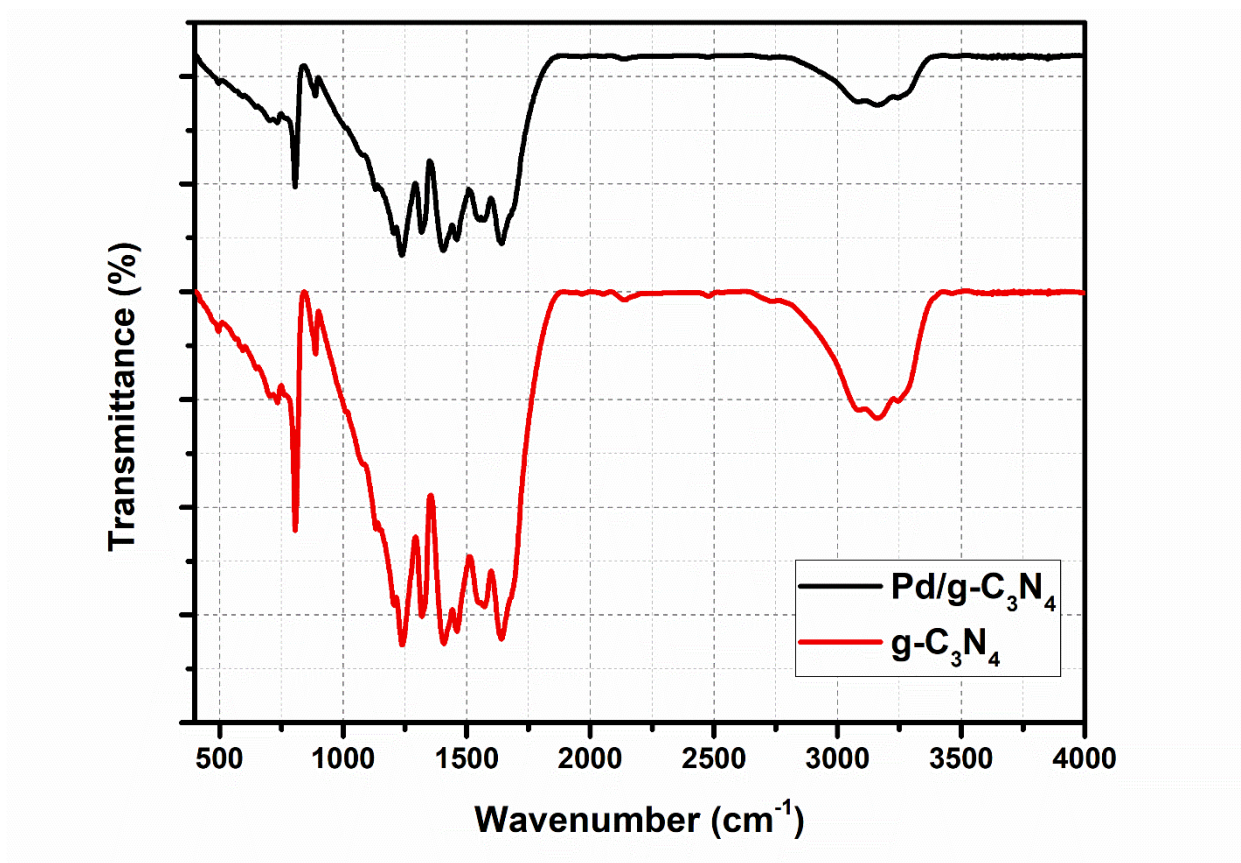


Figure 13: FTIR spectra of g-C₃N₄ and Pd/g-C₃N₄.

3.4.6 Laser Raman Spectroscopy (LRS)

Laser Raman spectroscopy of powder samples of g-C₃N₄ and Pd/g-C₃N₄ provides data similar to those from FTIR analysis, as shown in Fig. 14. Characteristic Raman peaks were observed at 623, 707, 757, 784, 893, 995, 1074, 1228, 1350, and 1573 cm⁻¹ for both the samples, which correspond to the vibration modes of the molecules.

An incident green laser with a spectral width of 535 nm was used as an excitation energy source; mW of power was applied with a sample exposure time of 20 and 120 seconds. In order to obtain a better peak, 20X and 50X objective lens were used. It was observed that the Raman intensity of the peaks at 623 cm⁻¹ and 707 cm⁻¹ is noticeably enhanced in Pd/g-C₃N₄ sample, which can be attributed to the surface-enhanced Raman scattering effect of incorporated Pd nanoparticles.

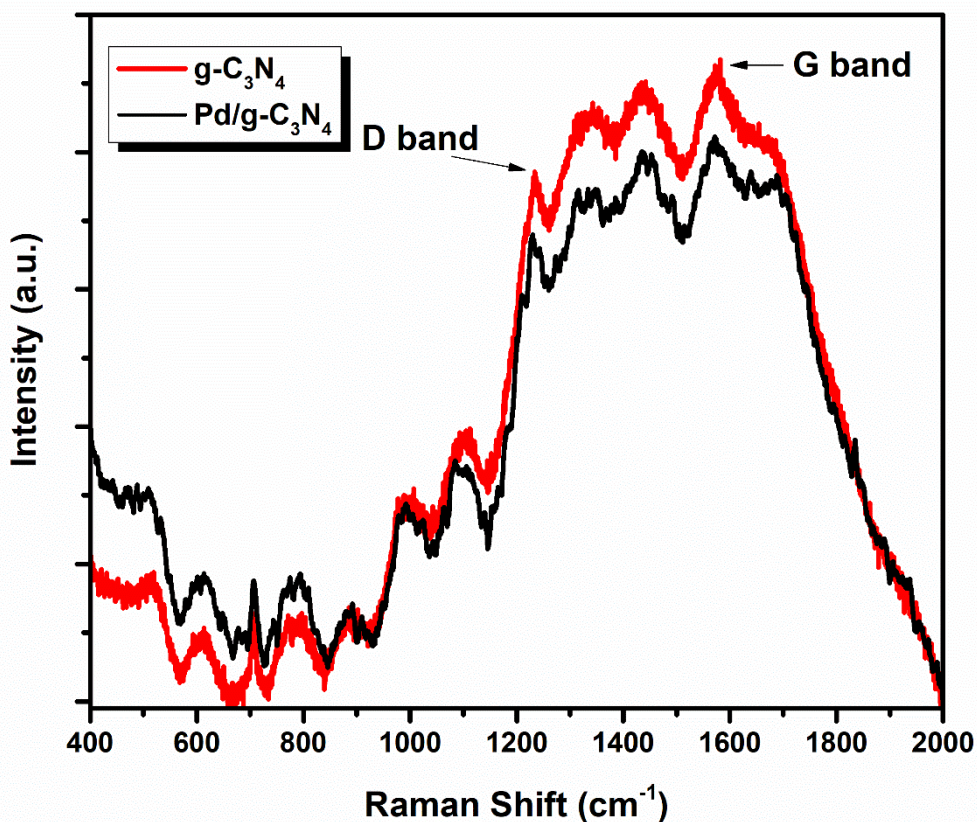


Figure 14: Raman spectra of g-C₃N₄ and Pd/g-C₃N₄

The Raman peaks at 623 cm^{-1} and 707 cm^{-1} correspond to the breathing modes of the triazine ring [96]. A peak of 995 cm^{-1} signifies the in-plane bending vibration of N-C-N [96-97]. Peaks at 1245 cm^{-1} and 1573 cm^{-1} can be assigned to the D and G band, respectively [97]. Peaks around 1436 cm^{-1} and 1573 cm^{-1} indicate the in-plane bending vibration of the NH₂ group. No definite peaks in the $2000\text{--}2500\text{ cm}^{-1}$ region in Raman ruled out the possibility of any triple bond between C and N in the samples [98].

3.4.7 X-ray photoelectron spectrum (XPS) analysis

The X-ray photoelectron survey spectra and core level analysis of Pd/g-C₃N₄ and the g-C₃N₄ film is shown in Fig. 15 (a). From the survey spectra, it is clear that elements such as carbon (C 1s), nitrogen (N 1s), and palladium (3d) are present along with unexpected oxygen (O 1s) peaks. In a deconvoluted high-resolution XPS spectrum, as shown in Fig. 15 (b) peaks at binding energies, 285.2 eV and 285.6 eV correspond to C 1s state for Pd/g-C₃N₄, and g-C₃N₄ attributed to aromatic ring consisting of sp² hybridized C-C bond [88-90]. Peaks at binding energies 288.3 eV and 289.1 eV are due to aromatic ring formation of carbon atom (N=C-N) [88]. C 1s appeared as a doublet whose peaks were separated by 2.8 eV and 3.5 eV for Pd/g-CN and g-CN, respectively.

Similarly, in the deconvoluted high-resolution XPS spectrum, as shown in Fig. 15 (c) peaks at binding energies 398.9 eV and 399.6 eV correspond to N 1s state for Pd/g-C₃N₄ and g-C₃N₄ film respectively, and these peaks are due to the presence of nitrogen in an aromatic ring as C=N-C [78]. The peak at binding energy 401.8 eV is attributed to C-N-H, which reveals the presence of hydrogen in the film could be present during the pyrolysis of the precursor.

Likewise, Fig. 15 (d) gives the deconvoluted high-resolution XPS spectrum of Palladium material along with its oxidation states. Peaks at binding energies 335 eV and 340.3 eV correspond to 3d_{5/2} and 3d_{3/2} respectively, which corresponds to the Pd⁰ oxidation state [89]. Similarly, the Pd⁺² oxidation state was observed. The deconvoluted high-resolution XPS spectrum of 3d state of palladium metal always gives two distinct peaks at 3d_{5/2} and 3d_{3/2}, which correspond to spin-orbital coupling separated by binding energy by 5.3 eV [89].

From the XPS, it was observed that there is a slight shift in the binding energy of g-C₃N₄ and Pd incorporated g-C₃N₄ (Pd/g-C₃N₄), which indicates that impregnation of palladium on g-C₃N₄ matrix causes a good interaction of Pd metal nanoparticles and the g-C₃N₄ matrix. It has been found that the shift in the binding energy is mainly due to the formation of the Pd–C bond [78].

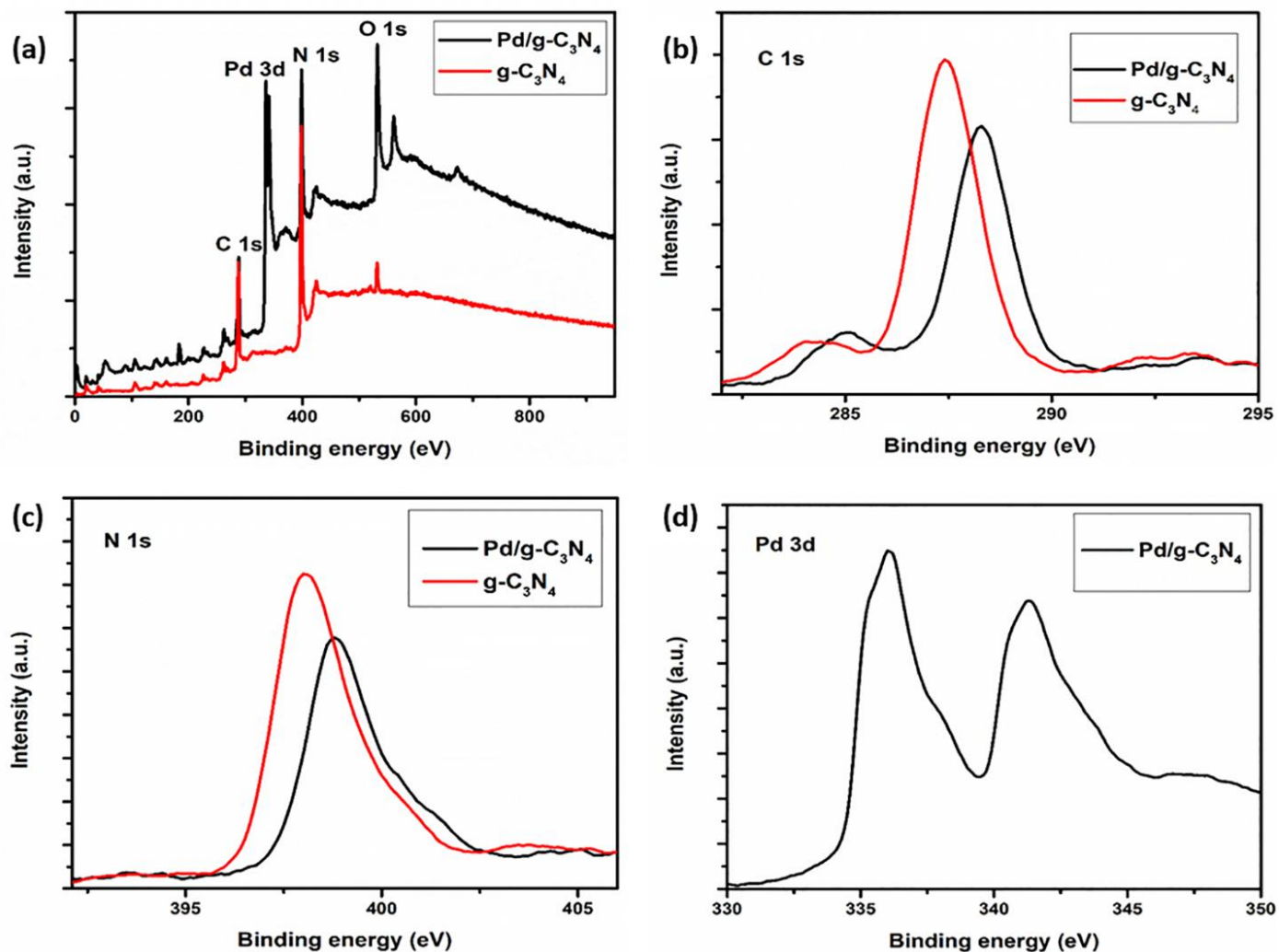


Figure 15: (a) X-ray photoelectron spectroscopy survey spectrum of Pd/g-C₃N₄ and g-C₃N₄, the deconvoluted high-resolution spectrum of (b) C 1s, (c) N 1s and (d) Pd 3d of Pd/g-C₃N₄ and g-C₃N₄.

3.4.8 UV-VIS-NIR Spectroscopy

The optical properties such as transmission, absorption, and reflection, are revealed by UV-VIS-NIR spectroscopy. A strong absorption peak of g-C₃N₄ is observed in the UV region, as shown in Fig.16. The g-C₃N₄ shows a blueshift in the absorption peak as it converts from bulk g-C₃N₄ to nanog-C₃N₄, which increases the bandgap of the material. It was also observed that the redshift occurs in the absorption peak of the g-C₃N₄ sample as the process temperature increases [87-88]. A UV-VIS study was also performed on the doped g-C₃N₄ material and it was found that doping also shifts the absorption peak. Boron doping yielded the least blueshift, while phosphorous yielded a strong redshift toward the visible regime of the spectrum [100]. In the UV-VIS spectra (Fig.16), g-C₃N₄ has an absorption peak till 420 nm, which fades as it moves toward the visible region. However, in the case of Pd/g-C₃N₄, the absorption peak starts from maximum absorption and yields a g-C₃N₄ absorption peak around 300-325 nm. Hence, incorporating the Pd nanoparticles enhances absorption in the UV regime.

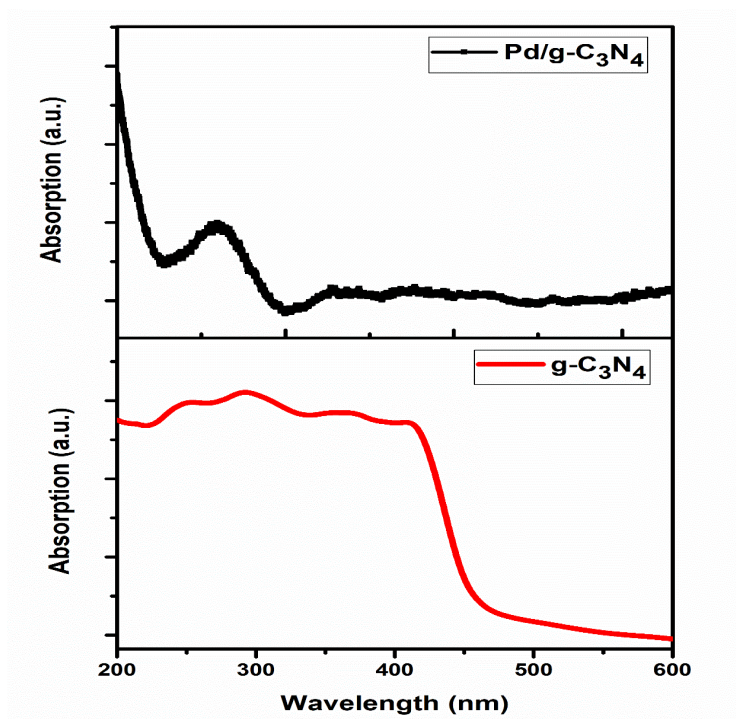


Figure 16: UV-VIS spectra of g-C₃N₄ and Pd/g-C₃N₄.

3.4.9 Photoluminescence spectroscopy:

Photoluminescence (PL) study was performed on the synthesized samples of g-C₃N₄, as shown in fig. 17. Eight different samples were synthesized by using thermal pyrolysis at temperatures ranges from 500-600 °C. The PL study shows a very high-intensity peak, which corresponds to higher recombination of electron-hole pairs at the excitation. Fig 17 shows that a slight shift in the wavelength was observed as the temperature increased from 500 to 600°C.

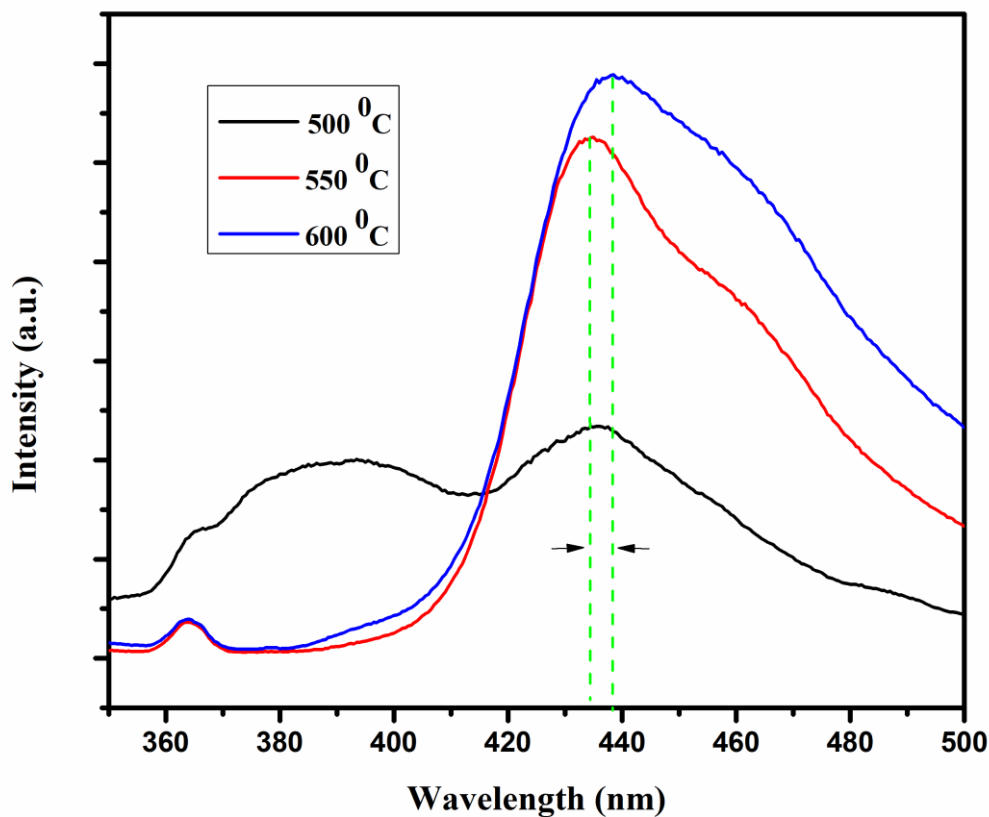


Figure 17: PL spectra of g-C₃N₄ at 500 °C, 550 °C, 600 °C

3.4.10 Cyclic Voltammetry:

Fig.18 shows the cyclic voltammetry (CV) of Pd/g-C₃N₄ and g-C₃N₄ (inset). Strong sorption and desorption peaks are shown by Pd/g-C₃N₄, which correspond to hydrogen evolution. No such peaks were observed for g-C₃N₄. The CV of Pd/g-C₃N₄ has two distinct peaks, 1 and 2, which correspond to Pd(111) and Pd(100). Peaks at the end of the CV correspond to the formation of Pd-O (oxidation of Pd). Similarly, peaks at 0 V (vs. Hg/Hg₂SO₄) correspond to a reduction of Pd-O (reduction of Pd) [99]. Peaks at -0.5V (vs. Hg₂SO₄) and -0.6V (vs. Hg₂SO₄) correspond to underpotential deposition hydrogen desorption and adsorption, respectively. During the process, Pd/g-C₃N₄ shows a prominent hydrogen reaction. The inset of Fig.18 shows g-C₃N₄, which behaves like a double layer capacitor with no hydrogen evolution reaction in the specified potential region. Pd/g-C₃N₄ gives a current density of around 1.5 mA; whereas g-C₃N₄ gives a very small current density of 1.5 μA.

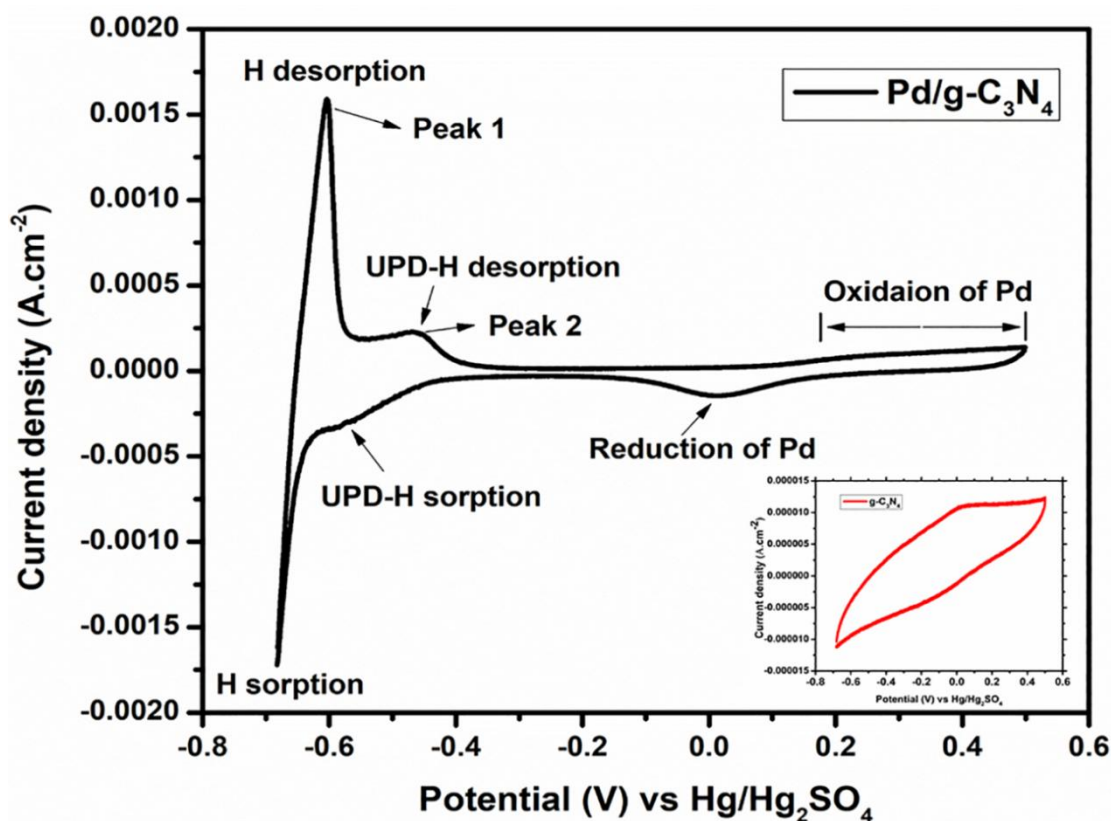


Figure 18: Cyclic voltammetry of Pd/g-C₃N₄ and g-C₃N₄.

3.5 Sensing Mechanism:

The sensing mechanism of the Pd/g-C₃N₄ sensor depends on two phenomena: the hydrogen molecule's interaction with Pd nanoparticles, and the reaction of a hydrogen atom with oxygen at the surface of Pd/g-C₃N₄ [101-102]. In the first case, when a sensor is exposed to a hydrogen-rich environment, the hydrogen molecules react with the Pd nanoparticles, as shown in Fig.19, and convert into hydrogen atoms that react with Pd to form palladium hydride. Interactions of hydrogen with Pd reduce the work function of the hydrogen atom on the surface. Free electrons of the hydrogen atom move toward the g-C₃N₄ matrix and impregnate on the g-C₃N₄ lattice. Pd nanoparticles act as a donor. The charge carrier concentration of the film increases; hence, the conductance increases and the film resistance decreases [103]. A decrease in the sensor resistance upon exposure to hydrogen gas indicates n-type conductivity/sensitivity of the matrix, whereas an increase in the resistance indicates a p-type conductivity/sensitivity.

The second phenomenon occurs due to the interaction of oxygen ions with hydrogen atoms (Fig.19) that are present on the surface of Pd/g-C₃N₄ because of the hydrogen's interaction with Pd particles. The reaction of an oxygen ion with two hydrogen atoms forms a water (H₂O) molecule at the surface and releases two electrons. Hence, the charge carrier concentration increases, and the resistance of the surface decreases [103-104]. As hydrogen molecules desorb from the surface, the resistance of the sensor increases. The resistivity of the sensor depends upon the concentration of hydrogen molecules.

It was also reported that when a hydrogen atom reacts with Pd nanoparticles, it forms PdH_x, causing swelling of the surface area. This phenomenon can be utilized in the optical sensing of hydrogen gases.

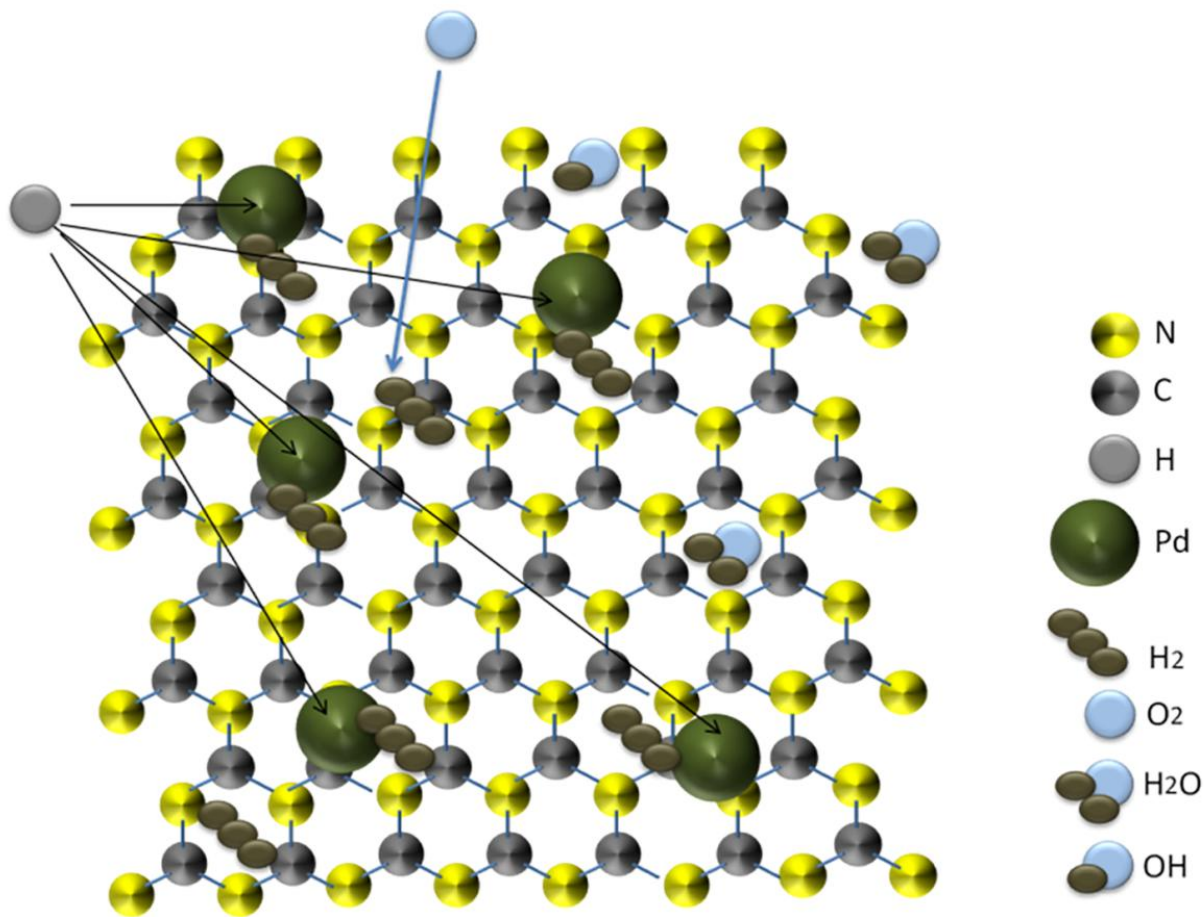


Figure 19: Sensing mechanism of Pd/g-C₃N₄ based resistive hydrogen gas sensor.

3.6 Fabrication of Screen-printed Sensor:

Pd/g-C₃N₄ nanocomposite-based hydrogen gas sensors were fabricated by the screen-printing technique. The inter-digitated electrodes (IDE) were designed by using CorelDRAW. IDE and the sensor probe are illustrated in Fig. 20 (a). Carbon-based electrode patterns were developed on a substrate by screenprinting, using a custom-made stencil. The IDE patterns were printed on a glass substrate and cured at 120 °C for 15 min. For improving printing results and precision, a 135- μ m mesh count screen was used and the paste was evenly spread over the entire printed area, using a 2-inch-sized squeegee. As illustrated in Fig. 20 (b), the overall sensor is made up of three

parts: sensing probe/material (Pd/g-C₃N₄ nanocomposite), carbon inter-digited electrodes, and a glass substrate. The image of the screen-printed sensor with and without the sensing probes are shown in Fig. 20 (b). Sensing material was prepared by taking 20mg of Pd/g-C₃N₄ nanocomposite added in terpineol (solvent) without any binder, screen printed on IDE, as shown in the Fig. 20 (c), followed by annealing for 30minute. The contacts to the electrodes were made using silver epoxy followed by drying at 90 °C for 1hr.

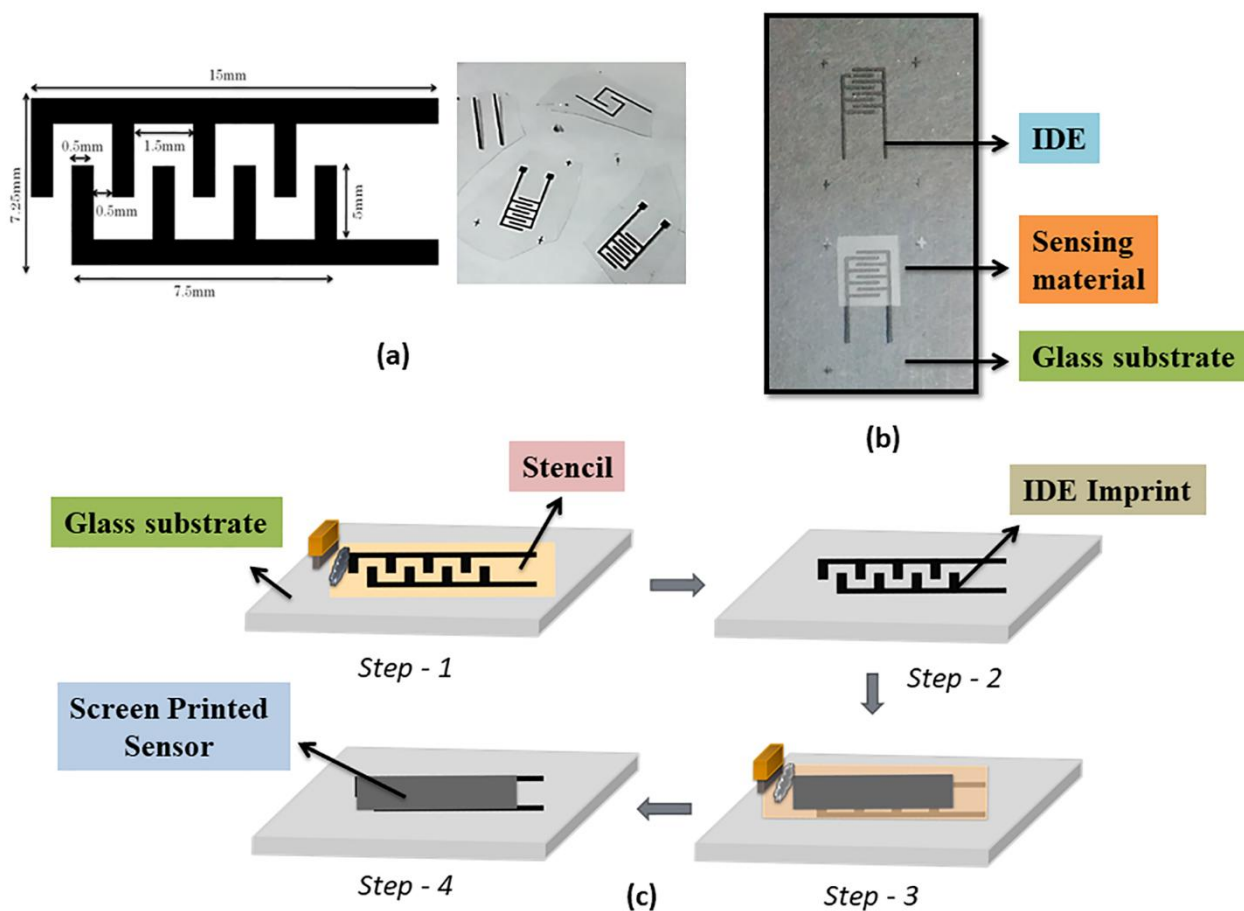


Figure 20: (a) Carbon inter-digited electrode (b) Screen printed Pd/ g-C₃N₄ sensor (c) Screen printing process.

3.7 Gas sensing measurement and analysis:

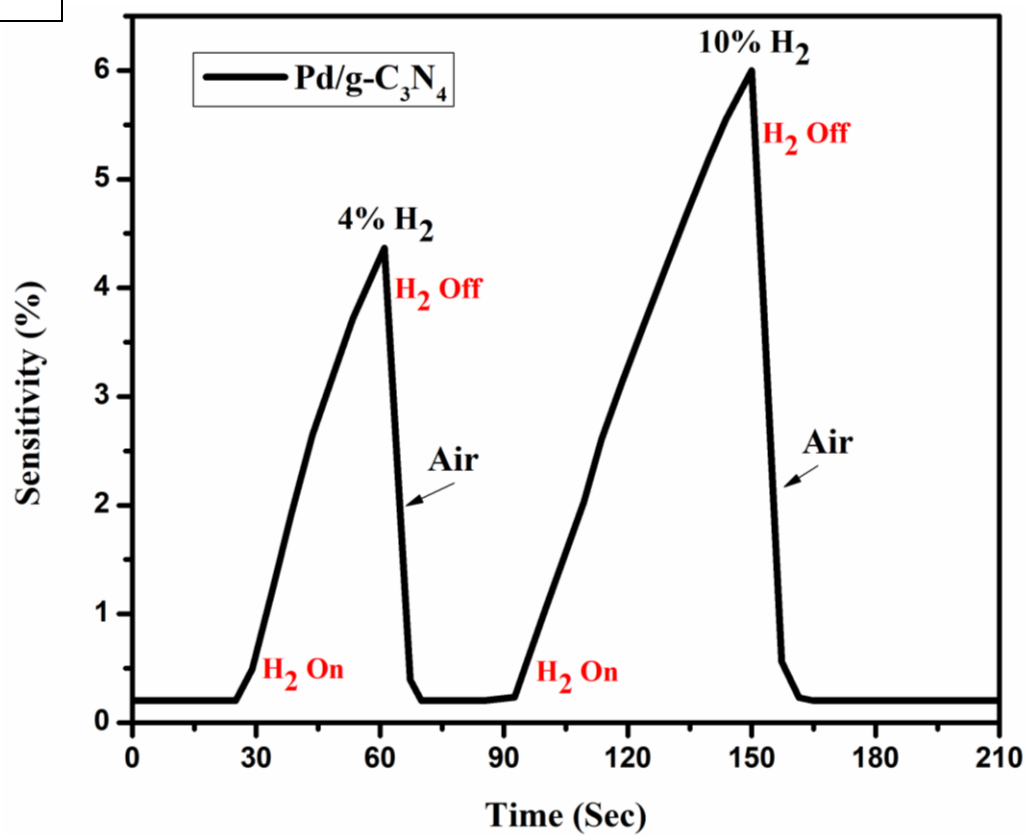
The sensing response of the fabricated film was recorded by depositing the film on an interdigitated carbon electrode, followed by silver paste for the electrical connection to the digital multimeter. The sensor change in the resistance was recorded during the presence and absence of hydrogen gas inside the testing chamber. During the testing of the sensor under the influence of hydrogen gas, it was observed that the resistance of the sensor increases as hydrogen is introduced into the test cell. The overall change in the resistance was converted to the sensor sensitivity (% S) which can be given as,

$$\% S = \frac{R_{tg} - R_{cg}}{R_{cg}} \times 100$$

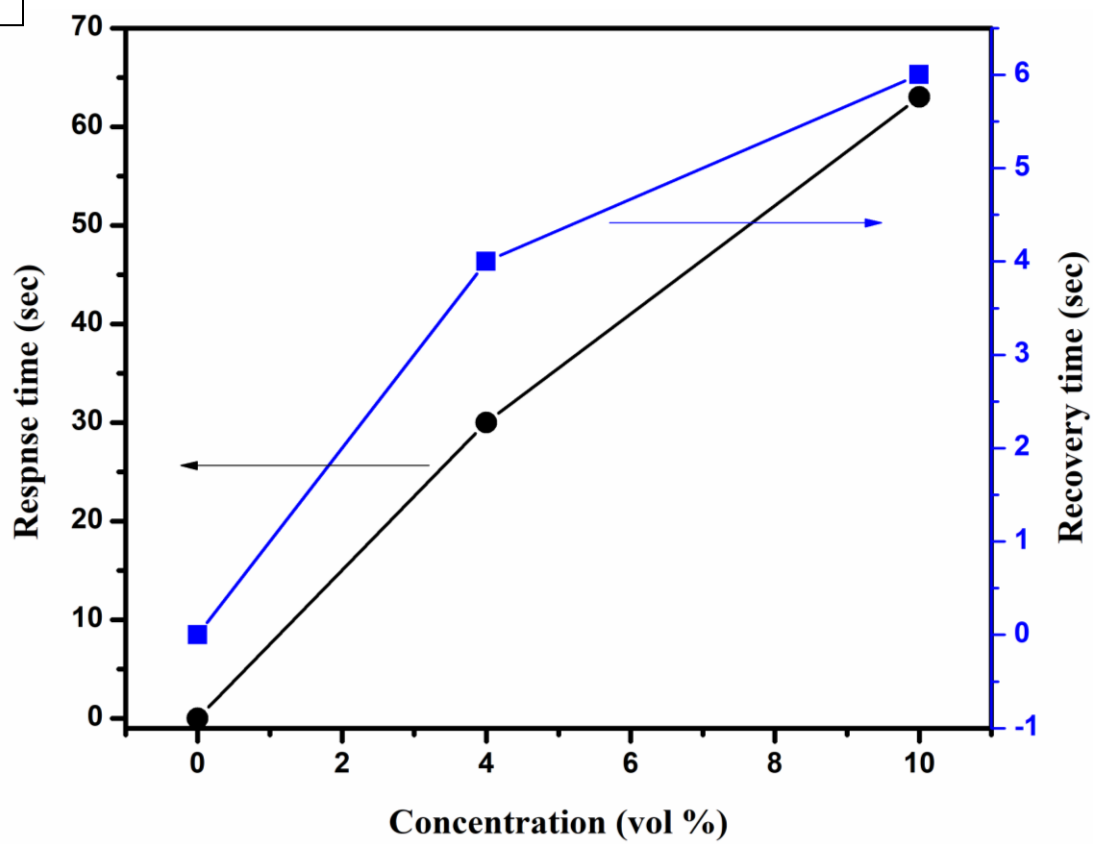
Where R_{cg} represent the resistance of the sensor when no hydrogen is present. Similarly R_{tg} refers to the resistance of the sensor in the presence of the analyte gas.

As shown in Fig 21(a), the sensitivity for the 10% hydrogen gas was measured to be 6%. Similar to that for 4% hydrogen concentration, the sensitivity was recorded as 4.6%. All the readings were taken at room temperature. The response time for 10% and 4% concentration was recorded as ~6sec and ~2-3 sec, respectively, as shown in Fig. 21 (b). The recovery time was recorded almost the same for both the sensors, which was around 3-4 sec in the open-air atmosphere. These results indicate that the sensor has good reversibility hence shows improved reproducibility over the different concentrations of the analyte gas. The Pd/g-C₃N₄ sensor shows fast switching capabilities and better sensitivity; however, g-C₃N₄ does not show any changes in its resistivity over hydrogen exposure. The improved sensing performances of the Pd/g-C₃N₄ nebulized film can be understood by the sensing mechanism that occurs during the sensing process. According to the sensing mechanism, it is assumed that when Pd adsorbed hydrogen molecules, Pd converts to PdH_x and the hydrogen molecules to hydrogen H⁺ and H⁻ ions. As a result of diffusion of atoms to the Pd surface, the overall work function reduces. Hence, the transfer of the electrons from the Pd atom to the g-C₃N₄ matrix occurs, and electrons get adsorbed into the interstitial sites of the material. Pd acts as a donor by donating electrons to the support material. The overall phenomenon generates electron-hole recombination in g-C₃N₄ support. As a result of recombination, the resistance of the sensor increases, hence the conductivity decreases.

(a)



(b)



(c)

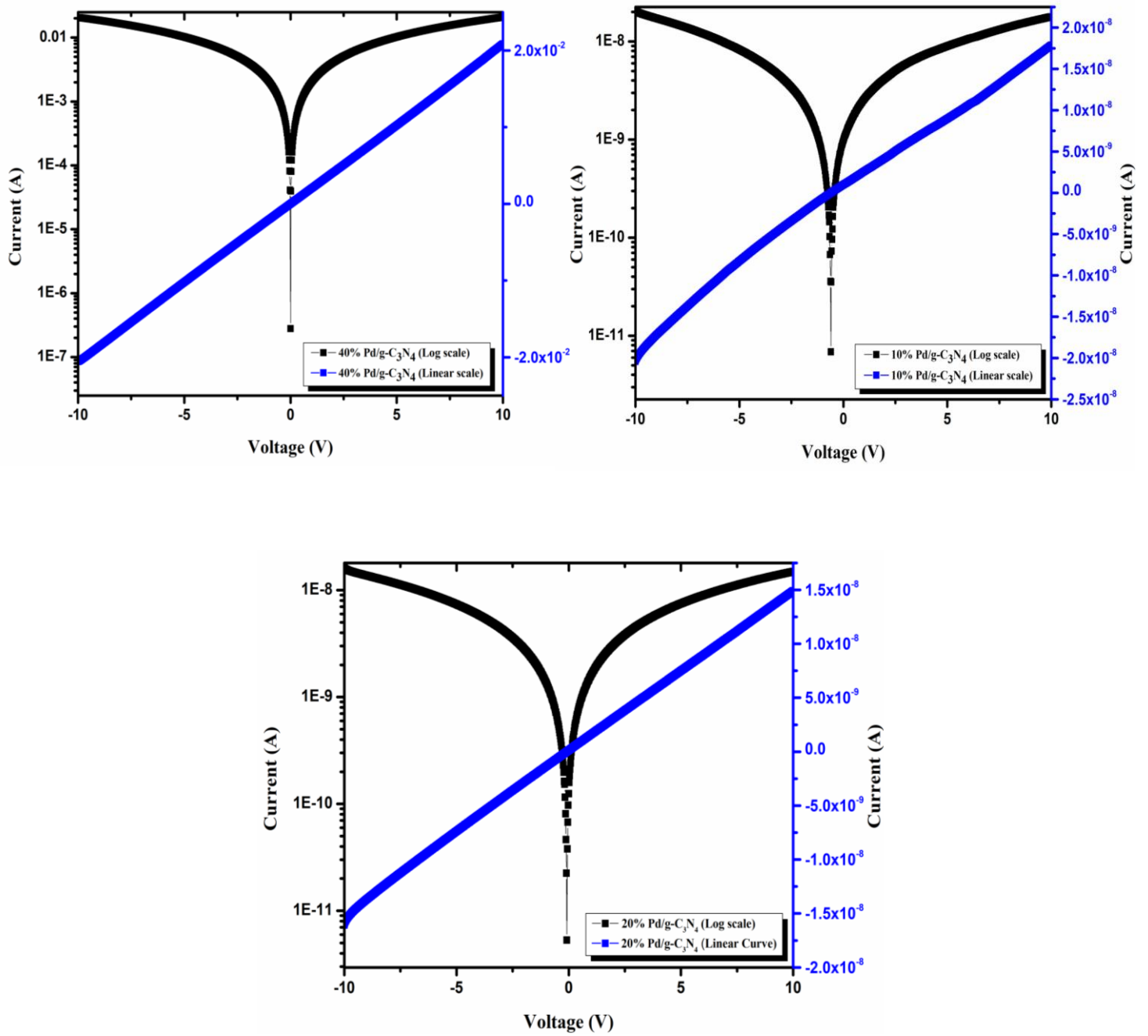


Figure 21: (a) Sensor sensitivity over different hydrogen gas concentration, (b) Response and recovery time of the sensor at different hydrogen gas concentration.(c) I-V curve of Pd with different loading.

Chapter 4

Preparation Characterizations and testing of Pt/g-C₃N₄ composite for efficient hydrogen gas sensing

4.1 Introduction:

In this chapter, the hydrogen sensing properties of the Pt impregnated graphitic carbon nitride nanocomposite at room temperature have been described. The sensing material was synthesized by using a hydrothermal approach, where melamine and chloroplatinic acid hexahydrate were used as precursors. The sensor was fabricated by depositing sensing materials on a screen-printed carbon electrode by jet nebulizer based spray pyrolysis setup. The crystallinity, nano morphology, elemental analysis, and chemical composition of the samples were examined by XRD, SEM, HRTEM, EDS, and XPS. A drastic change in electrical resistance was recorded during the presence and the absence of the analyte gas. The sensitivity obtained for the sensors at different concentrations were recorded. The sensing results depict that the Pt/g-C₃N₄ shows a good response towards the hydrogen gas and could be used for reliable hydrogen gas sensing.

4.2 The synthesis process of Pt/g-C₃N₄:

The g-C₃N₄ matrix was prepared by thermal calcination, and melamine was used as a precursor for the preparation. Five grams of melamine were placed in a quartz crucible (50 ml), which was covered by aluminum foil. The precursor material was then heated to 550 °C in a muffle furnace for 3h. The outgrowth of yellowish powder was collected, and the bulk was later characterized to be graphitic carbon nitride (g-C₃N₄). This method does not employ carrier gases (Argon, N, and O) and vacuum. The obtained bulk g-C₃N₄ was further converted into fine g-C₃N₄ nanoparticles by ultrasonication-assisted liquid exfoliation, followed by grinding into a fine powder with a mortar and pestle. It was then dispersed in DI water, which was followed by repeated sonication

for six hours. Unexfoliated g-C₃N₄ was removed by centrifugation. To impregnate the g-C₃N₄ matrix with the platinum nanoparticle, finely powdered g-C₃N₄ was added to pure DI water, followed by sonication at room temperature. After sonication, chloroplatinic acid hexahydrate (H₂PtCl₆·6H₂O) was added to the solution, followed by continuous sonication. A solution that contained a reducing agent was separately prepared by mixing NaOH and NaBH₄. This solution helps to reduce Pt ions into Pt metal nanoparticles under constant magnetic stirring at atmospheric temperature. As a result, a dark-colored solution of the Pt/g-C₃N₄ nanocomposite was obtained, which was then centrifuged and dried for use as a precursor material.

4.3 Material Characterizations:

4.3.1 X-ray Diffraction (XRD)

The XRD analysis was performed to explore the phase composition of the Pt/g-C₃N₄ nanocomposite, as shown in fig 22 and fig 23. g-C₃N₄ shows two peaks at $2\theta = 13.5^\circ$ and 27.5° , respectively, which corresponds to the 100 and 002 crystal plane [105,106]. The inter-planar spacing for both the peaks was calculated as 0.685nm and 0.323nm, respectively. The peak at 27.5° corresponds to the inter-planar stacking of aromatic rings; similarly, 13.5° peak refers to the graphite-like layer structure [106].

Pt shows peaks at $2\theta = 40.1, 46.6, 68.01, 81.80,$ and 86.51 which correspond to (1 1 1), (2 0 0), (2 2 0), (3 1 1), (2 2 2) planes, respectively [105]. The sharp peak of Pt shows the formation of highly crystalline nanoparticles on the g-C₃N₄ sheets. The average particle size of the impregnated Pt nanoparticle was calculated by using Scherrer's equation which can be written as:

$$D = \frac{K\lambda}{\beta \cos\theta}$$

Where,

D = Crystallite Size (nm)

K = 0.9 (Scherrer constant)

β = Full-width half maxima (Radians)

θ = Peak position (Radians)

The average particle size was calculated to be around 5-7 nm, which is in agreement with the TEM result. The XRD analysis shows peaks that correspond to g- C_3N_4 and Pt only; hence, we can conclude that material does not have any impurities.

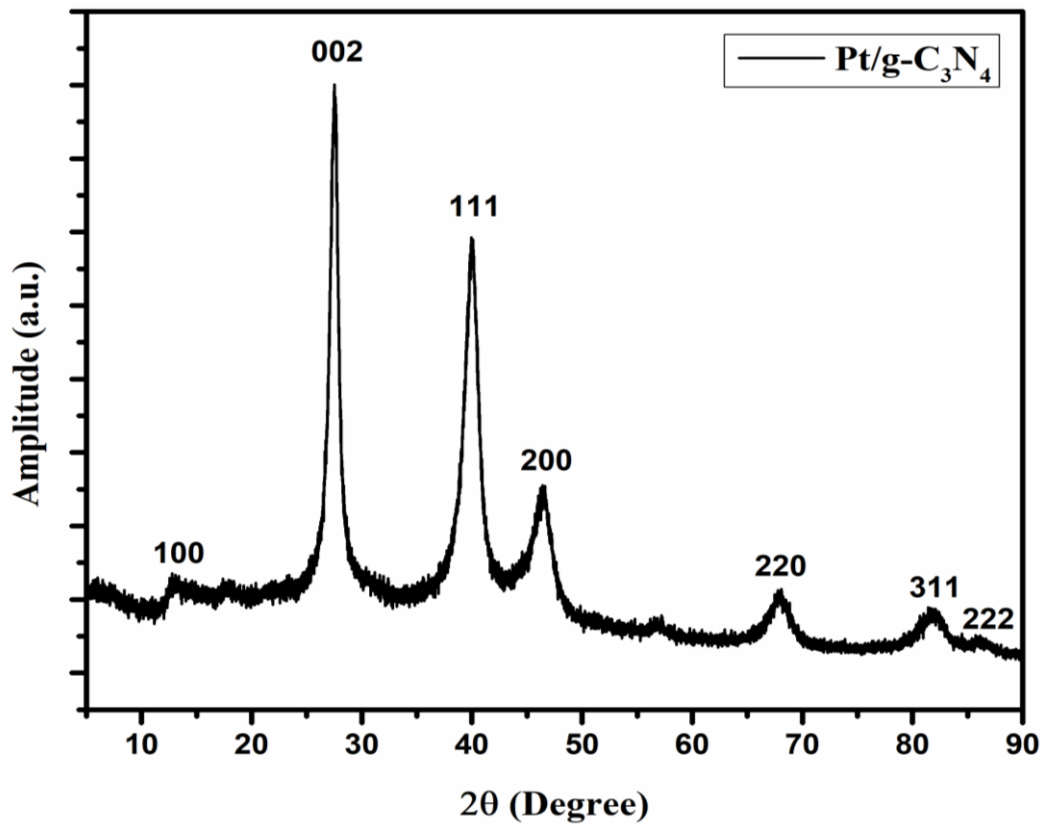


Figure 22: XRD spectrum of Pt/g- C_3N_4 .

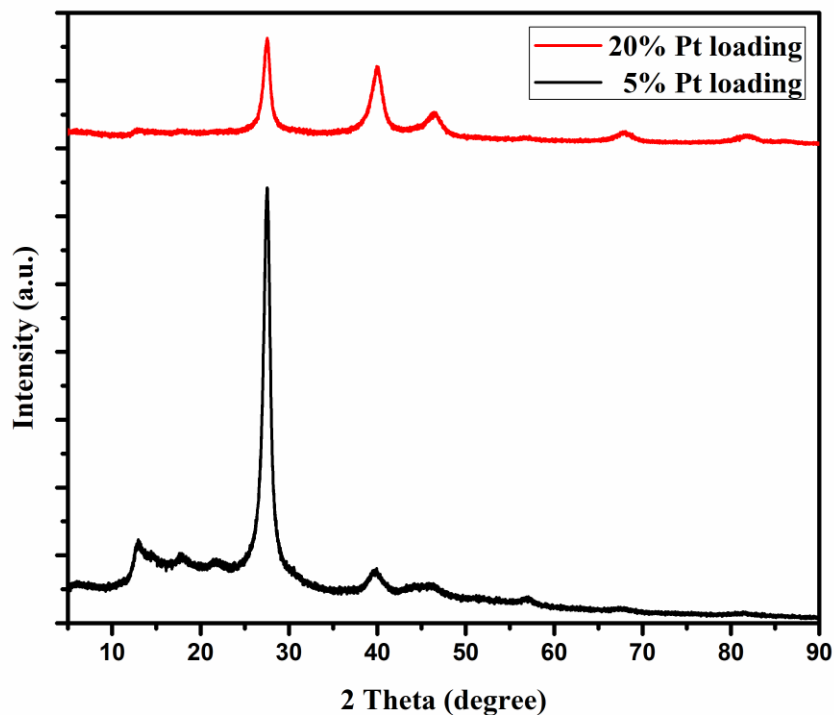


Figure 23: XRD spectra of Pt/g-C₃N₄ with Pt loadings of 5% and 20%.

4.3.2 X-Ray Photoelectron Spectroscopy (XPS):

To determine the chemical status and composition of the elements present in the Pt/g-C₃N₄ nanocomposite, X-ray photoelectron spectroscopy (XPS) was performed. The XPS survey spectrum for the Pt/g-C₃N₄ nanocomposite is shown in Fig. 24, which indicates the presence of Pt 4f, C 1s, and N 1s in the material. Two distinct peaks at 72.8 eV and 74.45 eV are assigned to Pt 4f_{7/2} and Pt 4f_{5/2}. These peaks are the same as the binding energy of Pt⁰ [105,107]. The spin-orbit splitting or energy differences between two peaks are around 2 eV. C 1s shows three peaks at 282.6, 284.8, and 288.5 eV. These correspond to -NH₂ group and sp² bonded carbon (N-C=N) in the aromatic structure [107-109]. N 1s can be deconvoluted into two peaks 396.3 and 398.7 eV. The peak at 398.5 is attributed to sp² hybridized nitrogen (C-N=C) and tertiary nitrogen (N-C) [107-109]. The binding energy of Pt 4f is observed to be slightly shifted as compared to that of the pure Pt. This confirms strong interaction between the two materials and also concludes

that Pt/g-C₃N₄ was successfully synthesized. All the required elements are present in the composites, and the phase of the as-prepared Pt/g-C₃N₄ is stable.

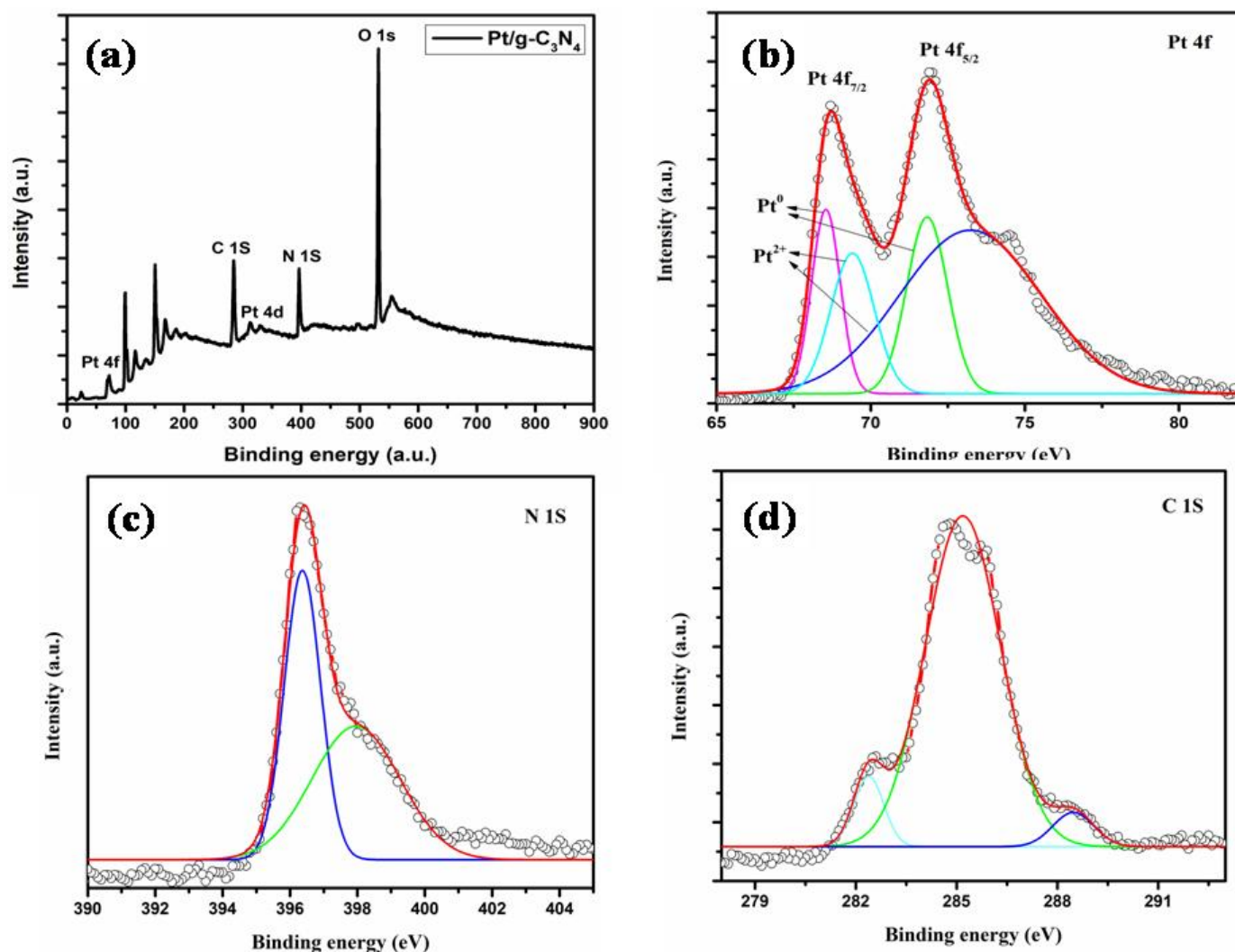


Figure 24: XPS spectra of (a) full scan spectra of Pt/g-C₃N₄ (b) Pt 4f (c) N 1s (d) C 1s

4.3.3 Field Emission Scanning Electron Microscopy (FESEM) and Transmission Electron Microscopy (TEM):

FESEM analysis of the as-prepared Pt/g-C₃N₄ is shown in Fig. 25(a). Pd nanoparticles are well impregnated on g-C₃N₄ support. The presence of the two materials can be easily identified on the basis of color contrast. Pt cluster was seen in some places, which may be due to the conglomeration of the material.

The TEM image in Fig 25(b) clearly shows that the Pt is present on the support of g-C₃N₄. The Pt cloud was formed in some places, as depicted in the SEM image. The particle size calculated by TEM is around 3-5nm, as shown in Fig 25(c), which is in good agreement with the Sherrer's average particle size calculation done from the obtained XRD data. The presence of Pt nanoparticle in g-C₃N₄ is further confirmed by the interplanar spacing between the planes, as shown in Fig 25(d). The line spacing of 0.22 nm is clearly visible from the figure, which attributes to Pt (111) plane [105].

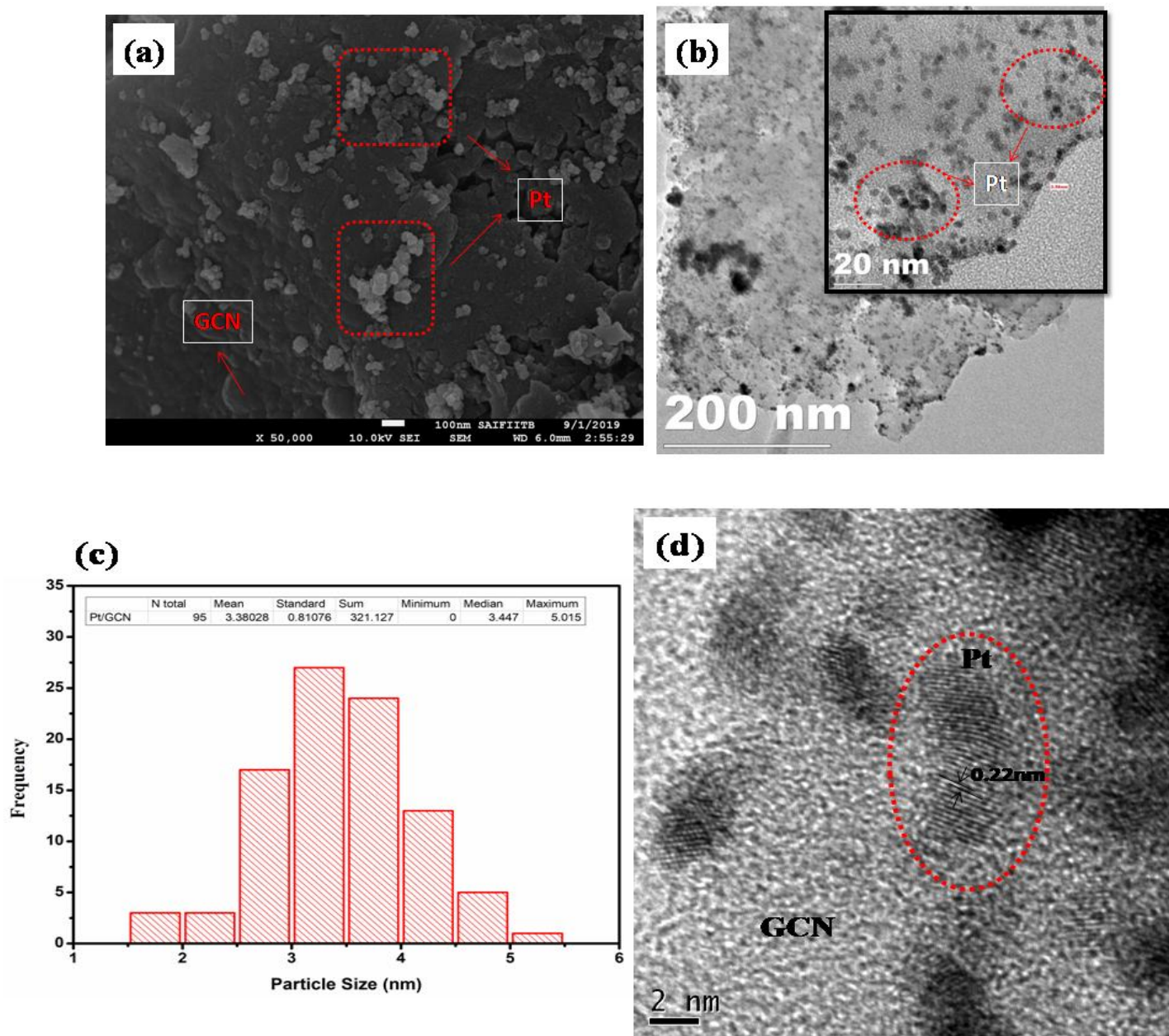


Figure 25: (a) FESEM analysis of Pt/g-C₃N₄ (b) TEM of Pt/g-C₃N₄ (c) Particle size of Pt from TEM data (d) Inter-planar spacing of Pt/g-C₃N₄.

4.3.4 Energy Dispersive X-Ray Spectroscopy (EDX):

EDX analysis was performed to evaluate the elemental percentage in the composite, as shown in Fig 26 (a). The presence of C, N, Pt is clearly evident from the EDX spectra of the selected area, as shown in Fig 26(c),(d)&(e). Similarly, elemental area mapping of Pt, C, and N is displayed. The presence of all the elements can be seen from the different color coding for the elements. In the EDX spectra, apart from the desired peaks, some extra peaks are also present, which are attributed to the coating material and filament.

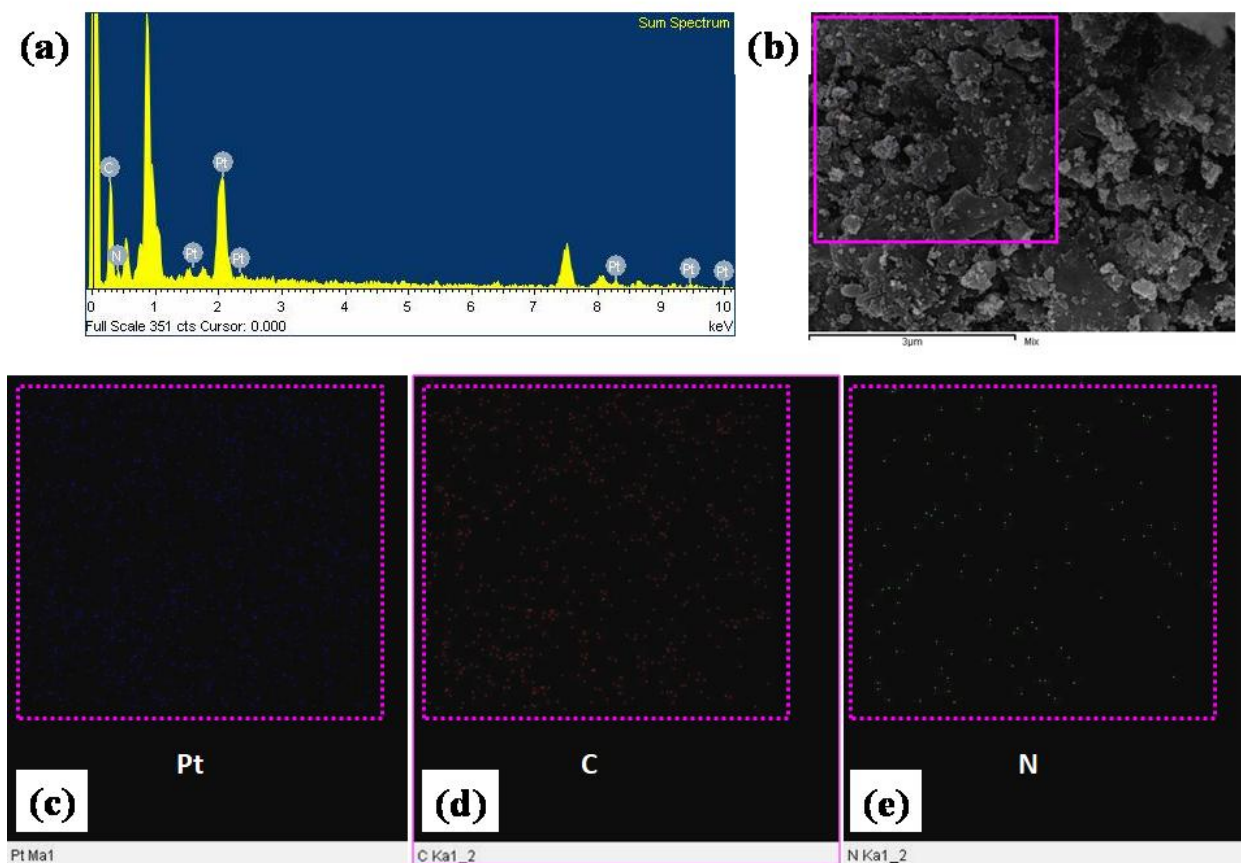


Figure 26: (a) EDX of Pt/g-C₃N₄ (b) elemental area mapping of elements (c) Pt (d) C (e) N.

4.3.5 Fourier Transform Infrared Spectroscopy (FT-IR):

FTIR spectrum for Pt/g-C₃N₄ is shown in Fig 27. The peak at 810 cm⁻¹ is due to the triazine unit present in the g-C₃N₄ material [110]. Peaks at 1245 cm⁻¹, 1335cm⁻¹, 1410 cm⁻¹, and 1638cm⁻¹ are attributed to the aromatic C-N or C=N stretching vibration mode [111-113]. The peak at higher binding energy around 3500-3750 cm⁻¹ refers to the single bond to hydrogen (O-H, C-H, N-H) or the hydroxyl group on the surface of the Pt/g-C₃N₄ nanocomposite [114].

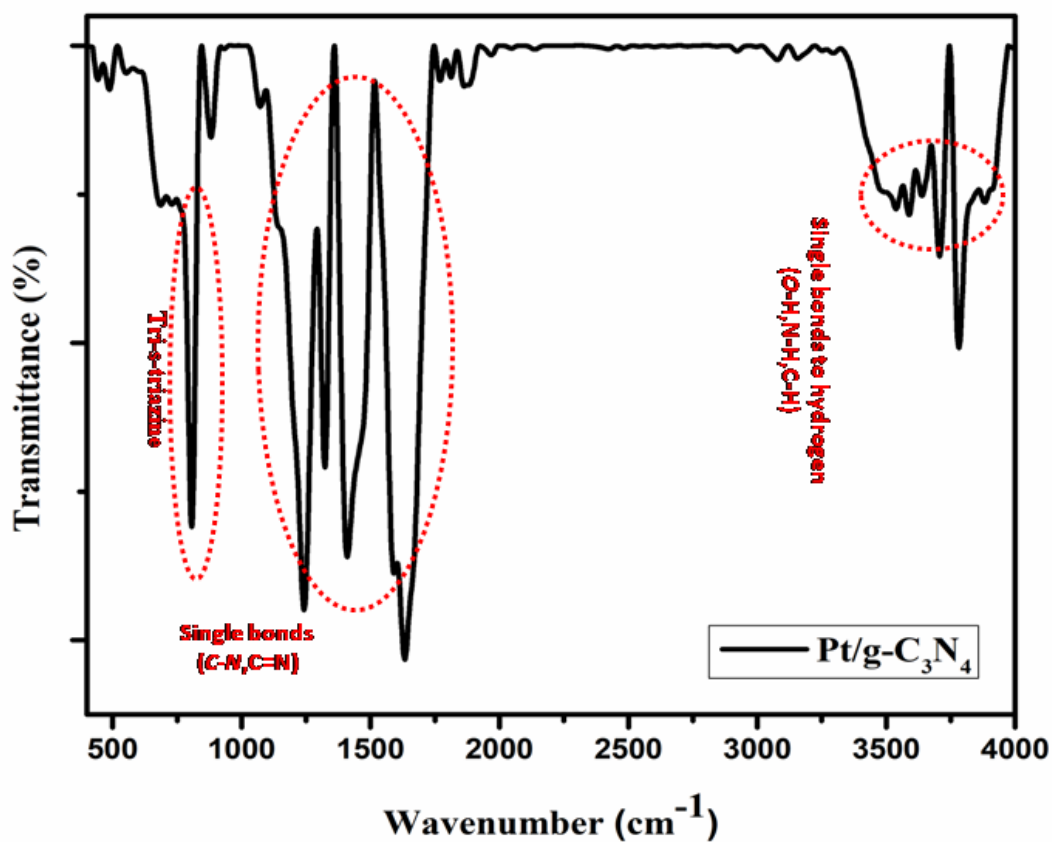


Figure 27: FTIR spectrum of Pt/g-C₃N₄

4.3.6 Photoluminescence Spectroscopy (PL):

PL analysis was done to evaluate the bandgap and carrier recombination property of the material, as shown in Fig. 28. PL spectra were recorded with an excitation wavelength of 325nm at room temperature. Pure $\text{g-C}_3\text{N}_4$ shows an emission peak at 435nm, which is attributed to the recombination of the photo-generated charge carriers, whereas $\text{Pt/g-C}_3\text{N}_4$ shows PL spectra at the same wavelength. However, the intensity of the peak decreases. The decrease in the peak intensity is attributed to the presence of Pt, which inhibits the recombination of photo-generated electron-hole pair. A slight blue shift in the peaks of $\text{Pt/g-C}_3\text{N}_4$ was observed from the spectra as compared to the pure $\text{g-C}_3\text{N}_4$.

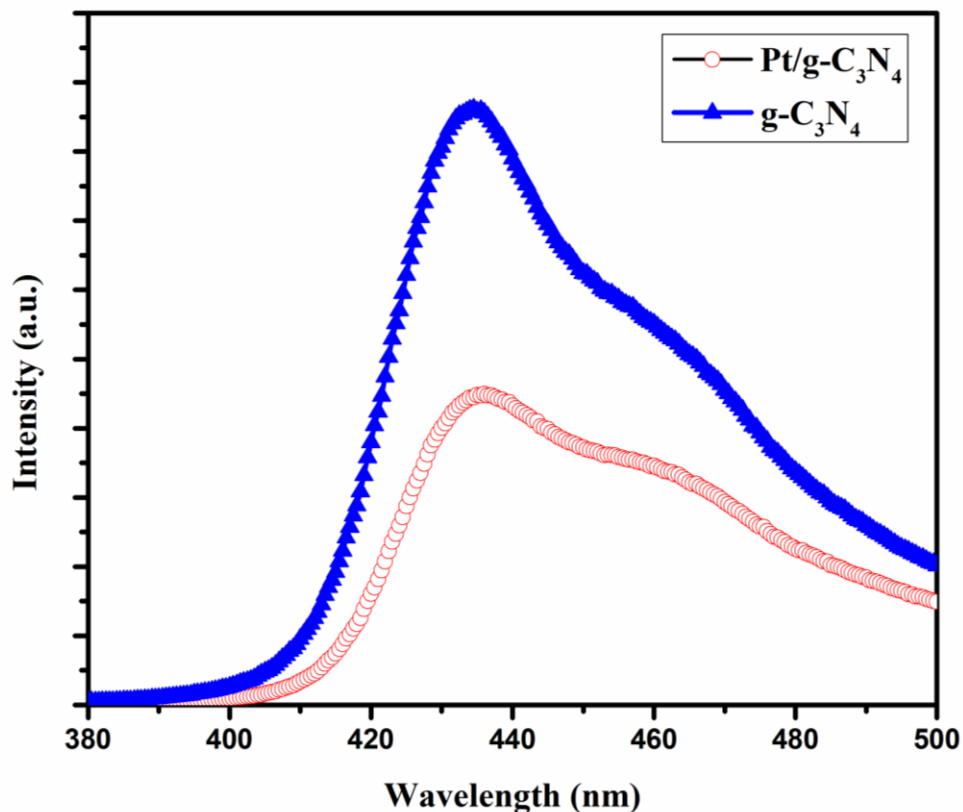


Figure 28: PL spectra for $\text{Pt/g-C}_3\text{N}_4$ and $\text{g-C}_3\text{N}_4$

4.4 Sensor fabrication

To fabricate the sensor, screen printing technology and nebulizer spray pyrolysis system was adopted. Carbon-based interdigitated electrodes were screen printed on top of a cleaned glass substrate. Thereafter, the Pt/g-C₃N₄ solution was made by mixing Pt/g-C₃N₄ fine powder into the 10 ml DI water. The solution was then taken into the jet nebulizer to deposit a thin layer of sensing material, as shown in fig—29 (a)(b).

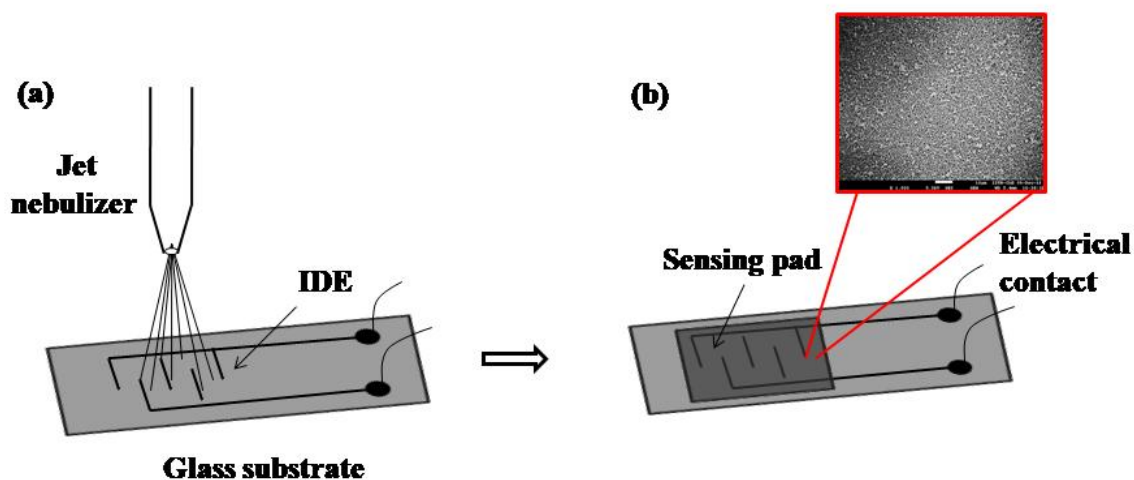


Figure 29: (a) deposition of sensing material on top of the IDE (b) Fabricated Pt/g-C₃N₄ gas sensor.

4.5 Hydrogen gas sensing:

The electrical resistance of the fabricated Pt/g-C₃N₄ sensor with respect to the presence and absence of hydrogen gas is shown in Fig. 30. To record the sensing parameters of gas sensor, continuous purging of air was performed for 1 hr to stabilize the resistance of the sensor followed by the annealing at 250°C. A proper vacuum was maintained by using a vacuum pump before the sensing. The zero air condition was chosen as pre-present gases could modulate the overall concentration of the analyte gas. During the purging of hydrogen gas, the overall

resistance of the sensor decreases, and after some period of time, resistance stabilized at a value corresponding to the gas concentration. A sudden increase in the sensor resistance was observed at no purging state, and it continues until the initial value reaches. The sensor response was recorded for the three different concentrations.

The percentage sensitivity (%), where R_g is the resistance at the presence of hydrogen gas, and R_o is the resistance of the sensor in the air (without analyte gas) is represented as:

$$S = \frac{R_o - R_g}{R_g} \times 100$$

As the principle of sense, when a hydrogen molecule interacts with the Pt nanoparticle present in the materials, van der Waal force induced. Due to the interaction of Pt with hydrogen molecules, a molecule dissociates into atoms and forms PtH_x . As a result of the interaction, the work function of Pt decreases, and electron transfer takes place from the Pt to $g-C_3N_4$ matrix. The decrement in the work function leads to enhancement to the charge carrier concentration in the material; as a result, overall resistance decreases [38]. The higher the concentration of hydrogen gas, the higher will be the change in resistance. The initial resistance of the sensor was recorded as $43\text{ M}\Omega$. After introducing 1%, 4%, and 10% of the hydrogen gas, the final resistance was recorded as $18.92\text{M}\Omega$, $11.61\text{M}\Omega$, and $4.21\text{M}\Omega$, respectively. Moreover, the overall sensitivity at different concentrations was found out to be 56, 73, and 90%, respectively. The sensitivity over the change in concentration is shown in Fig. 30(d). The stability over time is shown in Fig. 31, which shows the change in the resistance over time is almost stable with slight decay, which is due to environmental conditions.

Table 3: Comparison between drop cast and nebulized thin-film based Pt/g-C₃N₄ sensor with their sensitivity, response, and recovery time.

| Material | Gas concentration | Response time | Recovery time | Sensitivity (%) |
|-----------------------------|-------------------|---------------|---------------|-----------------|
| Pt/g-CN Drop-casted film | 1% | 11 min | 16 min | 56 |
| | 4% | 12 min | 19 min | 73 |
| | 10% | 16 min | 21 min | 90 |
| Pt/g-CN Nebulizer film | 1% | 39 sec | 5 sec | 81.3 |
| | 4% | 36 sec | 9 sec | 104.3 |
| | 10% | 28 sec | 17 sec | 137.9 |

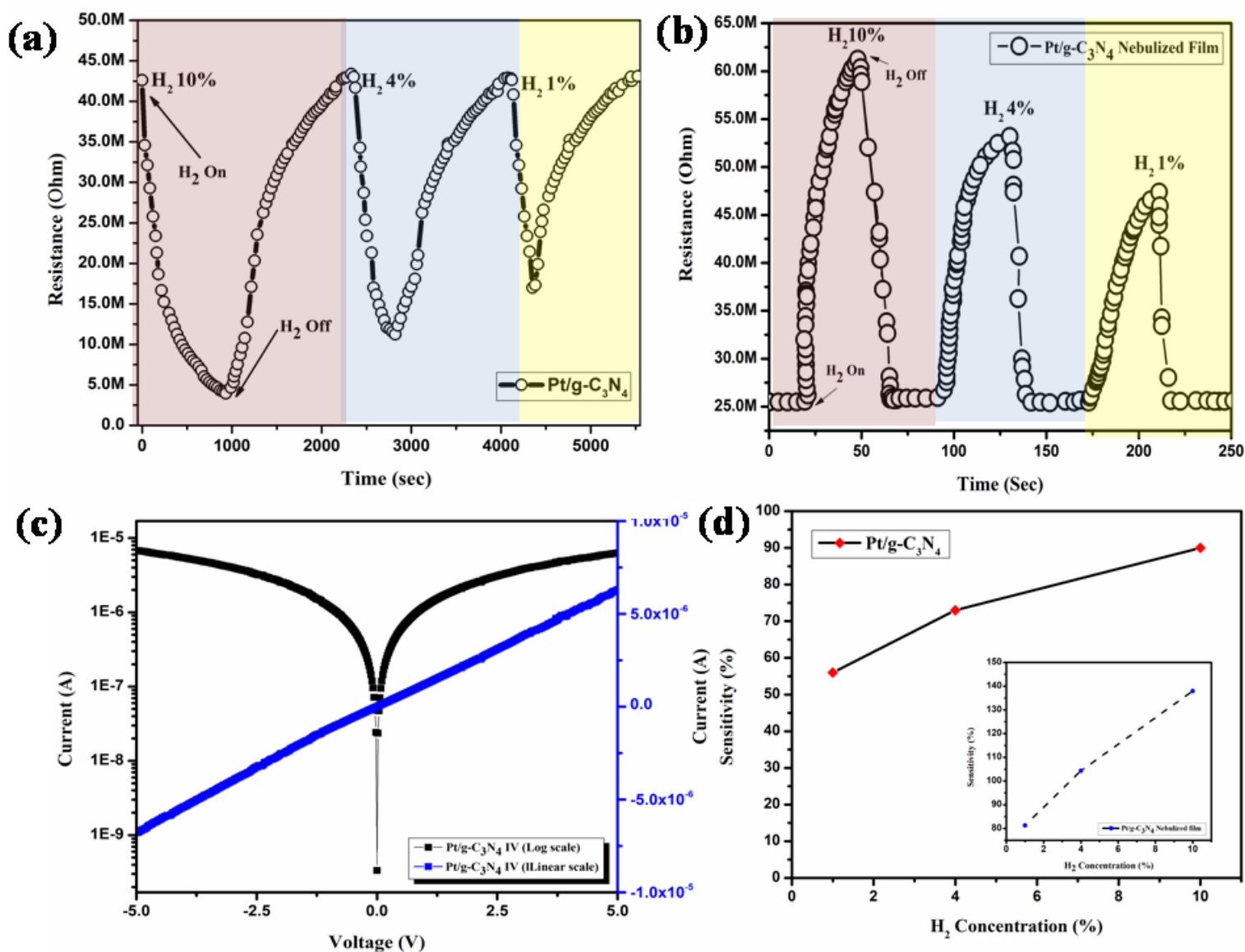


Figure 30:(a-b) Real-time electrical resistance response of Pt/g-C₃N₄ at 1%, 4% and 10% H₂ concentration at room temperature for drop casted and nebulized film (c) I-V curve of the sensor (d) Sensitivity of Pt/g-CN at 1%, 4% and 10% H₂ concentration at room temperature for drop casted and nebulized film (inset)

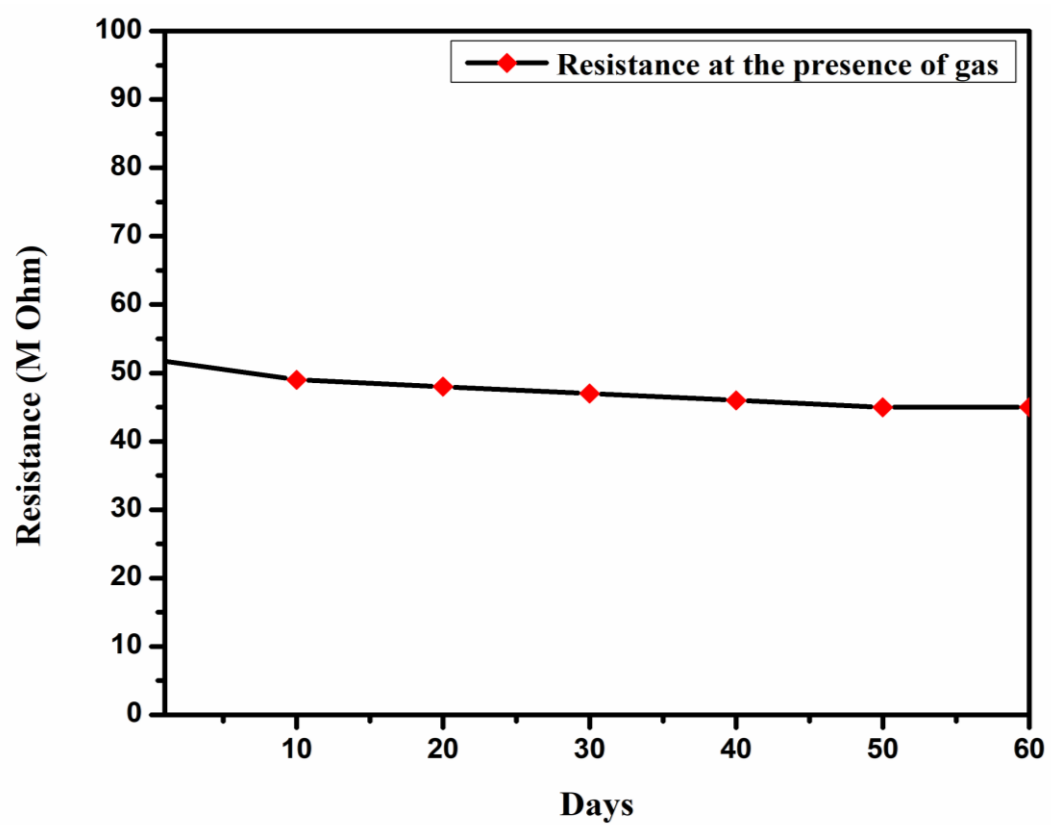


Figure 31: Stability of nebulized thin-film sensor over the periods of 60 days.

Chapter 5

Preparation, Characterizations, and testing of ZnO/g-C₃N₄ composite for efficient hydrogen gas sensing

5.1 Introduction:

In this chapter, the preparation of the ZnO/g-C₃N₄ nanocomposite is discussed. The synthesis of this nanocomposite is performed by the direct pyrolysis of the precursor (zinc acetate hexahydrate). The material synthesis is validated by different characterization tools, such as XRD, SEM, TEM, EDX, FT-IR, and PL. The SEM and TEM analyses reveal the formation of nanorods on g-C₃N₄ support. The gas sensing property of the ZnO/g-C₃N₄ was studied for various concentrations of hydrogen gas. Response and recovery times were recorded by the sensor, which is described in detail in this chapter.

5.2 Preparation of ZnO/g-C₃N₄ nanorods:

The synthesis process of the ZnO/g-C₃N₄ nanocomposite is illustrated in Fig.32. To synthesize the ZnO/g-C₃N₄ nanocomposite, melamine was taken as a precursor material for g-C₃N₄, and zinc acetate dehydrates for ZnO. All the materials taken for the synthesis were used as-received (i.e., without any further purification). For the synthesis, a very simple and cost-effective pyrolysis process was adopted. Four different wt% of the material were taken to form four sets of the test materials, namely 0.1 ZnO/g-C₃N₄, 0.2 ZnO/g-C₃N₄, 0.3 ZnO/g-C₃N₄, 0.4 ZnO/g-C₃N₄. To synthesize those sets, the required amount of melamine was taken and dispersed into the ethanol solution. Then zinc acetate dehydrate was added to the solution and kept on stirring at 50°C. Eventually a clear solution was obtained. The solution was kept in a muffle furnace for 5-6 hr to evaporate the solvent. After the evaporation of solvent, white powder was obtained. This was then transferred to alumina crucible (50ml) and closely packed using aluminum foil. Thereafter, obtained powder was heated up at 550°C for 5-6 hr at a 3°C/min ramp rate. As a result of the calculations, brown to dark brown powder was obtained with the varying wt% of

ZnO in the composite. The ZnO nanorods on g-C₃N₄ sheets were formed after the completion of the process, which was established by various morphological and microstructural characterizations. Further filtration or centrifugation was not required. The pure g-C₃N₄ was also synthesized for the comparison with the ZnO/g-C₃N₄ nanocomposite.

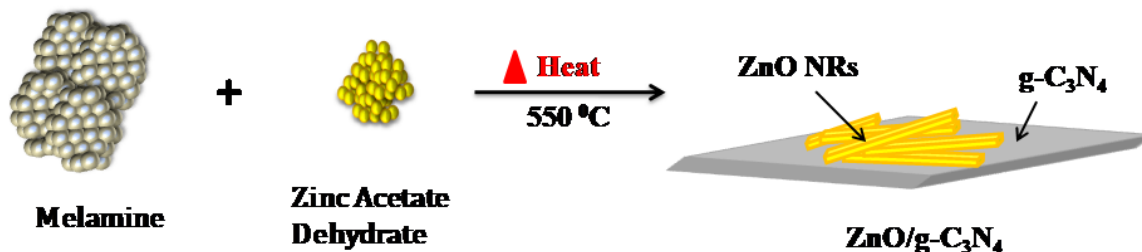


Figure 32: Schematic of ZnO/g-C₃N₄ synthesis.

5.3 Material Characterizations

5.3.1 X-Ray Diffraction:

The XRD spectrum for ZnO/g-C₃N₄ is shown in Fig. 33. g-C₃N₄ gives two peaks at 12.9 and 27.5, which corresponds to 100 and 002 lattices. The peak at 27.5 corresponds to interplanar stacking peaks of aromatic rings, and that at 12.9 corresponds to interlayer structure [115-118]. The interplanar spacing of the two peaks was obtained as 0.685 nm and 0.323 nm, respectively. The ZnO peaks are recorded at 31.8, 34.5, 36.3, 47.6, 56.7, 62.9, 69.2 which correspond to 100, 002, 101, 102, 110, 103, 112 lattices respectively (JCPDS 36-1451). No other peaks were recorded, which confirmed the very high purity of the material [119]. ZnO shows a hexagonal wurtzite structure, which was also confirmed by SEM. The prepared sample is polycrystalline in nature. In ZnO/g-C₃N₄ it was observed that g-C₃N₄ peak intensity decreases as the amount of ZnO increases due to the strong peak intensity of ZnO particles. After the formation of composites, no changes in g-C₃N₄ peaks were observed, which indicates highly stable layers of g-C₃N₄ after the synthesis. It is observed that the crystalline phase of the ZnO in composite

improves as the amount of ZnO increases in the ZnO/g-C₃N₄ nano-composites. ZnO[120]. Diffraction peaks in ZnO/g-C₃N₄ composites and pure ZnO do not change. Hence, it is confirmed that the degree of crystallinity of the ZnO does not change.

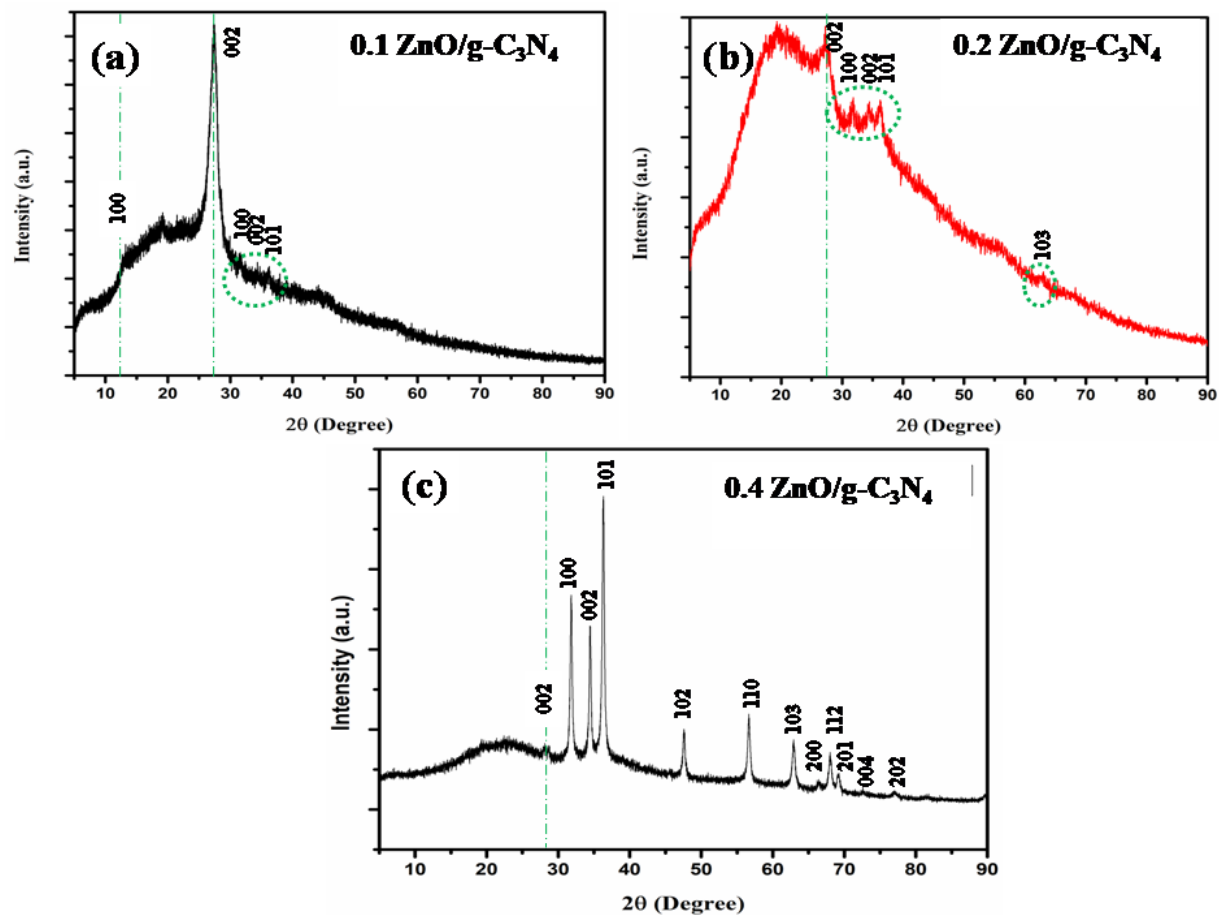


Figure 33: XRD spectra of (a) 0.1 ZnO/g-C₃N₄(b) 0.2 ZnO/g-C₃N₄(c) 0.3 ZnO/g-C₃N₄.

5.3.2 X-ray Photoelectron Spectroscopy:

To determine the chemical status and composition of the elements present in the ZnO/g-C₃N₄ nanocomposite, X-ray photoelectron spectroscopy (XPS) was performed. XPS survey spectrum for the ZnO/g-C₃N₄ nano-composite is shown in Fig.34, which indicates the presence of Zn 2p, C 1s, N 1s, and O 1s in the material. Two distinct peaks at 1020.4 eV and 1043.5 eV are assigned to Zn 2p_{3/2} and Zn 2p_{1/2} [121]. These peaks are the same as the binding energy of Zn²⁺, i.e., Zn atoms exist in 2+ oxidation states in the ZnO material [122-124]. Zn 2p_{3/2} peaks correspond to the Zn-O bond [10]. The spin-orbit splitting or energy differences between two peaks are 23.1 eV. Similarly, O 1s high-resolution spectrum can be deconvoluted at 531.6 eV peak, which corresponds to lattice oxygen of ZnO as well as surface hydroxyl (–OH) or O₂ adsorbed on the composite [125].

C 1s shows three peaks at 284.6, 286.5, and 288.4 eV. These correspond to –NH₂ group, and sp² bonded carbon (N-C=N) in the aromatic structure [125-126]. N 1s can be deconvoluted into three peaks 398.5, 400.6, and 404.3 eV. Peaks at 398.5 eV and 400.6 eV are attributed to sp² hybridized nitrogen (C-N=C) and tertiary nitrogen (N-C). Another peak at 404.3 eV corresponds to amino groups (N-H or Ar-NH₂) [126-127]. The binding energy of C 1s and N 1s in ZnO nano rods is observed to be slightly shifted as compared to the pure g-C₃N₄. This confirms strong interaction between the two materials and also concludes that ZnO/g-C₃N₄ is successfully synthesized. All the required elements are present in the composites. Also, the phase the as-prepared ZnO/g-C₃N₄ is stable.

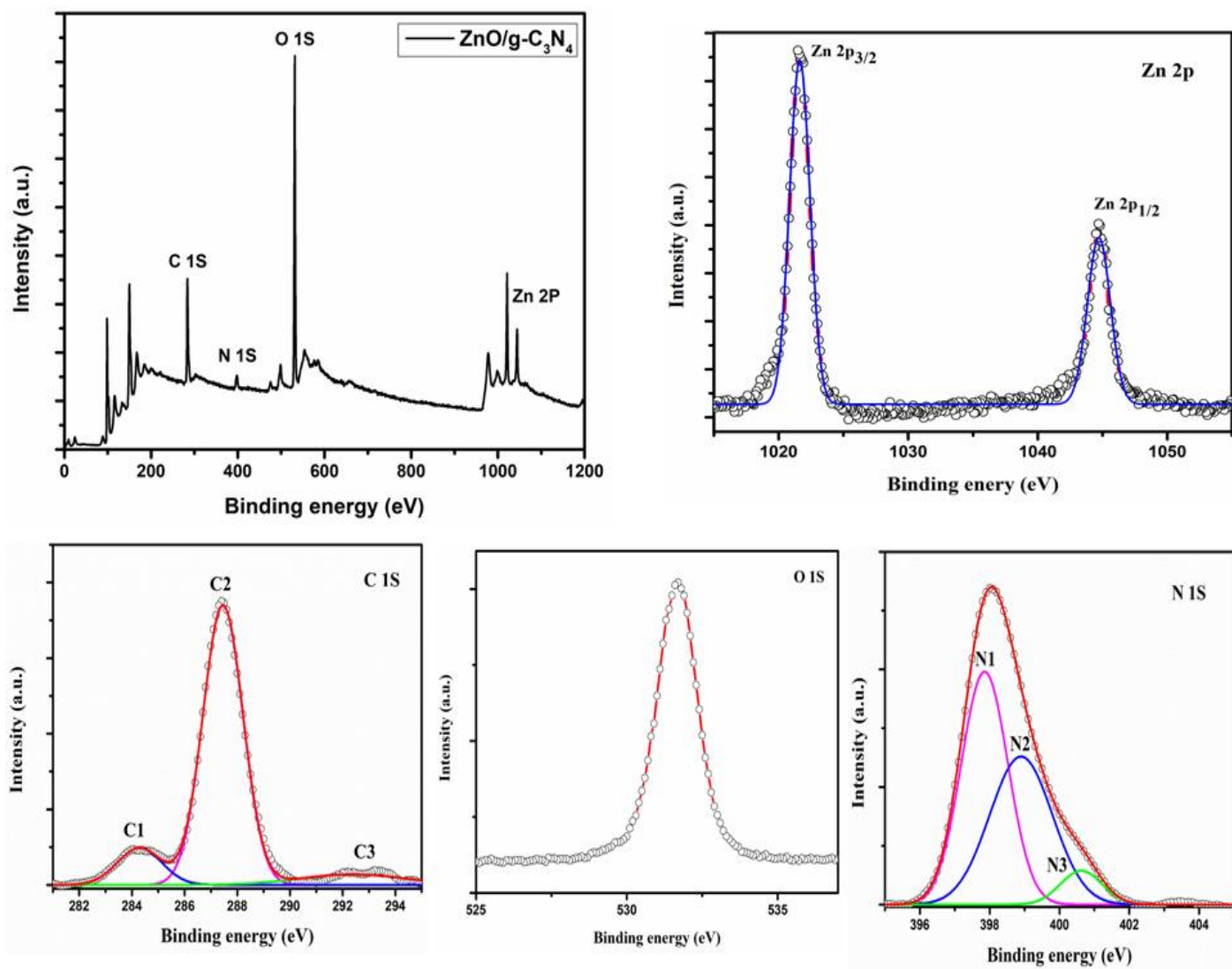


Figure 34: XPS spectra of ZnO/g-C₃N₄ and its deconvoluted peak of Zn 2p, C 1s, O 1s, N 1s.

5.3.3 FTIR:

FTIR was used to evaluate the bonding of atoms as well as the vibrational modes, as shown in Fig. 35. FTIR sample was prepared by the KBr pellet method in the wavenumber range 400-4000 cm^{-1} . The peak at 557 cm^{-1} represents the Zn-O stretching bond. Peak at 810 cm^{-1} is due to the characterization absorption of triazine units [128-130]. Peaks at 1233 – 1626 cm^{-1} are attributed to C=N stretching and aromatic C-N stretching, respectively [130-132]. Peaks at 1900-2200 cm^{-1} correspond to the cyano group, ($\text{C}\equiv\text{C}$, $\text{C}\equiv\text{N}$). Peaks at 2900-3400 cm^{-1} correspond to the NH group. It also refers to a single bond to hydrogen atoms, i.e., O-H, N-H, C-H, respectively [125, 132-133].

It is determined that the peak intensity at 2900-3400 cm^{-1} for ZnO/GCN reduces as the amount of ZnO introduced into the composite increases. The reduction of peak intensity indicates the removal of an amine group, i.e., low hydrogen content in the composite during the pyrolysis process.

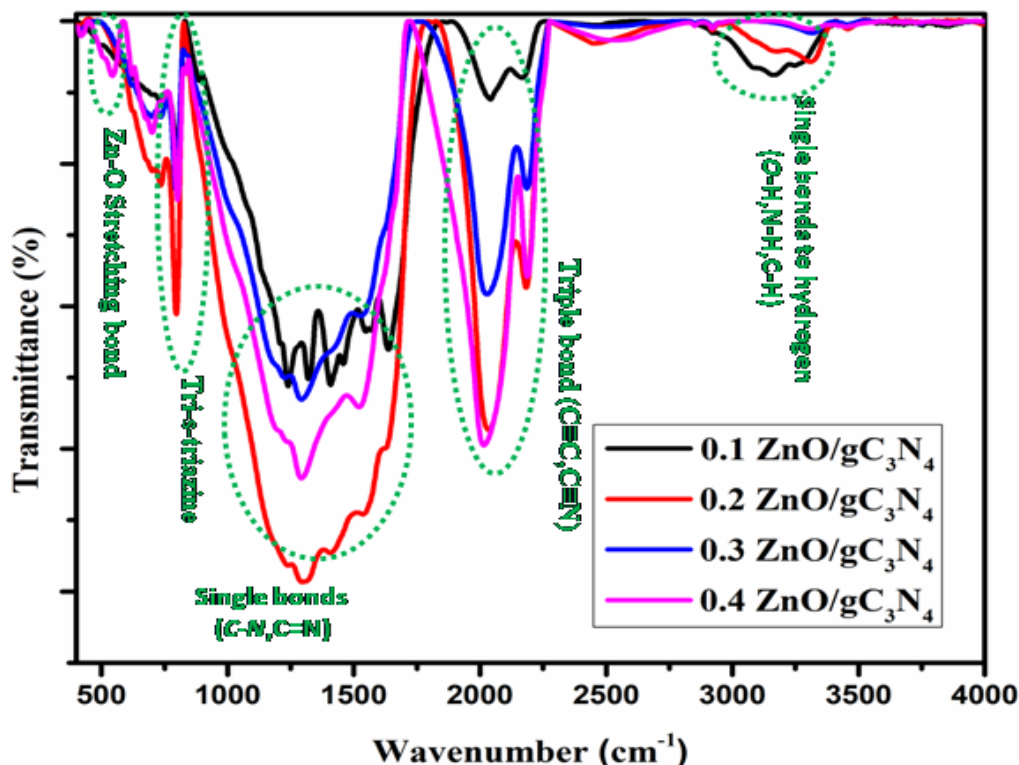


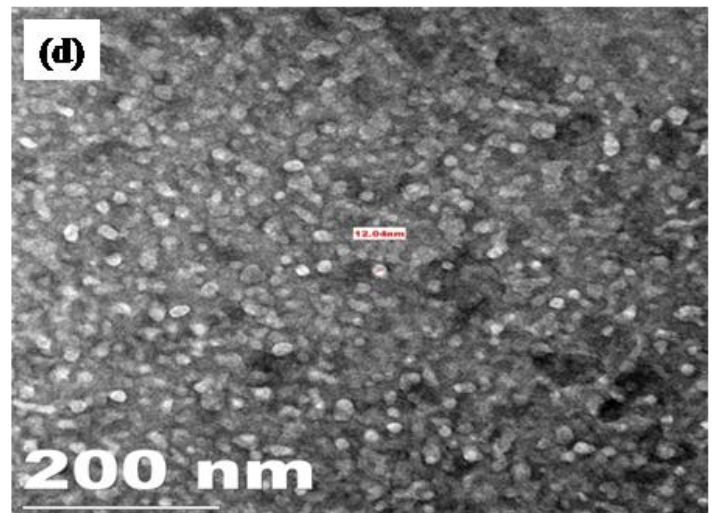
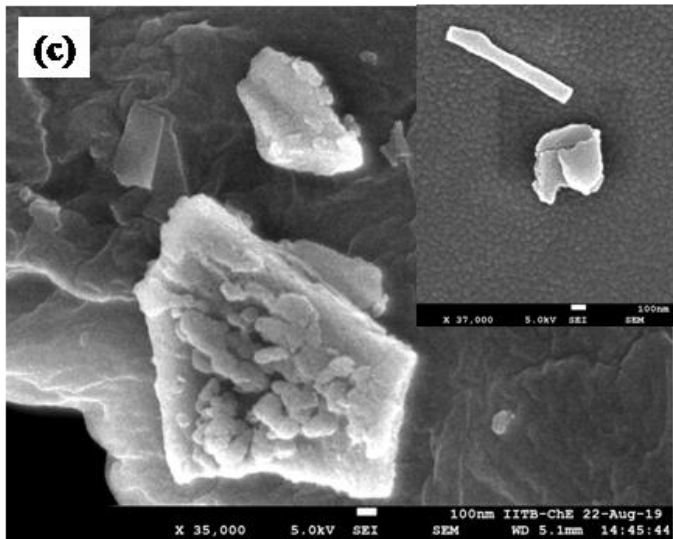
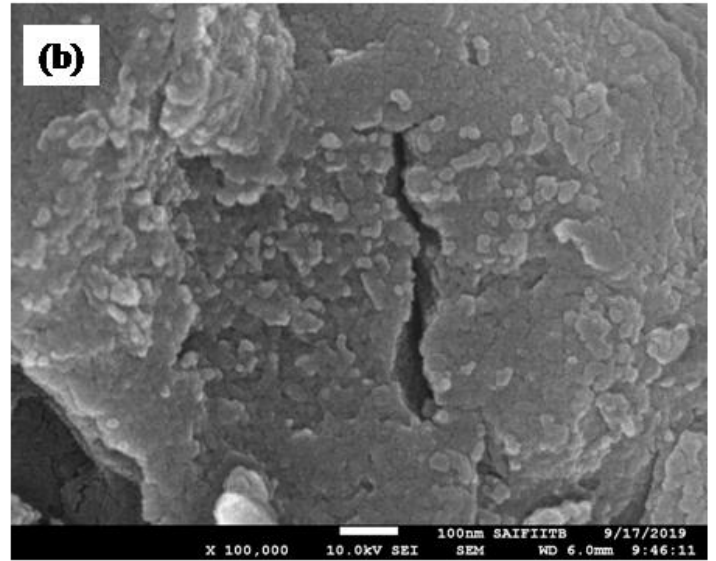
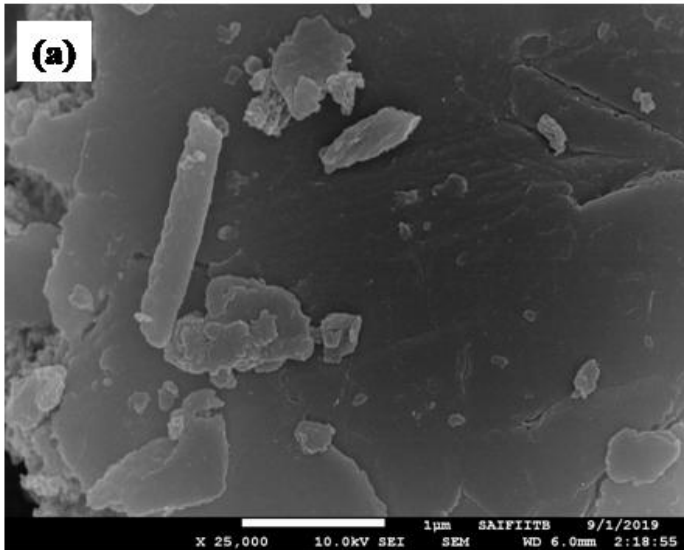
Figure 35: FTIR spectra of ZnO/GCN with different ZnO content.

5.3.4 FESEM and TEM:

SEM and TEM analyses were performed to investigate the surface morphology and microstructure of the prepared sample. SEM image reveals the irregular sheets of g-C₃N₄ with variation in size. It was also observed that g-C₃N₄ sheets have bending edges due to the surface tension. ZnO/ g-C₃N₄ nanocomposite was analysed at four different compositions, i.e., 0.1 ZnO/ g-C₃N₄, 0.2 ZnO/ g-C₃N₄, 0.3 ZnO/ g-C₃N₄, 0.4 ZnO/ g-C₃N₄, as shown in Fig 36(a),(b),(c)&(e) respectively. The g-C₃N₄ and ZnO can easily be identified by the color contrast between the two materials.

SEM image of 0.1ZnO/ g-C₃N₄ shows ZnO sheets impregnated on the surface of g-C₃N₄. The size and shape of the sheet of ZnO were not well defined. The 0.2 ZnO/ g-C₃N₄ and 0.3 ZnO/ g-C₃N₄ show the cocoon-likeZnO, which is in the initial stage of growth as a rod and finally some rods are formed. It was also observed that the incorporation of ZnO into the g-C₃N₄enhances the porosity of the overall composite. However, the porosity introduced in the composite is beneficial in our study as the porosity works as effective trapping sites for the gases [10/114-11/115]. Hence, the overall performance of the gas sensor increases towards the analyte. The 0.4 ZnO/ g-C₃N₄ shows the excellent formation of ZnOnanorods on the g-C₃N₄ sheets. The size of the rods is about 400-500nm. The formed rods show hexagonal wurtzitestructures, which are completely matched with the XRD result.

TEM images of the GCN and ZnO/ g-C₃N₄are shown in Fig 36 (d)(f). The g-C₃N₄has 2D sheets with irregularity in shape and size, as alsodepicted in SEM. The ZnO/g-C₃N₄TEM analysis shows that when the concentration of ZnO is low, it shows sphere-like morphology and as the concentration increases, ZnOnanorods form as can be seen in Fig. 36. ZnOnanorods are anchored to the g-C₃N₄sheet. The size of the nanorods is 400-500nm or greater. The material can be easily identified from the interplanar spacing.The spacing of 0.26nm in Fig 36(f) corresponds to ZnO. This confirms the presence of ZnO in the composites.



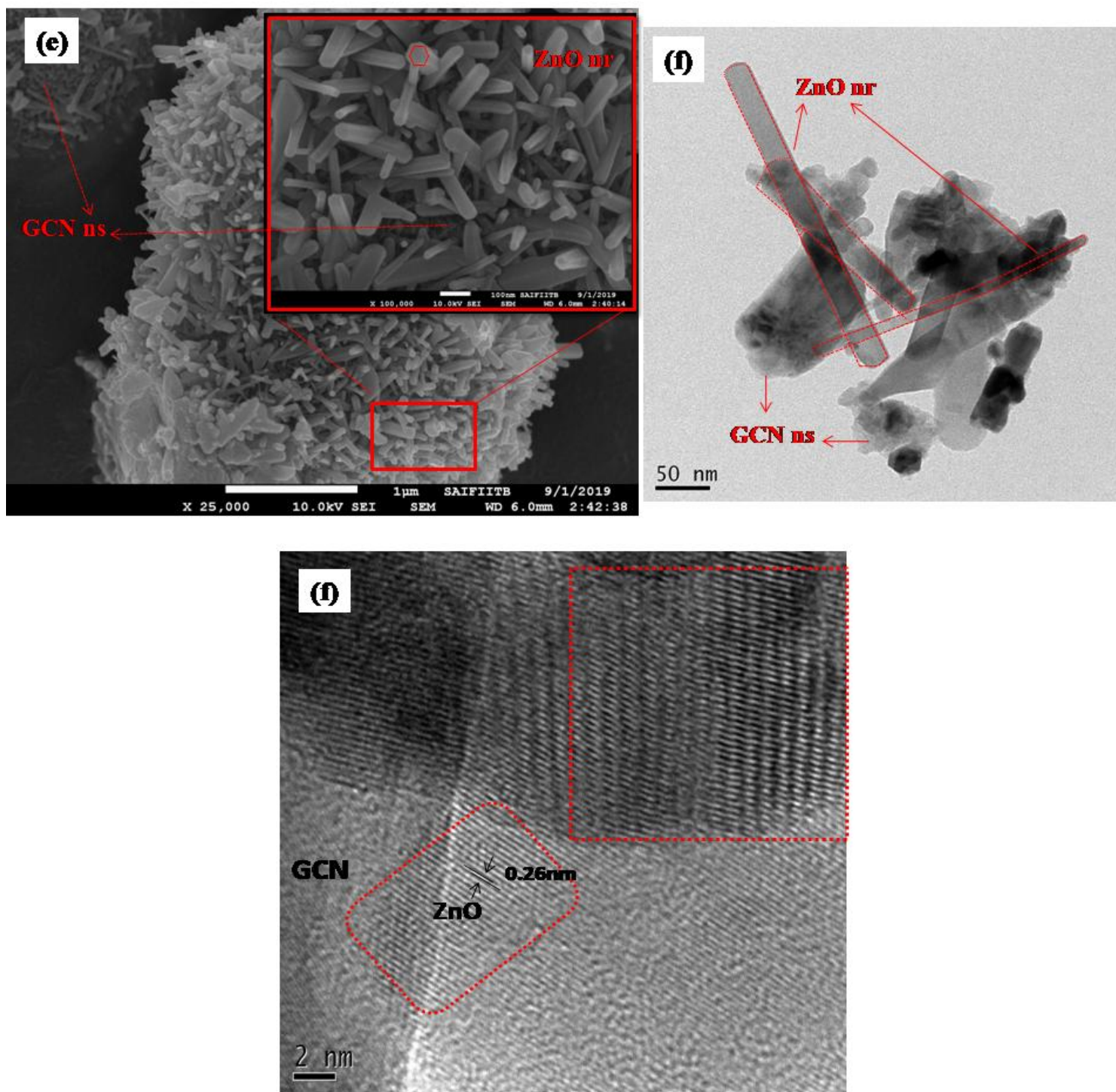


Figure 36: FESEM of ZnO/ g-C₃N₄ (a) 0.1 ZnO/ g-C₃N₄ (b) 0.2 ZnO/ g-C₃N₄ (c) 0.3 ZnO/ g-C₃N₄ (e) 0.4 ZnO/ g-C₃N₄. TEM image of (d) 0.2 ZnO/GCN (f) 0.4 ZnO/GCN (f) Interplanar spacing of ZnO/GCN.

5.3.5 Energy Dispersive X-Ray (EDX) Spectroscopy:

EDX analysis for the synthesized ZnO/g-C₃N₄ composite was done to confirm the presence of elements. As shown in Fig.37, EDX was performed in the selected area of the ZnO/g-C₃N₄ composite. The peaks for C, N, O, and Zn can easily be seen in the EDX spectrum. Apart from these elements, some other element peaks were also observed (which are attributed thin coating required for improving the conductivity and imaging). The elemental area mapping for the selected area and the presence of all the expected elements is clearly evident. Therefore, it is confirmed that the ZnO/g-C₃N₄ nanocomposite has all the expected elements present. As there are no other peaks (except for those corresponding to coating), the synthesized ZnO/g-C₃N₄ composite was concluded to be of high purity.

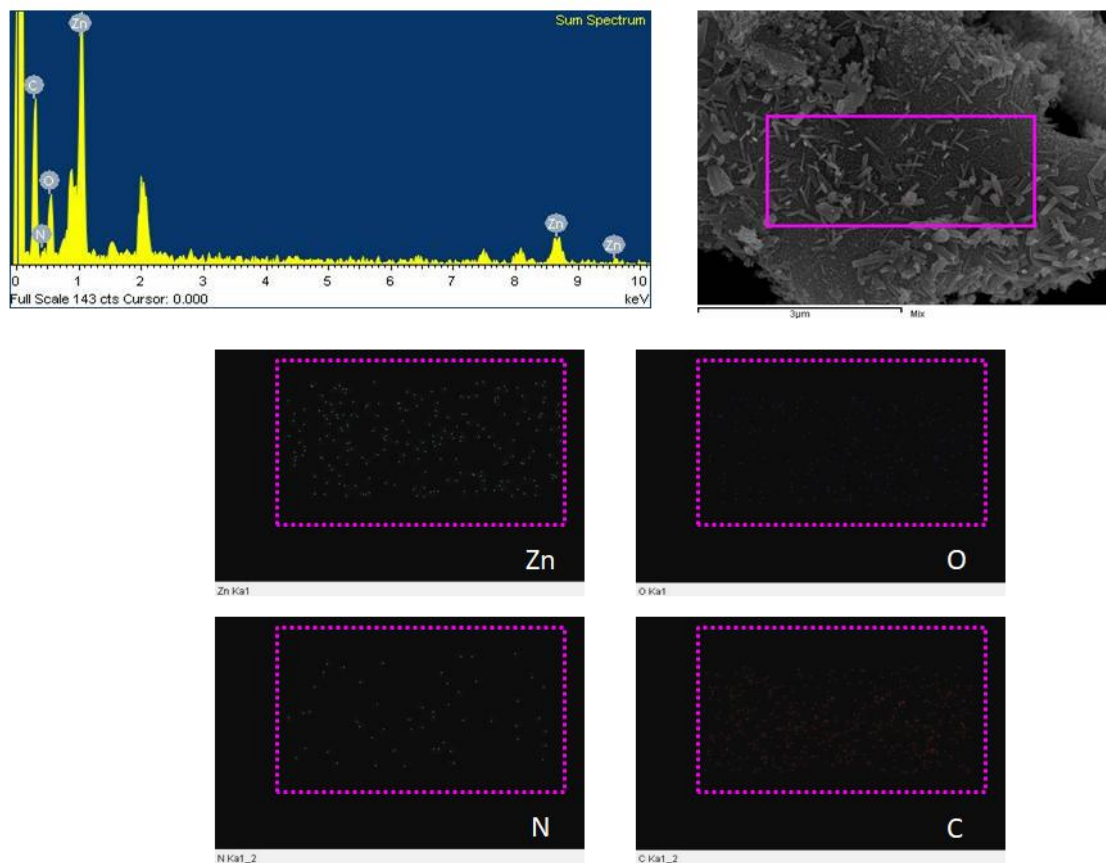


Figure 37: EDX analysis of ZnO/GCN. Elemental area mapping of Zn,O,N,C.

5.3.6 Photoluminescence (PL) study:

The photoluminescence (PL) study was done to investigate the recombination of photogenerated electron-hole pair and the bandgap of the synthesized composite as shown in Fig 38. PL spectra were examined into two regions, i.e., UV and visible. All the PL spectra were recorded with an excitation wavelength of 325nm at room temperature. Pure g-C₃N₄ shows an emission peak at 435nm, which is attributed to the recombination of the photogenerated charge carriers. In the case of ZnO/g-C₃N₄, the peak intensity was observed to decrease exponentially as the ZnO concentration increases in the composites, suggesting a reduction in the recombination of charge carriers. The peaks around 365nm appearing in the entire sample corresponds to near band edge emission of ZnO. The presence of ZnO and g-C₃N₄ emission peaks in the PL spectrum reveals the formation of ZnO/g-C₃N₄ composites. In order to understand the photo-induced charge separation and transfer in the prepared photocatalysts, the photoluminescence mechanism is explained as follows. When the g-C₃N₄ was excited at an excitation wavelength (325 nm), electrons from the valence band are transferred to the conduction band, leaving the holes in the former. The transferred electrons in the conduction band recombine with the holes in the valence band after releasing its energy, resulting in PL emission. The observed higher photoluminescence intensity indicates the higher recombination rate of photo-induced electron-hole pairs in the g-C₃N₄ sample. In the case of ZnO/g-C₃N₄ nanocomposites, the photo-induced electrons from the conduction band of g-C₃N₄ are transferred to the conduction band of ZnO, as the conduction band edge potential of g-C₃N₄ (-1.12 eV) is more negative than that of ZnO (-0.2 eV). In the meantime, the holes in the valence band of ZnO are transferred to the valence band of g-C₃N₄. This separation and transfer of charge carriers in the ZnO/g-C₃N₄ composite samples effectively inhibit the recombination process leading to the observed lower PL intensity.

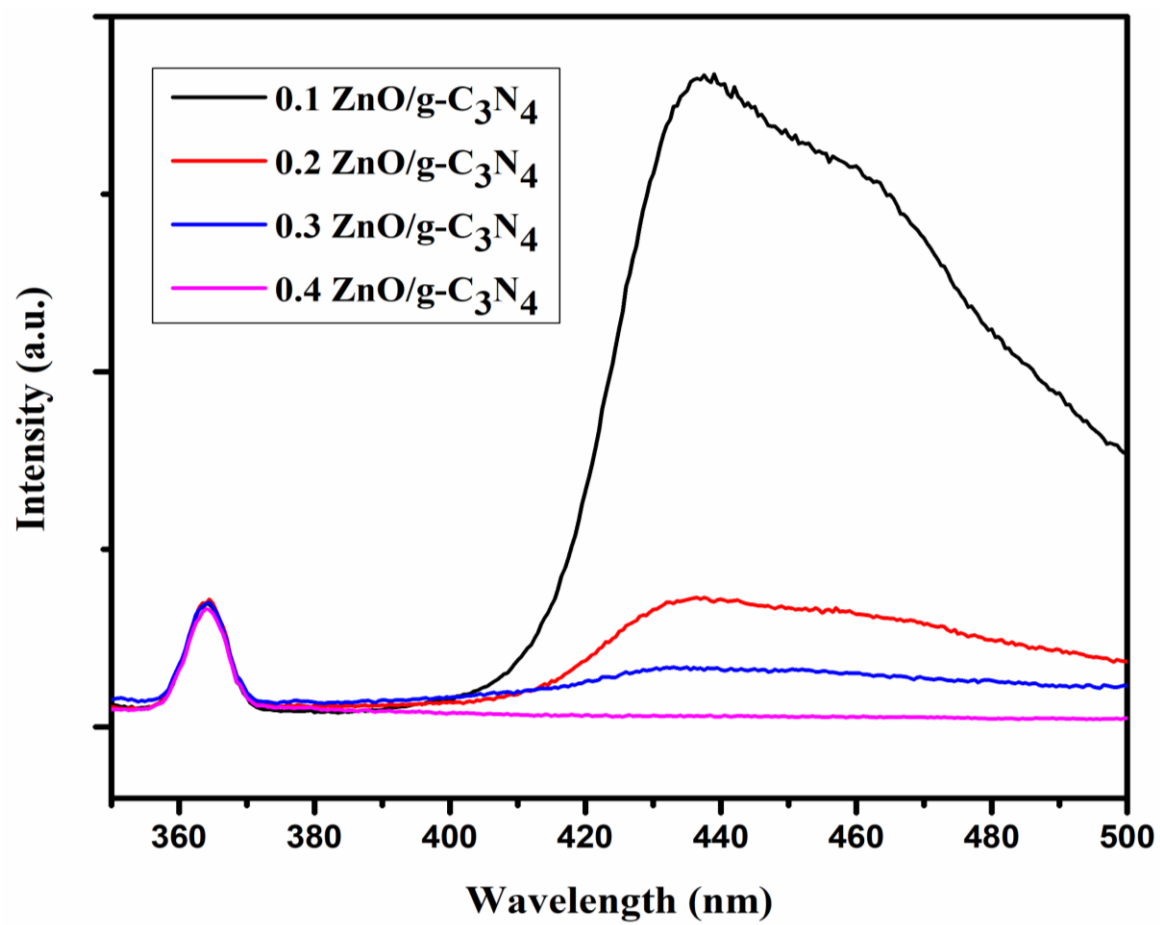
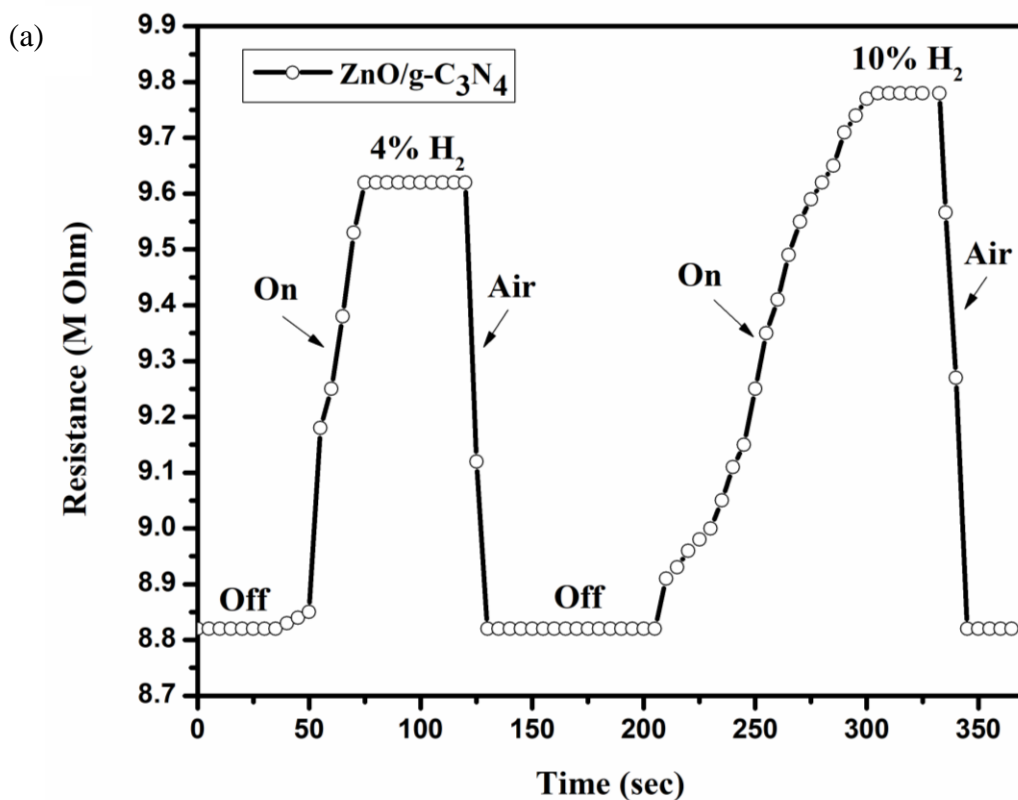


Figure 38: PL spectra of ZnO/g-C₃N₄ at different ZnO concentrations.

5.4 Gas sensing measurement:

Gas sensing measurement has been performed on a fabricated sensor, as shown in Fig 39. Carbon interdigitated electrodes were fabricated on top of pre-cleaned glass substrates. Sensing material was deposited by using drop-casting. The figure below shows the change in resistance with respect to various concentrations of gas. The response and recovery time of the sensor were measured for 4% and 10% hydrogen gas. The response time for the 4% hydrogen concentration was observed to be 65 sec, and it was 90 sec for 10% hydrogen concentration.



(b)

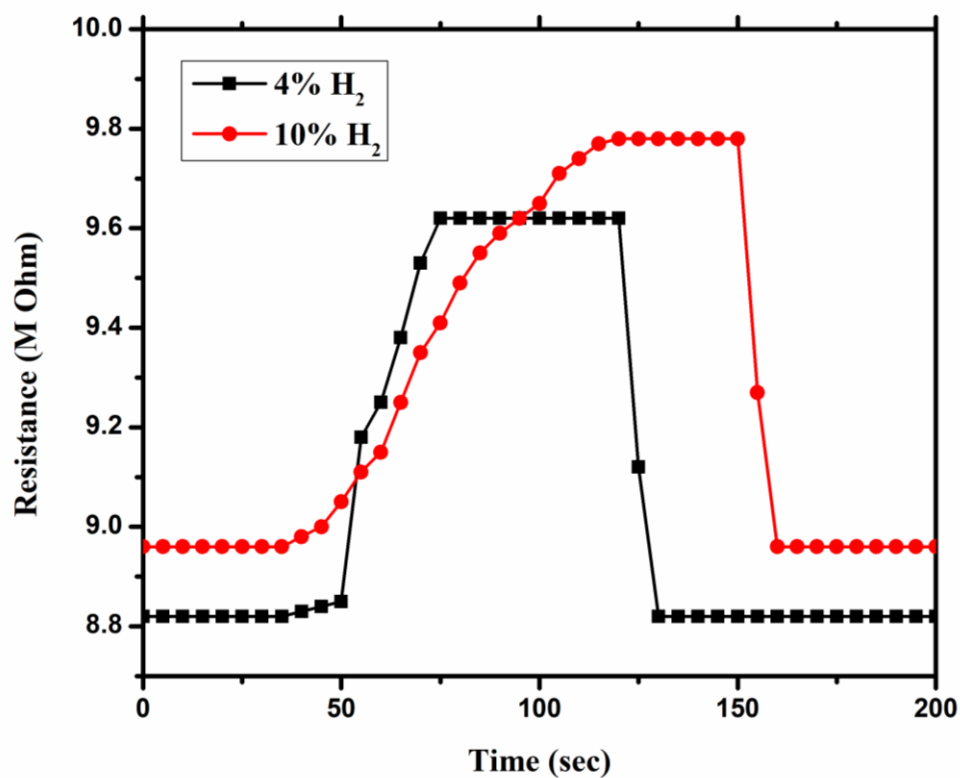


Figure 39: Real-time electrical resistance response of ZnO/g-C₃N₄ at 4% and 10% H₂ concentration at room temperature.

Table 4: Response and recovery time of the ZnO/g-C₃N₄ sensor at 4% and 10% concentration.

| Material | Gas concentration | Response time | Recovery time |
|-------------------------------------|-------------------|---------------|---------------|
| ZnO/g-C ₃ N ₄ | 4% | 20 sec | 3-5 sec |
| | 10% | 55 sec | 3-5 sec |

Chapter 6

RLC modeling of gas sensor

The sensors' modeling was done on the obtained RLC data from the RLC multimeter. RLC meter is the same as a digital meter, which has the ability to measure values of inductance (L), resistance (R) and capacitance (C), respectively. RLC meter, also referred to as impedance meter, is a measuring instrument used to measure any complex electrical impedance with respect to change in the frequency.

To find out the change in the parameters of the sensor at the presence and the absence of the hydrogen gas, sensor was connected to the impedance meter. The connected sensor was properly housed into the gas sensing setup. The changes in the parameters like capacitance, inductance, and resistance were recorded for various different concentrations of the gases at different operating frequencies. The changes in the parameter values were recorded and those data were used to model an RC first-order and RLC second-order filter. The changes in the graphs clearly depict the presence and the absence of analyte gas.

Let us consider the current following through the sensor circuit is given as:

$$I_{sensor}(t) = I_S \sin \omega t$$

By using Ohm's law, the voltage across the resistor connected in series would be given as follows

$$V_R(t) = RI_{sensor}(t) = R \cdot I_S \sin \omega t$$

Similarly the voltage drop across the capacitor,

$$V_C(t) = \frac{1}{C} \int I_S \sin \omega t \, dt$$

Similarly the voltage drop across the inductor,

$$V_L(t) = L \frac{d(I_S \sin \omega t)}{dt}$$

The impedance of the RC circuit is as follows

$$\frac{V_C(t)}{I_{sensor}(t)} = \frac{1}{j\omega c}$$

RLC first and second-order modeling and analysis:

Fig. 40 shows the RC first-order filter, which has a resistor in series with a capacitor. The values of R and C are taken from the recorded data, which is shown in the table 5 below. For the modeling of the sensor, several recorded data for various gas concentrations were used. Similarly, RLC second-order circuit was used to realize the sensor behavior by putting the different values of R, L, and C attributed to various concentrations of the analyte gas.

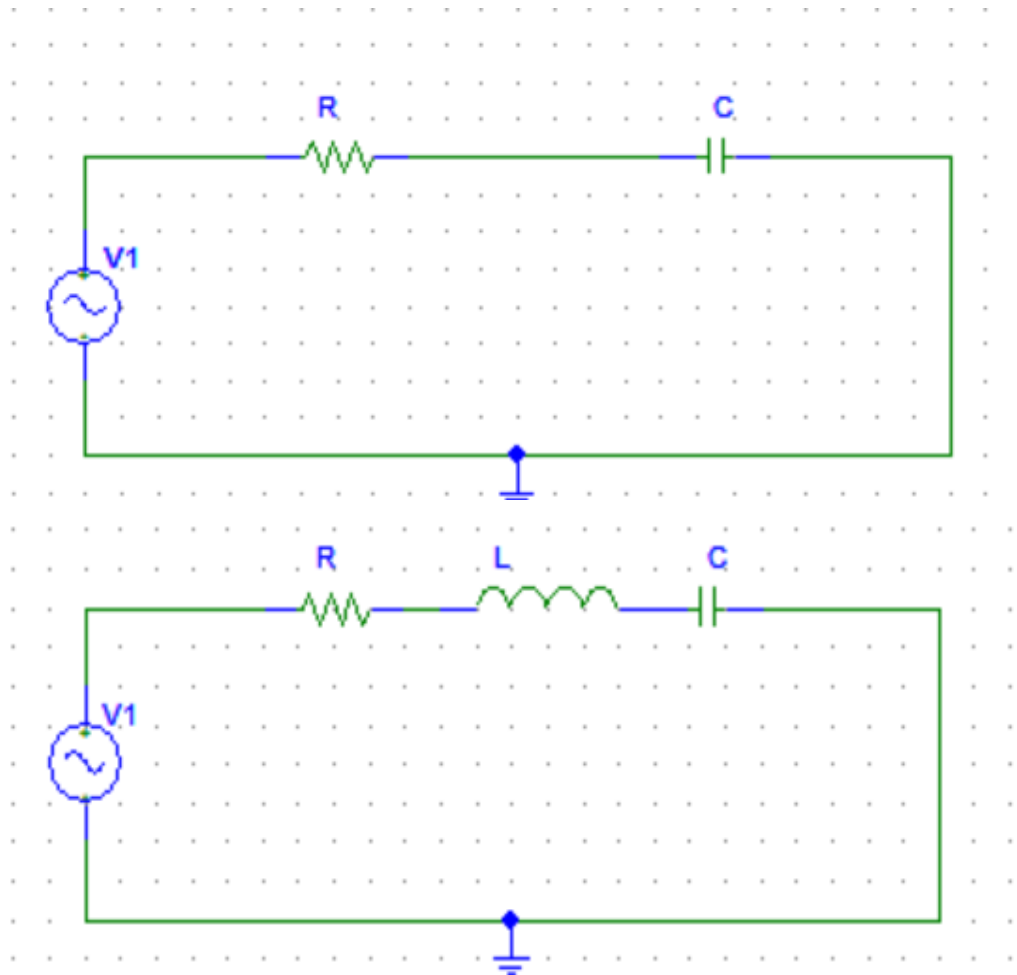


Figure 40: (a) RC (b) RLC circuit arrangement for the impedance measurements.

Fig 41 shows the change in the resonance frequency of the sensor in the presence and absence of the analyte gas. Fig 41(a) depicts the changes in the response for the three different loadings of the active Pd loading into the nanocomposite as 10%, 20%, and 40% respectively.

The results for no loading, i.e., pure $\text{g-C}_3\text{N}_4$ is shown in fig 41(c). From the figure, it is clear that Pd acts as an adsorbing material; therefore, a material with no loading does not show any possible changes during the presence and absence of the gas at various concentrations. Hence, no changes were recorded for the first-order and the second-order filter, as shown in figure.

The 20% Pd/ $\text{g-C}_3\text{N}_4$ shows slight changes for the analyte gas at different concentrations. From the first-order, it is clear that as the gas concentration increases gradually, the slope shifts upward direction, as shown in fig 41(b). Similarly, the second-order circuits show the variation in the impedance as it is exposed to a higher concentration.

Similarly, changes were observed for other Pd loaded materials, as shown in the figure. Higher concentration gives better response and variation to the peaks.

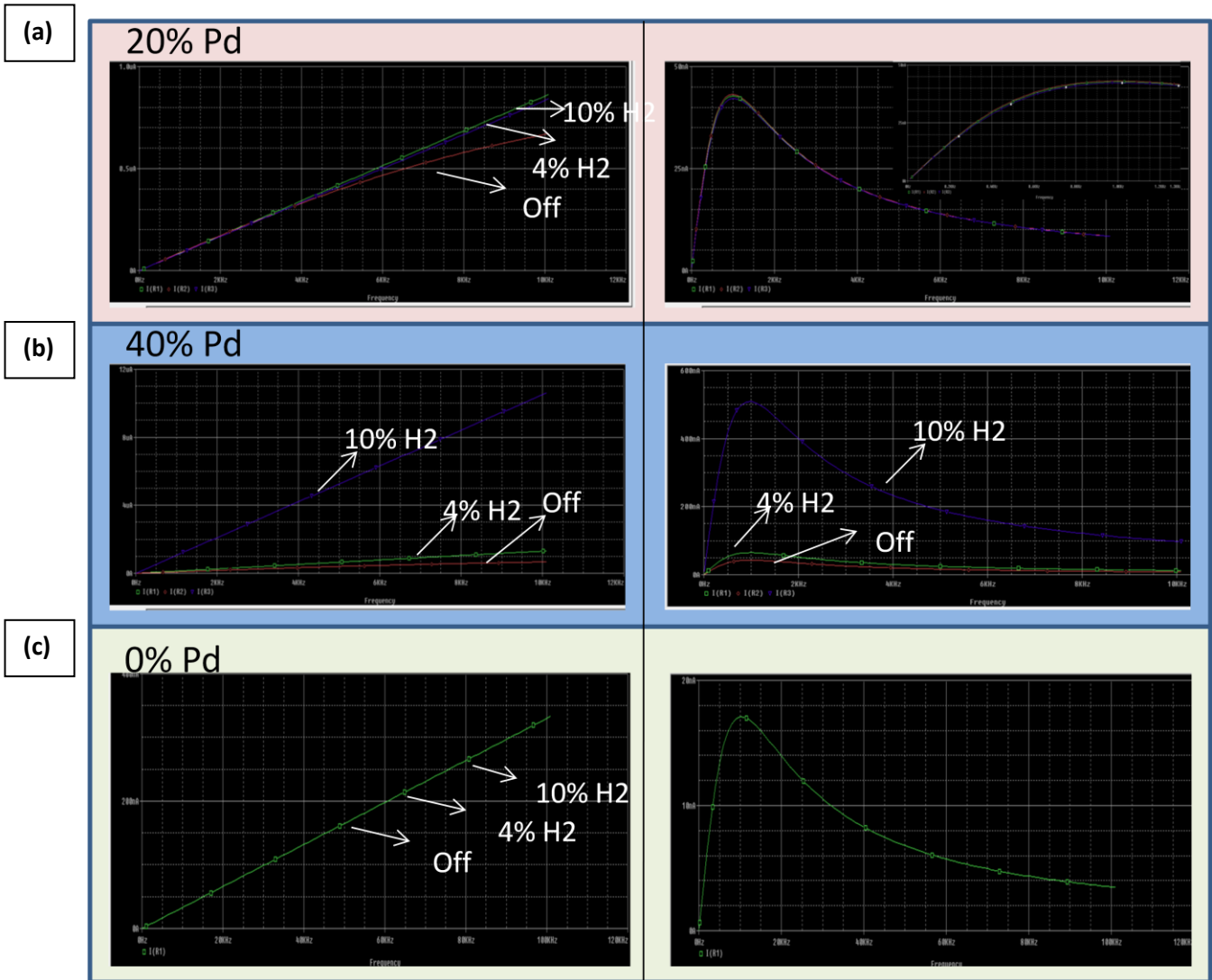


Figure 41: Impedance response of the first order and the second-order filter for Pd loading of 20% and 40% at a gas concentration of 4% and 10%, respectively.

Table 5: R,L,C values of sensor at 1%, 4%, 10% concentration of analyte gas.

| Pd/g-C₃N₄ (20% loading) | | | | | | | |
|--|------------------|--------------------------|-------------------------|--------------------------|--------------------------|-------------------------|-------------------------|
| Concentration | Frequency | R_p (Ω) | R_s(Ω) | C_p(pf) | C_s(pf) | L_p(H) | L_s(H) |
| 0% H ₂ | 20 Hz | -- | -- | 14.7955 | 78.4735 | -- | -- |
| | 100 Hz | -- | 39.6970M | 14.8343 | 18.9923 | -- | -- |
| | 1 Hz | 87.0631M | 1.64467M | 13.3744 | 13.6174 | -1.9135k | -1.8603k |
| | 10 Hz | 14.8367M | 123.386k | 11.6931 | 11.7882 | -21.6474 | -21.5019 |
| | 100 Hz | 2.1299M | 12.2417k | 9.97551 | 9.9968 | -254.63m | -253.35m |
| | 1 M Hz | -45.1104k | -1.5920k | 18.3492 | 18.9495 | -1.3875m | -1.3458m |
| | | | | | | | |
| 10% H ₂ | 20 Hz | -- | -- | 14.3812 | 16.7577 | -- | -- |
| | 100 Hz | -- | 11.0978M | 13.1712 | 15.4987 | -- | -- |
| | 1 Hz | -- | 1.1043M | 13.1632 | 13.2692 | -1.9222k | -1.8603k |
| | 10 Hz | 16.4013M | 113.914k | 11.6560 | 11.7506 | -21.7155 | -21.4432 |
| | 100 Hz | 2.2351M | 11.3527k | 9.94505 | 9.9881 | -254.55m | -253.35m |
| | 1 M Hz | -48.0232k | -1.5888k | 17.9613 | 18.5779 | -1.4102m | -1.5387k |
| | | | | | | | |
| 4% H ₂ | 20 Hz | -- | 9.0168M | 19.0629 | 15.2773 | -- | -- |
| | 100 Hz | -- | 9.6642M | 19.1275 | 14.8492 | -- | -- |
| | 1 Hz | -- | 963.131k | 13.7144 | 13.8587 | -1.8560k | -1.8560k |
| | 10 Hz | 16.1389M | 102.446k | 12.1965 | 12.2678 | -20.8238 | -20.8238 |
| | 100 Hz | 2.1581M | 10.6423k | 10.4323 | 10.4891 | -243.06m | -243.06m |
| | 1 M Hz | -44.2995k | -1.4128k | 19.7767 | 20.4307 | -1.2808m | -1.2808m |
| | | | | | | | |
| 1% | 20 Hz | -- | 9.0168M | 19.0629 | 15.2773 | -- | -- |
| | 100 Hz | -- | 9.6642M | 19.1275 | 14.8492 | -- | -- |
| | 1 Hz | -- | 963.131k | 13.7144 | 13.8587 | -1.8560k | -1.8560k |
| | 10 Hz | 16.1389M | 102.446k | 12.1965 | 12.2678 | -20.8238 | -20.8238 |
| | 100 Hz | 2.1581M | 10.6423k | 10.4323 | 10.4891 | -243.06m | -243.06m |
| | 1 M Hz | -44.2995k | -1.4128k | 19.7767 | 20.4307 | -1.2808m | -1.2808m |

| Pd/g-C ₃ N ₄ (40% loading) | | | | | | | |
|--|-----------|--------------------|--------------------|---------------------|--------------------|--------------------|--------------------|
| Concentration | Frequency | R _p (Ω) | R _s (Ω) | C _p (pf) | C _s (F) | L _p (H) | L _s (H) |
| 0% H ₂ | 20 Hz | 22.1986M | 22.0956M | 19.8727 | 6.3964n | ---- | -10.249k |
| | 100 Hz | 21.8067M | 20.5503M | 19.9624 | 306.66p | ---- | -8.017k |
| | 1 kHz | 18.9500M | 4.0180M | 16.1506 | 20.832p | -1.573k | -1.236k |
| | 10 kHz | 8.2091M | 147.086k | 14.2623 | 14.5763p | -17.663 | -17.358 |
| | 100 kHz | 1.6406M | 10.5901k | 12.3183 | 12.3355p | -206.21m | -204.92m |
| | 1 M Hz | -74.0235 | -883.074 | 17.2827 | 20.9906p | -1.3443m | -1.2705m |
| | | | | | | | |
| 10% H ₂ | 20 Hz | 3.463M | 3.468M | 24.649p | 201.087n | --- | -277.525 |
| | 100 Hz | 3.449M | 3.419M | 16.745p | 12.8580n | --- | -213.218 |
| | 1 kHz | 3.3529M | 3.088M | 14.516p | 167.304p | -1.740k | -161.168 |
| | 10 Hz | 2.797M | 455.227k | 12.893p | 15.385P | 19.639 | -16.522 |
| | 100 Hz | 1.175M | 17.960k | 10.901p | 11.0530p | 232.316m | -229.13m |
| | 1 M Hz | -49.731k | -1.305k | 19.470p | 19.996p | -1.308m | -1.267m |
| | | | | | | | |
| 1% H ₂ | 20 Hz | 3.463M | 3.468M | 24.649p | 201.087n | --- | -277.525 |
| | 100 Hz | 3.449M | 3.419M | 16.745p | 12.8580n | --- | -213.218 |
| | 1 Hz | 3.3529M | 3.088M | 14.516p | 167.304p | -1.740k | -161.168 |
| | 10 Hz | 2.797M | 455.227k | 12.893p | 15.385P | 19.639 | -16.522 |
| | 100 Hz | 1.175M | 17.960k | 10.901p | 11.0530p | 232.316m | -229.13m |
| | 1 M Hz | -49.731k | -1.305k | 19.470p | 19.996p | -1.308m | -1.267m |
| | | | | | | | |
| 4% H ₂ | 20 Hz | -- | 9.0168M | 19.0629 | 15.2773 | -- | -- |
| | 100 Hz | -- | 9.6642M | 19.1275 | 14.8492 | -- | -- |
| | 1 Hz | -- | 963.131k | 13.7144 | 13.8587 | -1.8560k | -1.8560k |
| | 10 Hz | 16.1389M | 102.446k | 12.1965 | 12.2678 | -20.8238 | -20.8238 |
| | 100 Hz | 2.1581M | 10.6423k | 10.4323 | 10.4891 | -243.06m | -243.06m |
| | 1 M Hz | -44.2995k | -1.4128k | 19.7767 | 20.4307 | -1.2808m | -1.2808m |

Chapter 7

Conclusion and Future Work:

Summary of the work:

Pd/g-C₃N₄ nano-composite has been synthesized by chemical process. Uniform impregnation of Pd metal nanoparticles was confirmed by HRTEM analysis. The average particle size was found to be 4.22nm, which closely matches the particle size calculated using Scherrer's formula and the obtained XRD data. The thermal stability of g-C₃N₄ and Pd/g-C₃N₄ was confirmed. Pd metal nanoparticle loading was determined to be 19.3% (wt%). Cyclic voltammetry analysis revealed significant hydrogen evolution reaction and hydrogen oxidation reaction of Pd/g-C₃N₄ nanocomposite. I-V measurements conclude that Pd/g-C₃N₄ gives better response towards hydrogen gas. Sensor resistivity was recorded to be in the kΩ range, which is in improvement on the reported value in the literature. Resistance change from 14 kΩ to 11.3 kΩ was determined at room temperature. This sensitive response of the Pd/g-C₃N₄ motivates for future exploration of this material for efficient hydrogen gas sensing.

Nanocomposite films of Pd/g-C₃N₄, Pt/g-C₃N₄, ZnO/g-C₃N₄ were deposited on clean Astro-glass substrates at 350°C, by a newly developed, dual-beam-nebulized spray pyrolysis system. The g-C₃N₄ with the tri-s-triazinering and the tetragonal structure of oxidized was confirmed by X-ray diffraction studies. Scanning electron microscopy evinced the presence of the sheet-like structure of g-C₃N₄ as well as of Pd nanoparticles that are impregnated on the g-C₃N₄ matrix. The studies also revealed the porous morphology of the film, which is good for gas sensing applications. This is because a porous structure helps in the trapping of gas, which increases the sensitivity towards the analyte gas. A film with good uniformity was produced. Additionally, it was found that an increase in precursor yields a denser and more uniform film, albeit a thicker one. Transmission electron microscopy confirmed the size of the Pd nanoparticles to be 5-10nm. X-ray photoelectron spectroscopy revealed the presence of C1s, N1s, and Pd3d (3d 5/2 and 3d

3/2). Two oxidation states of Pd, Pd^0 and Pd^{+2} , were detected. It also showed a slight shift in the binding energy, which indicates the strong interaction between the Pd metal nanoparticle and the g- C_3N_4 matrix. In order to determine Pd metal nanoparticle loading on the Pd/g- C_3N_4 nanocomposite and the respective phase changes with changes in temperature, TG/DTA analysis was performed. The Pd metal loading was found to be approximately 19.4%, which had undergone a phase change. However, pure g- C_3N_4 yielded two-phase changes, which correspond to evaporation and thermal decomposition. Hydrogen gas sensing of the film was recorded at the concentrations of 4% and 10%, which showed faster response and recovery time of a few seconds as compared to the previously reported study. Also, the sensitivity of the film was observed to be better. The results bear good reproducibility.

Hydrogen sensing properties of the Pt and ZnO impregnated graphitic carbon nitride nanocomposite at room temperature were also studied. The sensing material was synthesized by a hydrothermal approach, where melamine and chloroplatinic acid hexahydrate were used as precursors. The sensor was fabricated by depositing sensing materials on a screen-printed carbon electrode by jet nebulizer spray pyrolysis setup. The crystallinity, nano morphology, elemental analysis, and chemical composition of the products were examined by XRD, SEM, HRTEM, EDS, and XPS. The Pt nanoparticle size in g- C_3N_4 composite was calculated on the basis of XRD data and validated by TEM data, which shows an average particle size of 3-5 nm. A dynamic response or change in electrical resistance was recorded during the presence and the absence of the analyte gas. The sensitivity obtained for the sensor at different concentrations of hydrogen gas was recorded. The sensing results depict that the Pt/g- C_3N_4 , ZnO/g- C_3N_4 shows a good response towards the hydrogen gas, and could be used for reliable hydrogen gas sensing.

Future work:

The performance of the sensor can be enhanced by some adaptations and modifications to the sensor fabrication.

1. Sensor performance can be improved further by making the film porous to increase the surface-to-volume ratio.
2. Higher conductive electrode, such as silver or gold, can improve the sensor response, although it will increase the sensor cost.
3. Stacking of sensing layers could also be fabricated for the sensing of hydrogen gas.
4. Other sophisticated techniques such as sputtering and lithography could be used for sensor fabrication. Which could result in thinner and precise film, and hence, improves the sensing, although again, it will increase the overall process cost.
5. Degradation of the sensor can be investigated to examine its life span.

References:

- [1] Luna-Moreno, Donato, et al. "Optical fiber hydrogen sensor based on core diameter mismatch and annealed Pd–Au thin films." *Sensors and Actuators B: Chemical* 125.1 (2007): 66-71. <http://dx.doi.org/10.1016/j.snb.2007.01.036>
- [2] Hoa, Nguyen Duc, et al. "Urea mediated synthesis of Ni (OH) 2 nanowires and their conversion into NiO nanostructure for hydrogen gas-sensing application." *International Journal of Hydrogen Energy* 43.19 (2018): 9446-9453. <http://dx.doi.org/10.1016/j.ijhydene.2018.03.166>
- [3] El-Emam, Rami S., and Ibrahim Dincer. "Nuclear-Assisted Hydrogen Production." *Fuel Cells and Hydrogen Production: A Volume in the Encyclopedia of Sustainability Science and Technology*, Second Edition (2019): 1151-1161. http://dx.doi.org/10.1007/978-1-4939-7789-5_961
- [4] Samantaray, Sai Smruti, et al. "Enhanced hydrogen storage performance in Pd₃Co decorated nitrogen/boron-doped graphene composites." *International Journal of Hydrogen Energy* 43.16 (2018): 8018-8025. <http://dx.doi.org/10.1016/j.ijhydene.2018.03.078>
- [5] Acar, Canan, and Ibrahim Dincer. "Review and Evaluation of Hydrogen Production Options for Better Environment." *Journal of Cleaner Production* (2019). <http://dx.doi.org/10.1016/j.jclepro.2019.02.046>
- [6] Van Duy, Nguyen, et al. "Effects of gamma irradiation on hydrogen gas-sensing characteristics of Pd–SnO₂ thin-film sensors." *International Journal of Hydrogen Energy* 40.36 (2015): 12572-12580. <http://dx.doi.org/10.1016/j.ijhydene.2015.07.070>

- [7] Hübner, Thomas, et al. "Hydrogen sensors—a review." *Sensors and Actuators B: Chemical* 157.2 (2011): 329-352. <http://dx.doi.org/10.1016/j.snb.2011.04.070>
- [8] D'Amico, A., et al. "A micromachined gold-palladium Kelvin probe for hydrogen sensing." *Sensors and Actuators B: Chemical* 142.2 (2009): 418-424. [10.1016/j.snb.2009.03.076](http://dx.doi.org/10.1016/j.snb.2009.03.076)
- [9] De Luca, L., et al. "Hydrogen sensing characteristics of Pt/TiO₂/MWCNTs composites." *international journal of hydrogen energy* 37.2 (2012): 1842-1851. <http://dx.doi.org/10.1016/j.ijhydene.2011.10.017>
- [10] De Luca, L., et al. "Hydrogen sensing characteristics of Pt/TiO₂/MWCNTs composites." *international journal of hydrogen energy* 37.2 (2012): 1842-1851. <http://dx.doi.org/10.1016/j.ijhydene.2011.10.017>
- [11] Palmisano, V., et al. "Evaluation of selectivity of commercial hydrogen sensors." *International Journal of Hydrogen Energy* 39.35 (2014): 20491-20496. <http://dx.doi.org/10.1016/j.ijhydene.2014.03.251>
- [12] Raghu, S., P. N. Santhosh, and S. Ramaprabhu. "Nanostructured palladium modified graphitic carbon nitride—high-performance room temperature hydrogen sensor." *International Journal of Hydrogen Energy* 41.45 (2016): 20779-20786. <http://dx.doi.org/10.1016/j.ijhydene.2016.09.002>
- [13] Lavanya, N., et al. "Development of a selective hydrogen leak sensor based on chemically doped SnO₂ for automotive applications." *International Journal of Hydrogen Energy* 42.15 (2017): 10645-10655. <http://dx.doi.org/10.1016/j.ijhydene.2017.03.027>

- [14] Luo, Yifan, et al. "Hydrogen sensors based on noble metal doped metal-oxide semiconductor: A review." *International Journal of Hydrogen Energy* 42.31 (2017): 20386-20397. <http://dx.doi.org/10.1016/j.ijhydene.2017.06.066>
- [15] Gu, Haoshuang, Zhao Wang, and Yongming Hu. "Hydrogen gas sensors based on semiconductor oxide nanostructures." *Sensors* 12.5 (2012): 5517-5550. <http://dx.doi.org/10.3390/s120505517>
- [16] Matsumiya, Masahiko, et al. "Nano-structured thin-film Pt catalyst for thermoelectric hydrogen gas sensor." *Sensors and Actuators B: Chemical* 93.1 (2003): 309-315. [http://dx.doi.org/10.1016/s0925-4005\(03\)00223-5](http://dx.doi.org/10.1016/s0925-4005(03)00223-5)
- [17] Sekimoto, S., et al. "A fiber-optic evanescent-wave hydrogen gas sensor using palladium-supported tungsten oxide." *Sensors and Actuators B: Chemical* 66.1 (2000): 142-145. [http://dx.doi.org/10.1016/s0925-4005\(00\)00330-0](http://dx.doi.org/10.1016/s0925-4005(00)00330-0)
- [18] Butler, Michael A. "Micromirror optical-fiber hydrogen sensor." *Sensors and actuators B: Chemical* 22.2 (1994): 155-163. [http://dx.doi.org/10.1016/0925-4005\(94\)87015-2](http://dx.doi.org/10.1016/0925-4005(94)87015-2)
- [19] Singh, Vinod, et al. "Room temperature response and enhanced hydrogen sensing in size selected Pd-C core-shell nanoparticles: Role of carbon shell and Pd-C interface." *International Journal of Hydrogen Energy* 43.2 (2018): 1025-1033. <http://dx.doi.org/10.1016/j.ijhydene.2017.11.143>
- [20] Walia, Sunil, et al. "Transparent Pd Wire Network-Based Areal Hydrogen Sensor with Inherent Joule Heater." *ACS applied materials & interfaces* 8.35 (2016): 23419-23424. <http://dx.doi.org/10.1021/acsami.6b08275>

- [21] Ollagnier, Antonin, et al. "Activation process of reversible Pd thin film hydrogen sensors." *Sensors and Actuators B: Chemical* 186 (2013): 258-262. <http://dx.doi.org/10.1016/j.snb.2013.05.041>
- [22] Sun, Ling, et al. "The effects of Ni contents on hydrogen sensing response of closely spaced Pd–Ni alloy nanoparticle films." *International Journal of Hydrogen Energy* 41.2 (2016): 1341-1347. <http://dx.doi.org/10.1016/j.ijhydene.2015.10.117>
- [23] Lueng, Chris, et al. "Adjustable sensitivity for hydrogen gas sensing using perpendicular-to-plane ferromagnetic resonance in Pd/Co Bi-layer films." *International Journal of Hydrogen Energy* 42.5 (2017): 3407-3414. <http://dx.doi.org/10.1016/j.ijhydene.2016.09.204>
- [24] Uddin, ASM Iftekhar, et al. "Effects of Pt shell thickness on self-assembly monolayer Pd@ Pt core-shell nanocrystals based hydrogen sensing." *international journal of hydrogen energy* 41.34 (2016): 15399-15410. <http://dx.doi.org/10.1016/j.ijhydene.2016.06.138>
- [25] Contescu, Cristian I., et al. "Detection of hydrogen spillover in palladium-modified activated carbon fibers during hydrogen adsorption." *The Journal of Physical Chemistry C* 113.14 (2009): 5886-5890. <http://dx.doi.org/10.1021/jp900121k>
- [26] Jiao, Mingzhi, et al. "On-chip growth of patterned ZnO nanorod sensors with PdO decoration for enhancement of hydrogen-sensing performance." *International journal of hydrogen energy* 42.25 (2017): 16294-16304. <http://dx.doi.org/10.1016/j.ijhydene.2017.05.135>
- [27] Zhang, Jun, et al. "Nanostructured Materials for Room-Temperature Gas Sensors." *Advanced Materials* 28.5 (2016): 795-831. <http://dx.doi.org/10.1002/adma.201503825>

- [28] Cansizoglu, Mehmet F., et al. "Enhanced hydrogen storage by a variable temperature process." *International Journal of Hydrogen Energy* 44.7 (2019): 3771-3778. <http://dx.doi.org/10.1016/j.ijhydene.2018.12.087>
- [29] Woo, Je-A., et al. "Fast response of hydrogen sensor using palladium nanocube-TiO₂ nanofiber composites." *International Journal of Hydrogen Energy* 42.29 (2017): 18754-18761. <http://dx.doi.org/10.1016/j.ijhydene.2017.04.189>
- [30] Chen, Wan Ping, et al. "Extraordinary room-temperature hydrogen sensing capabilities of porous bulk Pt-TiO₂ nanocomposite ceramics." *international journal of hydrogen energy* 41.4 (2016): 3307-3312. <http://dx.doi.org/10.1016/j.ijhydene.2015.12.151>
- [31] Dhall, Shivani, Kapil Sood, and Rashi Nathawat. "Room temperature hydrogen gas sensors of functionalized carbon nanotubes based hybrid nanostructure: Role of Pt sputtered nanoparticles." *International Journal of Hydrogen Energy* 42.12 (2017): 8392-8398. <http://dx.doi.org/10.1016/j.ijhydene.2017.02.005>
- [32] Adamyan, A. Z., et al. "Sol-gel derived thin-film semiconductor hydrogen gas sensor." *International Journal of Hydrogen Energy* 32.16 (2007): 4101-4108. <http://dx.doi.org/10.1016/j.ijhydene.2007.03.043>
- [33] Wongchoosuk, Chatchawal, et al. "Multi-walled carbon nanotube-doped tungsten oxide thin films for hydrogen gas sensing." *Sensors* 10.8 (2010): 7705-7715. <http://dx.doi.org/10.3390/s100807705>

- [34] Lim, Z. H., et al. "A facile approach towards ZnO nanorods conductive textile for room temperature multifunctional sensors." *Sensors and Actuators B: Chemical* 151.1 (2010): 121-126. <http://dx.doi.org/10.1016/j.snb.2010.09.037>
- [35] Cui, Lujun, et al. "Experimental research on a reflective optical fiber bundle hydrogen gas sensor." *Sensor Review* 37.2 (2017): 180-186. <http://dx.doi.org/10.1108/sr-09-2016-0193>
- [36] Kumar, Rakesh, et al. "Fast response and recovery of hydrogen sensing in Pd–Pt nanoparticle–graphene composite layers." *Nanotechnology* 22.27 (2011): 275719. <http://dx.doi.org/10.1088/0957-4484/22/27/275719>
- [37] Zhao, Z., et al. "All-optical hydrogen sensor based on a high alloy content palladium thin film." *Sensors and Actuators B: Chemical* 113.1 (2006): 532-538. <http://dx.doi.org/10.1016/j.snb.2005.03.070>
- [38] Cui, L. J., Zhang, G., Shang, H. C., and Chen, Y. P., "Composition Control of Palladium-Silver Alloy for Optical Fiber Hydrogen Sensor". *Advanced Materials Research*, Vol.317, (2011) pp.1045-1049. <http://dx.doi.org/10.4028/www.scientific.net/amr.317-319.1045>
- [39] Dai, J., Yang, M., Yu, X. and Lu, H., "Optical hydrogen sensor based on etched fiber Bragg grating sputtered with Pd/Ag composite film", *Optical Fiber Technology*, Vol.19No.1, (2013) pp.26-30. <http://dx.doi.org/10.1016/j.yofte.2012.09.006>
- [40] Slaman, M., et al. "Fiber optic hydrogen detectors containing Mg-based metal hydrides." *Sensors and Actuators B: Chemical* 123.1 (2007): 538-545. <http://dx.doi.org/10.1016/j.snb.2006.09.058>

- [41] Sekimoto, S., et al. "A fiber-optic evanescent-wave hydrogen gas sensor using palladium-supported tungsten oxide." *Sensors and Actuators B: Chemical* 66.1 (2000): 142-145. [http://dx.doi.org/10.1016/s0925-4005\(00\)00330-0](http://dx.doi.org/10.1016/s0925-4005(00)00330-0)
- [42] Luna-Moreno, Donato, et al. "Optical fiber hydrogen sensor based on core diameter mismatch and annealed Pd–Au thin films." *Sensors and Actuators B: Chemical* 125.1 (2007): 66-71. <http://dx.doi.org/10.1016/j.snb.2007.01.036>
- [43] Gautam, Yogendra K., et al. "A room temperature hydrogen sensor based on Pd–Mg alloy and multilayers prepared by magnetron sputtering." *international journal of hydrogen energy* 40.45 (2015): 15549-15555. <http://dx.doi.org/10.1016/j.ijhydene.2015.08.078>
- [44] Hayashi, Yumi, et al. "Investigation of PdCuSi metallic glass film for hysteresis-free and fast response capacitive MEMS hydrogen sensors." *International Journal of Hydrogen Energy* 43.19 (2018): 9438-9445. <http://dx.doi.org/10.1016/j.ijhydene.2018.03.149>
- [45] Sripada, Raghu, et al. "Platinum and platinumiron alloy nanoparticles dispersed nitrogen-doped graphene as high performance room temperature hydrogen sensor." *Int J HydrogenEnergy* 40 (2015): 1034. <http://dx.doi.org/10.1016/j.ijhydene.2015.06.018> Arya, Sunil K., et al. "Advances in materials for room temperature hydrogen sensors." *Analyst* 137.12 (2012): 2743-2756. <http://dx.doi.org/10.1039/c2an16029c>
- [46] Kim, Seil, et al. "Fabrication and characterization of thermochemical hydrogen sensor with laminated structure." *International Journal of Hydrogen Energy* 42.1 (2017): 749-756. <http://dx.doi.org/10.1016/j.ijhydene.2016.08.216>

- [47] Leonardi, Salvatore Gianluca, et al. "Development of a hydrogen dual sensor for fuel cell applications." *International Journal of Hydrogen Energy* (2018). <http://dx.doi.org/10.1016/j.ijhydene.2018.02.019>
- [48] Tonezzer, Matteo, et al. "Selective hydrogen sensor for liquefied petroleum gas steam reforming fuel cell systems." *International Journal of Hydrogen Energy* 42.1 (2017): 740-748. <http://dx.doi.org/10.1016/j.ijhydene.2016.11.102>
- [49] Wang, Xinchun, et al. "A metal-free polymeric photocatalyst for hydrogen production from water under visible light." *Nature materials* 8.1 (2009): 76.<http://dx.doi.org/10.1038/nmat2317>
- [50] Bressan, J. D., A. Tramontin, and C. Rosa. "Modeling of nanoindentation of bulk and thin film by finite element method." *Wear* 258.1-4 (2005): 115-122.
- [51] Pelletier, H. "Predictive model to estimate the stress–strain curves of bulk metals using nanoindentation." *Tribology International* 39.7 (2006): 593-606.
- [52] Bressan, J. D., A. Tramontin, and C. Rosa. "Modeling of nanoindentation of bulk and thin film by finite element method." *Wear* 258.1-4 (2005): 115-122
- [53] Pelletier, Hervé, Joël Krier, and Pierre Mille. "Characterization of mechanical properties of thin films using a nanoindentation test." *Mechanics of materials* 38.12 (2006): 1182-1198.
- [54] Alaboodi, Abdulaziz S., and Zahid Hussain. "Finite element modeling of nano-indentation technique to characterize thin film coatings." *Journal of King Saud University-Engineering Sciences* (2017).

- [55] Tsui, T. Y., W. C. Oliver, and G. M. Pharr. "Indenter geometry effects on the measurement of mechanical properties by nanoindentation with sharp indenters." *MRS Online Proceedings Library Archive* 436 (1996).
- [56] Burnett, Philip J., and D. S. Rickerby. "The mechanical properties of wear-resistant coatings: II: Experimental studies and interpretation of hardness." *Thin solid films* 148.1 (1987): 51-65.
- [57] Hay, J. L., M. E. O'Hern, and W. C. Oliver. "The Importance of Contact Radius for Substrate-Independent Property Measurement of Thin Films." *MRS Online Proceedings Library Archive* 522 (1998).
- [58] Hay, Jack C., and G. M. Pharr. "Critical issues in measuring the mechanical properties of hard films on soft substrates by nanoindentation techniques." *MRS Online Proceedings Library Archive* 505 (1997).
- [59] Joslin, D. L., and W. C. Oliver. "A new method for analyzing data from continuous depth-sensing microindentation tests." *Journal of Materials Research* 5.1 (1990): 123-126.
- [60] Korsunsky, A. M., et al. "On the hardness of coated systems." *Surface and Coatings Technology* 99.1-2 (1998): 171-183.
- [61] Saha, Ranjana, et al. "Indentation of a soft metal film on a hard substrate: strain gradient hardening effects." *Journal of the Mechanics and Physics of Solids* 49.9 (2001): 1997-2014.
- [62] Mortazavi, Bohayra, Gianaurelio Cuniberti, and Timon Rabczuk. "Mechanical properties and thermal conductivity of graphitic carbon nitride: A molecular dynamics study." *Computational Materials Science* 99 (2015): 285-289.

- [63] Abdullahi, Yusuf Zuntu, et al. "Mechanical and electronic properties of graphitic carbon nitride sheet: First-principles calculations." *Solid State Communications* 248 (2016): 144-150.
- [64] Ajori, Shahram, Reza Ansari, and Sina Malakpour. "A density functional study on the mechanical properties of metal-free two-dimensional polymer graphitic Carbon-Nitride." *International Journal of Nano Dimension* 8.3 (2017): 234-240.
- [65] Bian, Juncao, et al. "Thermal vapor condensation of uniform graphitic carbon nitride films with remarkable photocurrent density for photoelectrochemical applications." *Nano Energy* 15 (2015): 353-361.
- [66] Tiwari, Atul. "Nanomechanical analysis of hybrid silicones and hybrid epoxy coatings—A brief review." *Advances in Chemical Engineering and Science* 2.1 (2012): 34-44.
- [67] Nassar, Joanna M., et al. "From stretchable to reconfigurable inorganic electronics." *Extreme Mechanics Letters* 9 (2016): 245-268.
- [68] Wang, Yong, Xinchun Wang, and Markus Antonietti. "Polymeric graphitic carbon nitride as a heterogeneous organocatalyst: from photochemistry to multipurpose catalysis to sustainable chemistry." *Angewandte Chemie International Edition* 51.1 (2012): 68-89.
- [69] Girish, M., et al. "A facile approach called nebulized spray pyrolysis to deposit MnS thin films: Effect of solution concentration with EDTA on the physical properties." *Optik-International Journal for Light and Electron Optics* 126.19 (2015): 2074-2079.
<http://dx.doi.org/10.1016/j.ijleo.2015.05.072>
- [70] Mohamed, J. Raj, C. Sanjeeviraja, and L. Amalraj. "Influence of substrate temperature on physical properties of (111) oriented CdIn₂S₄ thin films by nebulized

spray pyrolysis technique." Journal of Asian Ceramic Societies 4.2 (2016): 191-200.<http://dx.doi.org/10.1016/j.jascer.2016.03.002>

- [71] Mariappan, R., et al. "Structural, Optical and Electrical Properties of Thin Films Using Nebulizer Spray Pyrolysis Technique." Indian Journal of Materials Science 2013 (2013).<http://dx.doi.org/10.1155/2013/516812>
- [72] Illakkiya, J. Tamil, P. UshaRajalakshmi, and Rachel Oommen. "Nebulized spray pyrolysis: a new method for synthesis of graphene film and their characteristics." Surface and Coatings Technology 307 (2016): 65-72.<http://dx.doi.org/10.1016/j.surfcoat.2016.08.051>
- [73] Mohamed, J. Raj, C. Sanjeeviraja, and L. Amalraj. "Effect of substrate temperature on nebulized spray pyrolysed In 2 S 3 thin films." Journal of Materials Science: Materials in Electronics 27.5 (2016): 4437-4446.<http://dx.doi.org/10.1007/s10854-016-4315-x>
- [74] Huang, Sheng, Wenjun Luo, and Zhigang Zou. "Band positions and photoelectrochemical properties of Cu₂ZnSnS₄ thin films by the ultrasonic spray pyrolysis method." Journal of Physics D: Applied Physics 46.23 (2013): 235108.<http://dx.doi.org/10.1088/0022-3727/46/23/235108>
- [75] Fu, Xiaorong, et al. "Preparation and characterization of MgO thin films by a simple nebulized spray pyrolysis technique." Applied surface science 148.3-4 (1999): 223-228.[http://dx.doi.org/10.1016/s0169-4332\(99\)00126-9](http://dx.doi.org/10.1016/s0169-4332(99)00126-9)
- [76] Wang, Sheng-Yue, and You-Wei Du. "Preparation of nanocrystalline bismuth sulfide thin films by asynchronous-pulse ultrasonic spray pyrolysis technique." Journal of crystal growth 236.4 (2002): 627-634.[http://dx.doi.org/10.1016/s0022-0248\(02\)00846-1](http://dx.doi.org/10.1016/s0022-0248(02)00846-1)
- [77] Ortiz, A., et al. "Structural and optical characteristics of gallium oxide thin films deposited by ultrasonic spray pyrolysis." Journal of The Electrochemical Society 148.2 (2001): F26-F29. <http://dx.doi.org/10.1149/1.1342183>

- [78] Wang, Sheng-Yue, and Zu-Hong Lu. "Preparation of Y₂O₃ thin films deposited by pulse ultrasonic spray pyrolysis." *Materials chemistry and physics* 78.2 (2003): 542-545. [http://dx.doi.org/10.1016/s0254-0584\(02\)00350-4](http://dx.doi.org/10.1016/s0254-0584(02)00350-4)
- [79] Liu, Lin, Gap-Yong Kim, and Abhijit Chandra. "Fabrication of solid oxide fuel cell anode electrode by spray pyrolysis." *Journal of Power Sources* 195.20 (2010): 7046-7053. <http://dx.doi.org/10.1016/j.jpowsour.2010.04.083>
- [80] Zhang, Xia, et al. "Structural and optical properties of Zn_{1-x}Mg_xO thin films deposited by ultrasonic spray pyrolysis." *Thin Solid Films* 492.1-2 (2005): 248-252. <http://dx.doi.org/10.1016/j.tsf.2005.06.088>
- [81] Singh, Preetam, Ajay Kaushal, and Davinder Kaur. "Mn-doped ZnO nanocrystalline thin films prepared by ultrasonic spray pyrolysis." *Journal of Alloys and Compounds* 471.1-2 (2009): 11-15. <http://dx.doi.org/10.1016/j.jallcom.2008.03.123>
- [82] Walsh, Dominic, et al. "Aerosol-mediated fabrication of porous thin films using ultrasonic nebulization." *Chemistry of materials* 19.3 (2007): 503-508. <http://dx.doi.org/10.1021/cm0621951>
- [83] Wang, Shengyue, et al. "Characterization and gas-sensing properties of nanocrystalline iron (III) oxide films prepared by ultrasonic spray pyrolysis on silicon." *Sensors and Actuators B: Chemical* 69.1-2 (2000): 22-27. [http://dx.doi.org/10.1016/s0925-4005\(00\)00304-x](http://dx.doi.org/10.1016/s0925-4005(00)00304-x)
- [84] Bian, Jiming, et al. "Properties of undoped n-type ZnO film and N-In codoped p-type ZnO film deposited by ultrasonic spray pyrolysis." *Chemical Physics Letters* 393.1-3 (2004): 256-259. <http://dx.doi.org/10.1016/j.cplett.2004.06.044>
- [85] Kamble, Vinayak B., and Arun M. Umarji. "Chromium oxide thin films by Ultrasonic Nebulized Spray Pyrolysis of Aqueous Combustion Mixture for gas sensing

application." Physics and Technology of Sensors (ISPTS), 2012 1st International Symposium on. IEEE, 2012.<http://dx.doi.org/10.1109/ispts.2012.6260915>

- [86] Ebenso, E. E., et al. "Thin films of $\text{Ln}_{1-x}\text{Sr}_x\text{CoO}_3$ (Ln= La, Nd and Gd) and SrRuO_3 by nebulized spray pyrolysis." *Solid state sciences* 2.8 (2000): 833-839.[http://dx.doi.org/10.1016/s1293-2558\(00\)01098-0](http://dx.doi.org/10.1016/s1293-2558(00)01098-0)
- [87] Zhou, Lingyu, et al. "Ultrathin two-dimensional graphitic carbon nitride as a solution-processed cathode interfacial layer for inverted polymer solar cells." *Journal of Materials Chemistry A* 4.21 (2016): 8000-8004.<http://dx.doi.org/10.1039/c6ta01894g>
- [88] Bian, Juncao, et al. "Thermal vapor condensation of uniform graphitic carbon nitride films with remarkable photocurrent density for photoelectrochemical applications." *Nano Energy* 15 (2015): 353-361.<http://dx.doi.org/10.1016/j.nanoen.2015.04.012>
- [89] Ghosh, Arpita, PrijiChandran, and S. Ramaprabhu. "Palladium-nitrogen coordinated cobalt alloy towards hydrogen oxidation and oxygen reduction reactions with high catalytic activity in renewable energy generations of proton exchange membrane fuel cell." *Applied Energy* 208 (2017): 37-48.<http://dx.doi.org/10.1016/j.apenergy.2017.10.022>
- [90] Zhu, Junjiang, et al. "Graphitic carbon nitride: synthesis, properties, and applications in catalysis." *ACS applied materials & interfaces* 6.19 (2014): 16449-16465.<http://dx.doi.org/10.1021/am502925j>
- [91] Yan SC, Li ZS, Zou ZG. Photodegradation performance of gC_3N_4 fabricated by directly heating melamine. *Langmuir* 2009;25:10397e401.
<http://dx.doi.org/10.1021/la900923z>.

- [92] Zhao Y, Liu Z, Chu W, Song L, Zhang Z, Yu D, et al. "Largescale synthesis of nitrogen-rich carbon nitride microfibers by using graphitic carbon nitride as precursor". *Adv Mater* 2008;20:1777e81. <http://dx.doi.org/10.1002/adma.200702230>.
- [93] Mircescu NE, Oltean M, Chis V, Leopold N. "FTIR, FT-Raman, SERS and DFT study on melamine". *Vib Spectrosc* 2012;62:165e71. <http://dx.doi.org/10.1016/j.vibspec.2012.04.008>
- [94] Yang, Shubin, et al. "Exfoliated graphitic carbon nitride nanosheets as efficient catalysts for hydrogen evolution under visible light." *Advanced materials* 25.17 (2013): 2452- 2456. <http://dx.doi.org/10.1002/chin.201331210>
- [95] Wang Z, Lv P, Hu Y, Hu K. "Thermal degradation study of intumescent flame retardants by TG and FTIR: melamine phosphate and its mixture with pentaerythritol". *J Anal Appl Pyrol* 2009;86:207–14. <http://dx.doi.org/10.1016/j.jaap.2009.06.007>.
- [96] Zhao X, Yan N. "One-pot synthesis and assembly of melamine-based nanoparticles for microporous polymer organic frameworks and their application as a support for a silver nanoparticle catalyst". *RSC Adv* 2015;5:69955–61. <http://dx.doi.org/10.1039/c5ra10602h>
- [97] Zinin PV, Ming LC, Sharma SK, Khabashesku VN, Liu X, Hong S, et al. "Ultraviolet and near-infrared Raman spectroscopy of graphitic C₃N₄ phase". *Chem Phys Lett* 2009;472:69–73. <http://dx.doi.org/10.1016/j.cplett.2009.02.068>.
- [98] Ferrari A, Robertson J. "Interpretation of Raman spectra of disordered and amorphous carbon". *Phys Rev B* 2000;61:14095–107. <http://dx.doi.org/10.1103/PhysRevB.61.14095>.
- [99] McMillan PF, Lees V, Quirico E, Montagnac G, Sella A, Reynard B, et al. "Graphitic carbon nitride C₆N₉H₃·HCl: characterisation by UV and near-IR FT Raman

spectroscopy". J Solid State Chem 2009;182:2670–7.
<http://dx.doi.org/10.1016/j.jssc.2009.07.030>.

- [100] Bhowmik, Tanmay, Manas Kumar Kundu, and Sudip Barman. "Palladium nanoparticle–graphitic carbon nitride porous synergistic catalyst for hydrogen evolution/oxidation reactions over a broad range of pH and correlation of its catalytic activity with measured hydrogen binding energy." *Acs Catalysis* 6.3 (2016): 1929–1941.<http://dx.doi.org/10.1021/acscatal.5b02485>
- [101] Srinivasu, Kancharlapalli, BrindabanModak, and Swapan K. Ghosh. "Porous graphitic carbon nitride: a possible metal-free photocatalyst for water splitting." *The Journal of Physical Chemistry C* 118.46 (2014): 26479–26484.<http://dx.doi.org/10.1021/jp506538d>
- [102] S. Dhall, N. Jaggi, "Room temperature hydrogen gas sensing properties of Pt sputtered F-MWCNTs/SnO₂ network", *Sens. Actuators B* 210 (2015) 742–747.<http://dx.doi.org/10.1016/j.snb.2015.01.031>
- [103] D.T. Phan, G.S. Chung, "Reliability of hydrogen sensing based on bimetallic Ni-Pd/graphene composites", *Int. J. Hydrogen Energy* 39 (2014) 20294–20304.<http://dx.doi.org/10.1016/j.ijhydene.2014.10.006>
- [104] Zhang, Dongzhi, Chuanxing Jiang, and Yong Zhang. "Room temperature hydrogen gas sensor based on palladium decorated tin oxide/molybdenum disulfide ternary hybrid via hydrothermal route." *Sensors and Actuators B: Chemical* 242 (2017): 15–24.<http://dx.doi.org/10.1016/j.snb.2016.11.005>

- [105] Tian, H., Fan, H., Ma, J., Ma, L., & Dong, G. (2017). Noble metal-free modified electrode of exfoliated graphitic carbon nitride/ZnO nanosheets for highly efficient hydrogen peroxide sensing. *Electrochimica Acta*, 247, 787-794.
- [106] Chidambaram, N., and K. Ravichandran. "Fabrication of ZnO/g-C₃N₄ nanocomposites for enhanced visible light driven photocatalytic activity." *Materials Research Express* 4.7 (2017): 075037.
- [107] Tian, H., Fan, H., Ma, J., Liu, Z., Ma, L., Lei, S., ... & Long, C. (2018). Pt-decorated zinc oxide nanorod arrays with graphitic carbon nitride nanosheets for highly efficient dual-functional gas sensing. *Journal of hazardous materials*, 341, 102-111.
- [108] Cao, J., Gong, Y., Wang, Y., Zhang, B., Zhang, H., Sun, G., ... & Zhang, Z. (2017). Cocoon-like ZnO decorated graphitic carbon nitride nanocomposite: Hydrothermal synthesis and ethanol gas sensing application. *Materials Letters*, 198, 76-80.
- [109] Moussa, H., Chouchene, B., Gries, T., Balan, L., Mozet, K., Medjahdi, G., & Schneider, R. (2018). Growth of ZnO Nanorods on Graphitic Carbon Nitride gCN Sheets for the Preparation of Photocatalysts with High Visible-Light Activity. *ChemCatChem*, 10(21), 4973-4983.
- [110] Raghu, S., P. N. Santhosh, and S. Ramaprabhu. "Nanostructured palladium modified graphitic carbon nitride-high performance room temperature hydrogen sensor." *International Journal of Hydrogen Energy* 41.45 (2016): 20779-20786. <http://dx.doi.org/10.1016/j.ijhydene.2016.09.002>
- [111] Zhao Y, Liu Z, Chu W, Song L, Zhang Z, Yu D, et al. "Large scale synthesis of nitrogen-rich carbon nitride microfibers by using graphitic carbon nitride as precursor". *Adv Mater* 2008;20:1777e81. <http://dx.doi.org/10.1002/adma.200702230>.

- [112] Mircescu NE, Oltean M, Chis V, Leopold N. "FTIR, FT-Raman, SERS and DFT study on melamine". *Vib Spectrosc* 2012;62:165-71. <http://dx.doi.org/10.1016/j.vibspec.2012.04.008>
- [113] Yang, Shubin, et al. "Exfoliated graphitic carbon nitride nanosheets as efficient catalysts for hydrogen evolution under visible light." *Advanced materials* 25.17 (2013): 2452- 2456. <http://dx.doi.org/10.1002/chin.201331210>
- [114] Zinin PV, Ming LC, Sharma SK, Khabashesku VN, Liu X, Hong S, et al. "Ultraviolet and near-infrared Raman spectroscopy of graphitic C₃N₄ phase". *Chem Phys Lett* 2009;472:69–73. <http://dx.doi.org/10.1016/j.cplett.2009.02.068>.
- [115] X.C. Wang, K. Maeda, A. Thomas, K. Takanabe, G. Xin, J.M. Carlsson, K. Domen, M. Antonietti, A metal-free polymeric photocatalyst for hydrogen production from water under visible light, *Nat. Mater.* 8 (2009) 76–80.
- [116] F. Goettmann, A. Fischer, M. Antonietti, A. Thomas, Chemical synthesis of mesoporous carbon nitrides using hard templates and their use as a metal-free catalyst for Friedel-Crafts reaction of benzene, *Angew. Chem. Int. Ed.* 45 (2006) 4467–4471
- [117] S.B. Yang, Y.J. Gong, J.S. Zhang, L. Zhan, L.L. Ma, Z.Y. Fang, R. Vajtai, X.C. Wang, P.M. Ajayan, Exfoliated graphitic carbon nitride nanosheets as efficient catalysts for hydrogen evolution under visible light, *Adv. Mater.* 25 (2013) 2452–2456
- [118] X.C. Wang, K. Maeda, A. Thomas, K. Takanabe, G. Xin, J.M. Carlsson, K. Domen, M. Antonietti, A metal-free polymeric photocatalyst for hydrogen production from water under visible light, *Nat. Mater.* 8 (2009) 76–80

- [119] Liu, Wei, et al. "Facile synthesis of g-C₃N₄/ZnO composite with enhanced visible light photooxidation and photoreduction properties." *Chemical Engineering Journal* 209 (2012): 386-393.
- [120] Anand, Kanika, et al. "Hydrogen sensor based on graphene/ZnO nanocomposite." *Sensors and Actuators B: Chemical* 195 (2014): 409-415.
- [121] L. Xu, R.F. Zheng, S.H. Liu, J. Song, J.S. Chen, B. Dong, H.W. Song, NiO@ZnO heterostructured nanotubes: electrospinning fabrication, characterization, and highly enhanced gas sensing properties, *Inorg. Chem.* 51 (2012) 7733–7740.
- [122] Cao, Jianliang, et al. "Cocoon-like ZnO decorated graphitic carbon nitride nanocomposite: Hydrothermal synthesis and ethanol gas sensing application." *Materials Letters* 198 (2017): 76-80.
- [123] Wu, Gang, et al. "Effect of preparation method on the physical and catalytic property of nanocrystalline Fe₂O₃." *Journal of alloys and compounds* 504.2 (2010): 371-376.
- [124] Moussa, Hatem, et al. "Growth of ZnO nanorods on graphitic carbon nitride gCN sheets for the preparation of photocatalysts with high visible-light activity." *ChemCatChem* 10.21 (2018): 4973-4983.
- [125] Tian, Hailin, et al. "Pt-decorated zinc oxide nanorod arrays with graphitic carbon nitride nanosheets for highly efficient dual-functional gas sensing." *Journal of hazardous materials* 341 (2018): 102-111.
- [126] Thomas, Arne, et al. "Graphitic carbon nitride materials: variation of structure and morphology and their use as metal-free catalysts." *Journal of Materials Chemistry* 18.41 (2008): 4893-4908.

- [127] S.B. Yang, Y.J. Gong, J.S. Zhang, L. Zhan, L.L. Ma, Z.Y. Fang, R. Vajtai, X.C. Wang, P.M. Ajayan, Exfoliated graphitic carbon nitride nanosheets as efficient catalysts for hydrogen evolution under visible light, *Adv. Mater.* 25 (2013) 2452–2456.
- [128] F. Dong, L. Wu, Y. Sun, M. Fu, Z. Wu, S.C. Lee, Efficient synthesis of polymeric gC₃N₄ layered materials as novel efficient visible light driven photocatalysts, *J. Mater. Chem.*, 21 (2011), 15171–15174.
- [129] J. Xu, Y. Li, S. Peng, G. Lu, S. Li, Eosin Y-sensitized graphitic carbon nitride fabricated by heating urea for visible light photocatalytic hydrogen evolution: the effect of the pyrolysis temperature of urea, *Phys. Chem. Chem. Phys.* 15 (2013), 7657–7565.
- [130] Sett, A., et al. "1D–2D hybrids as efficient optoelectronic materials: a study on graphitic carbon nitride nanosheets wrapped with zinc oxide rods." *Dalton Transactions* 47.13 (2018): 4501–4507.
- [131] J. Xu, Y. Li, S. Peng, G. Lu, S. Li, Eosin Y-sensitized graphitic carbon nitride fabricated by heating urea for visible light photocatalytic hydrogen evolution: the effect of the pyrolysis temperature of urea, *Phys. Chem. Chem. Phys.* 15 (2013), 7657–7565.
- [132] J.W. Fang, H.Q. Fan, M.M. Li, C.B. Long, Nitrogen self-doped graphitic carbon nitride as efficient visible light photocatalyst for hydrogen evolution, *J. Mater. Chem. A* 3 (2015) 13819–13826.
- [133] Y. Gao, X. Cao, X. Lan, C. Zhao, X. Xue, Y. Song, Solution-based doping of manganese into colloidal ZnO nanorods, *J. Phys. Chem. C* 112 (2008) 8832–8838.

List of publications:

Journal:

1. Ibrahim, A., U. B. Memon, S. P. Duttagupta, Ijjada Mahesh, RK Singh Raman, A. Sarkar, G. Pendharkar, and S. S. V. Tatiparti. "Nano-structured palladium impregnate graphitic carbon nitride composite for efficient hydrogen gas sensing." *International Journal of Hydrogen Energy* 45, no. 17 (2020): 10623-10636.[**Impact Factor: 4.084**]
2. "Hydrogen sensing properties of nano-confined Pt/g-C₃N₄ composite at room temperature: role of film thickness towards hydrogen sensing," *Materials Today Communications*– Under Review.
3. "Enhancement of response and recovery time of Palladium doped graphitic carbon nitride film for hydrogen gas sensing at room temperature deposited by nebulized spray pyrolysis," – *Advanced Engineering Material*– Under Review.

Conference:

1. Ibrahim, A., U. B. Memon, J. Praveen Kumar, S. P. Duttagupta, RK Singh Raman, A. Sarkar, G. Pendharkar, and S. S. V. Tatiparti. "Synthesis, structural and morphological property of a novel Pd/g-CN nanocomposite for gas sensing application." In *IOP Conference Series: Materials Science and Engineering*, vol. 499, no. 1, p. 012003. IOP Publishing, 2019.
4th International Conference on structural nanocomposites (NANOSTRUC 2018), Berlin, Germany, 23-24 May 2018
2. Ibrahim, A., U. B. Memon, Ijjada Mahesh, S. P. Duttagupta, RK Singh Raman, A. Sarkar, G. Pendharkar, and S. S. V. Tatiparti. "Nano-structured palladium impregnated graphitic carbon nitride composite for an efficient hydrogen gas sensing," in 11th International Conference on Advanced Nano Materials (ANM 2018), Aveiro, Portugal, 18-20 July 2018

Other Conference:

1. Memon, U. B., Ibrahim, A., Pattanayak, A., Duttagupta, S. P., Sarkar, A., & Raman, R. S. (2018, May). A simulation study of terahertz dielectric resonator using graphitic carbon nitride. In *2018 22nd International Microwave and Radar Conference (MIKON)* (pp. 722-725). IEEE. (Poznan, Poland)

Acknowledgment

I would like to thank my supervisors' prof. S P Duttaguta (Department of Electrical Engineering), Prof. A sarkar (Department of Chemical Engineering), Prof. Sankara Sarma V Tatiparti (Department of Energy science and engineering), Prof. Raman Singh (Department of Chemical Engineering and Aerospace Engineering) for their guidance and support towards my PhD research work.

I would like to thank Prof A Sarkar for being very resourceful and letting me use their lab for my entire Ph.D. duration and supporting me for my every necessity towards my work. I would like to thanks Prof. Raman Singh for being such a great help in my writing work, manuscript correction, to give importance to have strong writing skills for better communication.

I would like to thank the IITB-Monash research academy for supporting my work financially. Also, for providing funds during my work-related travel. I am very thankful to academy persons Murali Sastry, Kyatanahalli Nagabhushana Nancy Sowho, Jayasree T S, Kiran More, Krishna Warriar, Laya Vijaya. I would like to thanks Sheba Sanjay ma'am for her such a great help in my manuscript's language correction and piece of advice for better and improved writing skills.

I would like to thank the staff of Central facility IITB, SAIF IITB, for their help in material characterization. I also like to thank Prof. Sudarshan Kumar (Department of Aerospace Engineering) for letting me use their facility during gas sensing. I would like to thank Prof. Vijay A Juvekar (Department of Chemical Engineering) for the optical study of some of my samples.

I would like to thank my seniors from the Department of Electrical Engineering (IITB) Surya Prakash, Saumitra Singh, Soumya Gupta, Sirsendu Arose, Kuntal Ghosh, Subhash Yadav Also from Chemical Engineering (IITB) Ravi Kumar, Sachin Giri, Praveen Kumar Jella.

I also thank Saad-Al-Saadi (Department of Chemical Engineering, Monash University) for helping me during my stay at Monash University; I Sincerely thank him to got me familiar with their lab to antique, access to the facilities and many more.

I would also like to thank Monash University Chemical Engineering staff for helping me during my stay period. Special thanks to Kim Phu for giving me several important lab-based safety training, which would be helpful for my future perspective.

I would like to thank the IITB staff for their help and support. I would like to thank Dr. Mahesh Ijjada (Department of Chemical Engineering) for giving me a start at my Ph.D. work; he also taught me fundamental electrochemistry and many more.

Last but not least, I would like to thank my lab mate cum my batch mate cum my wife Uzma Bano Memon (Department of Electrical Engineering IITB and Department of Chemical Engineering Monash University) for being with me in every up and down during my Ph.D. period. She was a great help in my Ph.D. work. Her support is very significant, especially during the sensing aspect of my work.

Date: 30/10/20

Arif Ibrahim

